Large Strain Deformation of PETG at Processing Temperatures

by

Rebecca A. Brown

B.S. Mechanical Engineering, Utah State University, 1998

Submitted to the Department of Mechanical Engineering
in partial fulfillment of the requirements for the degree of

Master of Science in Mechanical Engineering
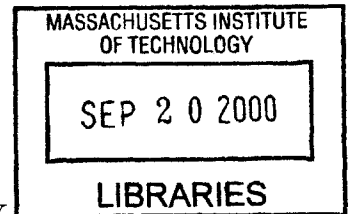
at the

MASSACHUSETTS INSTITUTE OF TECHNOLOGY

June 2000

Author . . . .
/ . . . .
Mechanical Engineering
May 5, 2000

Certified by . . . .
/ Mary C. Boyce
Professor of Mechanical Engineering
Thesis Supervisor

Accepted by . . . .
Ain A. Sonin
Chairman, Department Committee on Graduate Students

Large Strain Deformation of PETG at Processing Temperatures

by

Rebecca A. Brown

Abstract

Glycol modified Poly(ethylene terephthalate), PETG, a non-crystallizing form of PET, is tested in uniaxial compression and plane strain compression. In addition to deformation mode, the temperature and strain rate are varied in order to fully capture the strain rate, strain state, and temperature dependence of the material response.

A three-dimensional constitutive model is developed using the experimental results. The model uses two networks to represent the resistance of the material to deformation, one is an intermolecular resistance to flow and the other is a resistance due to molecular orientation. This model is used to produce computer simulations of uniaxial and plane strain compression experiments. The results indicate that the large strain hardening behavior of PETG can only be captured if the model includes a critical orientation parameter to halt the molecular relaxation process once the network achieves a specific level of molecular orientation.

The model predicts many of the features of the material behavior very well, including the initial modulus, roll over to flow stress, initial hardening modulus, cessation of molecular relaxation, and dramatic strain hardening. In plane strain compression the initial modulus, flow stress, and initial hardening modulus are also captured well. The model only falls short in capturing the large strain hardening behavior in plane strain compression. This can be improved with further work to better fit the strain hardening portion of the constitutive model.

Thesis Supervisor: Mary C. Boyce
Title: Professor of Mechanical Engineering

Acknowledgments

Thanks also to all of the members of my unofficial external support group. First and foremost are my parents. Thank you for your unfailing support, for those lengthy Sunday evening phone calls, and especially for your love and prayers. I have to thank Colin next, who will probably never know how much his friendship through our correspondence means to me. Thanks for the delightful e-mails which brightened my spirits, warmed my heart, and got me to thinking about the deeper things in life. Lisa, I could not have endured this year alone. You saved me in so many ways. Thanks for helping me work through so many issues and for reminding me that I really am a girl and that it's okay to be an emotional wreck occasionally. To the MIT FHE group who can never be thanked enough for the family away from home they are to me-I never would have thought I could learn so much from a bunch of undergrads; ldssa-request for the post-FHE huddles; the guys in the lab-Mats, Franco, Rami, and Mike-who teased me just enough to keep me smiling; my brother Ethan who let me tell him all of my boy problems plus some; the Allens who think I'm more amazing than I really am; my quartet-Brian, Stan, and Ivan-who put up with my half-hearted chamber music attempts while I put this together those last couple of weeks; my friends in the Relief Society Presidency-Jillaire, Lisa (again), and Megan-for the "efficient" meetings and girl talk; the institute council members-especially Robert, Dave, and Lisa (again)-for fun Sunday dinners and insane council meetings; and Bishop Davis whose wise counsel helped me sort through some tough decisions.

Above all, I especially feel grateful to my Heavenly Father. He is my light and my life, He comforts me in times of trial, strengthens me to bear my burdens, and provides peace and comfort in a tumultuous world.

Contents

List of Figures

9

Chapter 1

Introduction

In recent years there has been an increasing amount of interest in studying the large-strain mechanical behavior of poly(ethylene terephthalate), PET, above the glass transition temperature. PET is a widely used polymer for consumer products because it can be easily and inexpensively formed into lightweight but highly durable plastic bottles, ideal for bottled water and soda. PET is also used in many applications as a drawn fiber or stretched film. Much of the commercial success of PET lies in the fact that it crystallizes at large strains, thereby locking in the final shape after forming and creating a finished part with enhanced mechanical properties (higher stiffness, higher strength, etc.). Because of its wide use and complicated stress-strain behavior under large deformation, a robust constitutive model to accurately account for its stress-strain behavior is highly desirable.

The purpose of this research is to better understand the material behavior above the glass transition temperature in the processing regime. Specifically, the strain-rate, strain-state, and temperature dependence of the mechanical behavior is examined without the complication of strain-induced crystallization by studying a non-crystallizing form of PET, namely PETG. The stress-strain behavior of PETG is compared with results from previous work on PET to better isolate the contribution of strain-induced crystallization to strain hardening in PET. A constitutive model from previous work of Boyce, Socrate, and Llana[12] is modified to remove crystallization effects and is fit to the PETG experimental data. The revised model is

compared with the experimental data for PETG.

1.1 Experimental Background

Over the past half century, a substantial amount of experimental research has been conducted on PET, but relatively little has been published on PETG. As early as 1954, Marshall and Thompson[28] examined the load-extension-temperature properties of PET in an effort to better understand continuous drawing processes in the production of polyester yarn. A few years later, Thompson revisited the subject[34], looking specifically at the role of strain-induced crystallization in the hot drawing of PET fibers. His model captured the physics at critical points but did not represent the overall trend well. One weakness was the assumption that crystallization could be equated with a strain hardening process independent of time and temperature.

Several researchers have looked at the morphology and the development of crystalline order in PET. Misra and Stein[30] were some of the first to investigate the microstructure of PET as a function of deformation temperature and annealing time. They examined changes in crystallinity through density, wide angle X-ray diffraction, and small angle light scattering methods and noted an increase in crystallinity upon further annealing of the deformed material. They observed an initially rodlike morphology which evolves into ellipsoidal spherulites upon further annealing. In their experiments, strain rate was not varied and most of the PET structural information was obtained from experiments performed at 80 ° C.

Work by Bellare, Cohen, and Argon[8] at high temperatures (190 ° C) looked at the morphological evolution of initially semicrystalline PET during plane strain compression. They observed an initially spherulitic morphology which transforms into a lamellar microstructure, oriented toward the flow direction. This orientation causes the crystalline PET to develop an orthotropic symmetry.

Salem[32, 33] investigated the onset of crystallinity for initially amorphous PET in the temperature range near the glass transition (83 ° C to 96 ° C) and at moderately high uniaxial extension rates (nominal strain rates between .01 sec^{-1} and 2.1 sec^{-1}).

He found that the onset of crystallization occurs at the inflection point in the stress-strain curve, a point which shifts to higher strain levels and lower stress levels as strain rate decreases.

Blundell, et al.[10] and Mahendrasingam, et al.[26, 27] have looked at the evolution in structure of PET during deformation using synchrotron radiation in order to determine precisely when crystallization occurs. Their results indicate that crystallization does not begin until the end of draw, but that it occurs very rapidly as soon as motion has ceased. These results contradict what other researchers have concluded, but Blundell, et al. find that crystallization occurs so rapidly that attempts in earlier research to quench the specimen mid-experiment to determine crystallinity was ineffective. Regardless of whether crystallization occurs during draw or immediately after, there is a form of high-order molecular orientation and organization which occurs during drawing which greatly contributes to the material strain hardening. The crystallization which occurs as a result of the deformation, as well as any additional crystallization due to annealing both serve to enhance the stiffness and strength of the polymer.

Much of the research into deformation of PET has been conducted with uniaxial and biaxial tension experiments. Duckett, Rabinowitz, and Ward[20] investigated how the tensile yield stress of PET depended on strain rate and temperature. Their results indicated that yield stress increases monotonically with increasing strain-rate and with decreasing temperature.

Gordon, Duckett, and Ward[22] conducted drawing experiments on PET in two stages and observed changes in density and birefringence, as well as stress-strain behavior. Their tests were all conducted in the glass transition region (70 ° C to 90 ° C). They concluded that the behavior could be described by the deformation of a molecular network and were able to approximate changes in refractive indices and stress using the Gaussian theory of rubber elastic photo-elasticity.

A notable series of papers by Chandran and Jabarin[24, 16, 17, 18] also contain results from uniaxial and biaxial extension experiments. In the first of these[24], uniaxial tension experiments were conducted on PET at temperatures in the range of
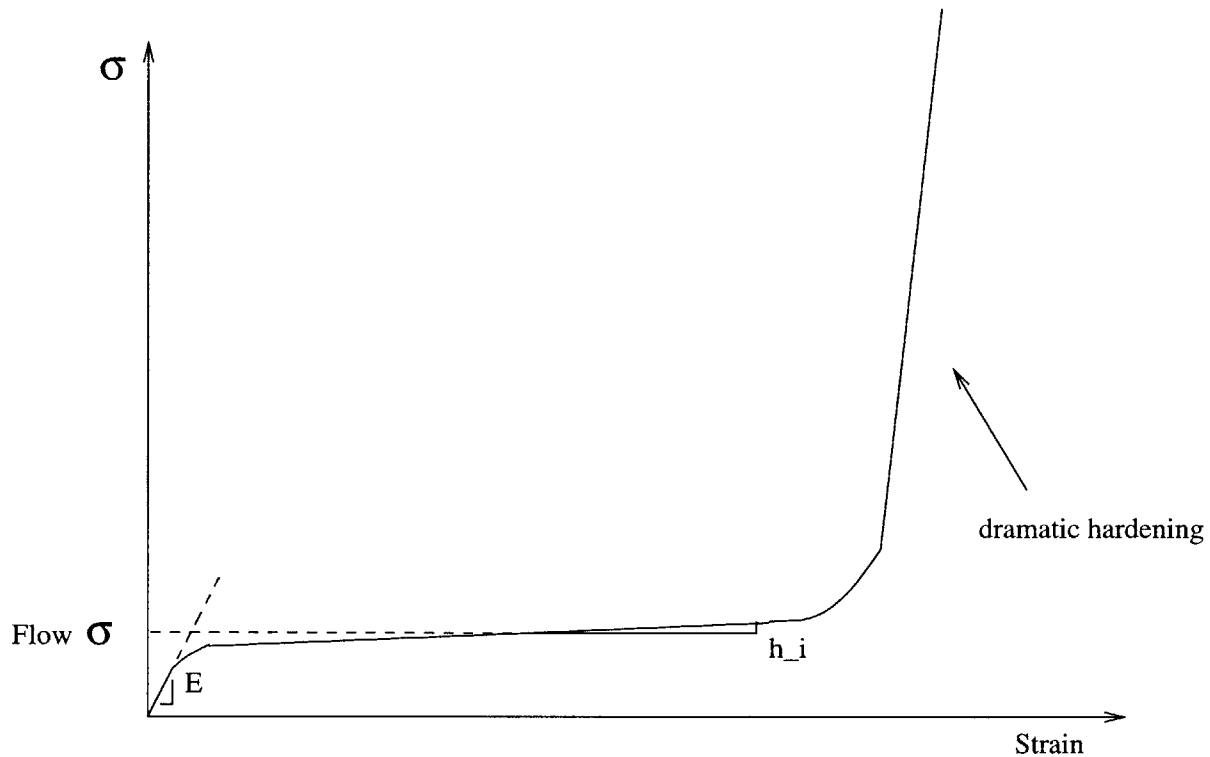
Figure 1-1: Generic stress-strain curve for PETG

80 ° C to 100 ° C and at extension rates from 5 mm/min to 127 mm/min. Birefringence after different annealing times was also examined. Results indicated that strain induced crystallization occurs during stretching and that it occurs even when samples are stretched to a final strain below the strain hardening region of the stress-strain curve (see figure 1-1).

In the later papers by Chandran and Jabarin, an extensive series of biaxial extension experiments were performed in order to examine the strain rate, temperature, and mode of deformation dependence of the stress-strain curve for PET. Their data provides a good benchmark for the behavior of PET film in biaxial extension because it includes such a wide variety of simultaneous as well as sequential experimental results.

Adams, Buckley, and Jones[1] performed biaxial extension tests with several different strain rate ratios and looked at the yield stress in each direction. Their results

confirmed the Mises yield criterion for PET in biaxial extension. The same research group has also published several papers related to constitutive modeling of the deformation of PET[2, 13, 14] which will be discussed in the next section.

Matthews, et al.[29] performed biaxial drawing experiments at one temperature, $85 °C$, over a range of strain rates from 10^{-4} sec^{-1} to .5 sec^{-1} for the purposes of fitting a constitutive model. Their model will also be discussed in the next section.

In other research, Cakmak, White, and Spruiell[15] conducted blow molding experiments. They looked at crystallinity along the length of a commercial soda bottle and also in laboratory bottles, where pressure and temperature could be varied. They showed that bottles processed by stretch blow molding possess relatively high crystallinity. Additionally, they found that the bottles exhibited anisotropic mechanical behavior through the bottle wall thickness. This is attributed to a higher transverse stretch on the inner wall surface than on the outer surface.

Axtell and Haworth[6] conducted blow-molding experiments in which they varied strain rate (.25 sec^{-1} to .95 sec^{-1}), temperature ($80 °C$ to $110 °C$), and inflation pressure. In their test setup, they were able to ensure a constant strain rate throughout the deformation and they noted a critical strain level where the stress growth function departed from a common baseline. They interpreted this as coinciding with the onset of strain induced crystallization.

A few workers have looked at the behavior of PET in compression tests, among them being Zaroulis and Boyce[35]. They performed tests on initially amorphous PET in uniaxial compression as well as plane strain compression and compared the results. Their experiments were in the glassy and glass transition regions, but not above the glass transition temperature. Strain rates were in the range of 0.005 sec^{-1} to 0.5 sec^{-1}. Their results showed a decrease in yield stress and flow stress as well as a small decrease in the strain hardening modulus with increasing temperature and decreasing strain rate. They performed differential scanning calorimetry (DSC) on the deformed specimens to determine the occurrence of strain-induced crystallization. They found that the material does not crystallize below the glass transition temperature, but that at $80 °C$ the material does crystallize upon deformation. In comparing the plane

strain and uniaxial deformation modes, they observed that plane strain specimens exhibit an increase in yield stress and a larger strain hardening behavior than uniaxial specimens.

In quite recent work, Llana and Boyce[25] published a large quantity of experimental data for PET deformed in uniaxial compression and plane strain compression experiments over a wide range of temperatures ($80\,^\circ$C to $110\,^\circ$C) and strain rates ($.001$ sec^{-1} to 1.0 sec^{-1}). They examined the final crystallinity by means of differential scanning calorimetry and wide angle x-ray diffraction techniques and found that crystallinity increased with increasing strain rate and decreasing deformation temperature in both deformation modes.

Overall, relatively little work has gone into determining the effect of pressure on the behavior of PET. One exception is Guan, Wang, and Porter[23], who investigated the difference between the effect of a tensile stress with that of a compressive stress. They determined that in forging (compression) a higher degree of crystallinity is obtained than in tension. One thing to note is that since their experiments were conducted at constant extension rate, in forging true strain rate increased with increasing strain level whereas in tension true strain rate decreased with increasing strain level, making it unclear whether the increased crystallinity was due to the evolving strain rate or the different mode of deformation. Because of variations in material properties of materials obtained from different suppliers, it is difficult to directly compare the tensile and compressive data found in the literature. Future work needs to be done in this area.

In an unpublished paper, Patton[31] presented some of the limited data available on PETG. Her research consisted primarily of uniaxial compression experiments at temperatures above the glass transition and was augmented with a few plane strain experiments. No major conclusions were drawn from the research.

1.2 Constitutive Modeling Background

Several attempts have been made to model various aspects of polymer deformation. Much of this effort has gone into modeling PET by considering a microstructural picture of an orienting molecular network. The models then incorporate the principles of rubber elasticity. This general topic of rubber elasticity has been investigated by several groups. Edwards and Vilgis[21] examined the effect of entanglements in rubber elasticity and developed a constitutive model to account for the competing effects of chain slippage during deformation and chain inextensibility.

An alternative approach to this is that taken by Arruda and Boyce[4], in which the large stretch behavior of amorphous polymers is taken to depend on a limiting extensibility of the polymer chains. They used an 8-chain model in a unit cube, to take advantage of symmetry, and applied a non-Gaussian (Langevin) statistical model, which has as inputs only two material parameters: a rubbery modulus, and a limiting extensibility parameter, or locking stretch.

In rather early work, Duckett, Rabinowitz, and Ward[20] applied a phenomenological yield model to poly(methyl methacrylate) (PMMA) and extended the results for the yield behavior of PET. They found that yield in PET followed the same general trend as for PMMA, namely, that yield stress increases monotonically with increasing strain rate and decreasing temperature.

Matthews, Duckett, Ward, and Jones[29] developed a constitutive model using the Ball[7] model for rubber-like behavior. Their model does not account for strain hardening very well and was only fit to biaxial experimental data at 85 °C over a range of strain rates and so does not account for temperature dependence. The model accounts for the rate dependence of the polymer behavior by making the entanglement density a linear function of the logarithm of the shear strain rate.

In preliminary work on PET, Buckley and Jones[13] developed a glass-rubber constitutive model for general amorphous polymers near the glass transition. This model captures the yield and initial flow features of the constitutive behavior, but provides for little or no strain softening and does not attempt to include the effects

of strain induced crystallization. In later work, Buckley, Jones, and Jones[14] applied this same constitutive model to data from biaxial experiments on PET. The model effectively captured the middle range, but was not very effective at simulating initial yield, large extensions, nor unloading behavior of the polymer.

Bergstrom and Boyce[9] have recently completed work dealing with constitutive modeling for large strain behavior in elastomers. Their work specifically dealt with the time dependent aspect of the behavior and molecular relaxation. Their model followed the Doi and Edwards[19] approach of taking the primary relaxation mechanism to be one of chain reptation.

In very recent work, Boyce, Socrate, and Llana[12] have developed a constitutive model which captures many of the features of PET. Their model will be further explained in section 3.1, but it is one of the first models to attempt to capture the effects of strain induced crystallization.

Almost simultaneously, Adams, Buckley, and Jones[2] have produced a constitutive model based on data from their biaxial stretching experiments at a variety of temperatures above the glass transition. Their model approximates the data well and has features to account for strain induced crystallization, but their data was all gathered at the same constant extension rate of 1 sec^{-1}. As such, it is uncertain how well their model predicts material behavior at different strain rates. Also, they do not report on the unloading behavior predicted by their model.

It is clear that while there has been some work done in this area, we are still lacking a good three-dimensional constitutive model that fully accounts for the temperature and strain rate dependence of the material and which incorporates all of the features of initial yield, strain softening, strain hardening, and strain induced crystallization. In this thesis, a model is presented that attempts to capture all of the above for the non-crystallizing PETG. In future work, this model will be applied to PET and elements to account for crystallization will be added.

Chapter 2

Experimental Work

2.1 Material

The material used in all experiments was PETG 6763 supplied by Eastman Chemical Co. with a weight average molecular weight of 38,888. It was supplied in the form of 4 in. by 4 in. plaques of 1/8 in. nominal thickness, from which compression specimens were machined.

2.2 DSC

Differential scanning calorimetry (DSC) was performed using a Perkin Elmer DSC 7 at a constant heating rate of $10\,^\circ$C per minute. The equipment was calibrated with zinc and indium. DSC scans performed on the as-received material as well as on deformed material indicated that there was no crystallinity in the material, either before or after testing. DSC scans also identified the glass transition temperature for the material as $80\,^\circ$C.

2.3 DMA

Dynamic mechanical analysis (DMA) was performed on the as-received material. Specimens were cut using a Buehler Isomet cutoff saw at a very low cutting speed

so as to prevent aging of the material. Specimens were approximately 30 mm long, 3.2 mm wide, and 1 mm thick. In DMA experiments, an oscillating force is applied to the material at various frequencies and the response of the material is reported in the form of the shear and loss modulus. The samples were tested in the extensional mode at frequencies ranging from 1 Hz to 100 Hz and at temperatures ranging from 40 °C to 110 °C. The oscillating force had a mean value of 30 gf (.2943 N) with an amplitude of oscillation of 45 gf (.4415 N). The modulus data is shown in figures 2-1 and 2-2. The shift in the curve as frequency is varied demonstrates the strain rate dependence of the glass transition temperature. When the material is deformed at higher frequencies, which corresponds to higher strain rates, the glass transition temperature shifts to higher temperatures.

With a knowledge of the DMA testing frequency, the elastic modulus, the specimen dimensions, and the magnitude of the cyclic load, an equivalent strain rate can be computed at various points on the DMA curves. These data points can then be compared with results from other tests, such as constant strain rate compression experiments. This is discussed in further detail in section 3.2.1.

2.4 Compression Tests

2.4.1 Setup

Two kinds of compression tests were performed: uniaxial and plane strain. For the uniaxial tests, specimens were cut into circular disks 12.39 mm in diameter. For the plane strain experiments, samples measured 9.55 mm on each side. In each case, WD-40, a common lubricant, was applied to the compression platens and a sheet of teflon was placed in between the PETG and the compression platens to eliminate the effects of friction. Care was taken so that no WD-40 contacted the test specimens.

The specimens were brought to test temperature by use of an electric resistance heater. They were allowed to come to thermal equilibrium for a total of 20 minutes.

The compression experiments were performed using an Instron 1350 with servo-
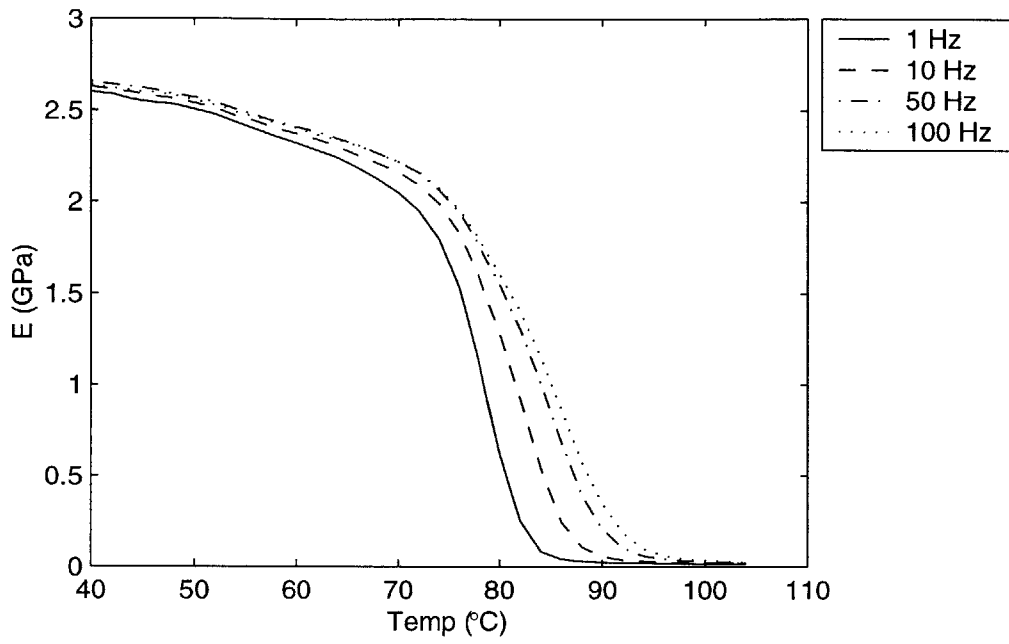
Figure 2-1: DMA Data
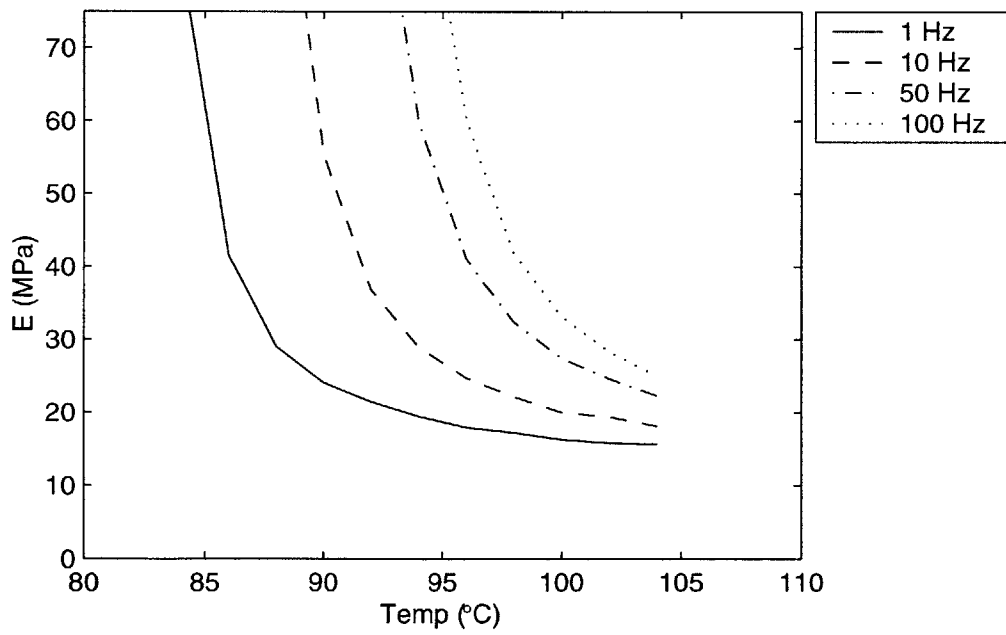
Figure 2-2: DMA Data, enlarged to show detail at high temperature

21

hydraulic controls. The cross head speed was controlled using a personal computer running Windows NT and LabView. The vertical specimen displacement was measured using an extensometer and was fed back to the computer in order to eliminate load train compliance error. Specimens were compressed at a constant logarithmic strain rate to final strains ranging from -0.8 to -2.0 for the uniaxial experiments and to final strains from -0.8 to -1.3 in the plane strain experiments.

The load was measured and acquired by standard data acquisition software during the experiments. True stress was determined from the initial cross-sectional area and by assuming no volume change for the polymer during plastic deformation.

Each test was performed at least twice in order to ensure repeatability. Tests were performed at strain rates ranging from $-.005$ sec^{-1} to -1.0 sec^{-1}. Attempting to perform experiments at higher strain rates raised the question of whether a constant strain rate could be achieved at such high rates using the test equipment. Temperatures were varied from 25 °C to 110 °C.

2.4.2 Results

The results are shown in the following figures and are discussed below. Figures 2-3 through 2-9 show uniaxial compression data at each temperature. Figures 2-10 through 2-15 show the same data plotted at constant strain rate. Figures 2-16 through 2-20 show the effect of unloading at different final strains in uniaxial compression.

From these figures it can be observed that PETG exhibits the following general trends. First, the material has an initially stiff response which is highly temperature dependent. The modulus decreases moderately with increasing temperature and fairly independent of strain-rate at temperatures below the glass transition temperature. In the transition region, the modulus drops dramatically with increasing temperature. This drop off occurs at higher temperatures for specimens deformed at higher strain rates. Above the transition region, the modulus continues to drop as temperature rises, but the change is more moderate. The dependence is also mildly strain-rate dependent in this region, with increasing strain rate leading to increased modulus.

Second, at temperatures below the glass transition temperature the polymer ex-

22

hibits a definite yield stress which increases with increasing strain rate and decreases with increasing temperature. This yield is followed by a considerable amount of strain softening. The amount of strain softening is relatively strain-rate independent, but increases with increasing temperature. At temperatures above the transition temperature, the stress-strain curves show the classic monotonic rise in stress with increasing strain (see figure 1-1). The yield stress is not so abrupt and instead the curve gently rolls over and the material begins to flow at a stress level on the order of 1-2 MPa. The magnitude of this flow stress also depends on strain rate and temperature. At higher temperatures and lower strain rates the roll over occurs at lower stress levels. Figures 2-21 through 2-24 show an enlarged view of the initial modulus and roll over to flow for the polymer above the glass transition temperature.

Figure 2-6 shows the data at 80 °C, approximately the glass transition temperature for PETG. This is a very interesting set of curves, in that it demonstrates the strain rate dependence of the glass transition temperature nicely. At high strain rates, the material is still below the transition temperature at 80 °C and exhibits the high yield stress and strain softening characteristic of polymers in the glassy state. At low strain rates, however, there is no apparent yield stress and the stress-strain curve rises monotonically. This indicates that at these strain rates the polymer is already above its glass transition at 80 °C and hence exhibits rubbery polymeric behavior.

Third, after the strain softening region, or roll over to flow above the transition temperature, the polymer begins to strain harden as the strain level is increased. The material then begins to undergo the competing effects of strain hardening and molecular relaxation. This hardening is evident in the initial hardening modulus, h_i, in the flow region followed by the dramatic upturn in the stress-strain curve as the polymer chains start to reach their limiting extensibility or locking stretch. Molecular relaxation occurs simultaneously as the polymer chains slide through the tangled web of neighboring chains using a mechanism referred to as chain reptation.

In the constant strain rate figures (figures 2-10 to 2-15) the temperature dependence of the material is clearly discernible. At each of the strain rates, the initial yield or initial flow stress decreases as temperature increases. The hardening slope

23

decreases with increasing temperature and the strain at which the dramatic upswing in stress occurs is greater at higher temperatures. This is because of the thermally assisted molecular relaxation occurring in the polymer. As the temperature increases, the molecules have more thermal motion and can therefore more easily slide between each other and the neighboring entanglements.

Figures 2-16 to 2-20 show the material response as it is unloaded at different final strains. The data shows good repeatability and shows that at temperatures above the glass transition, much of the deformation is recovered upon unloading regardless of the final strain. Experimentally, it is difficult to determine how much of the deformation is actually recovered because upon unloading the bottom surface of the specimen remains in contact with the compression platen while the top surface is air quenched. This causes the rubbery specimens to curl up due to the thermal gradient during unloading so that the final specimen dimensions are difficult to measure. The effect is less pronounced in plane strain due to the test fixture remaining in contact with the specimen. Post test measurements using calipers indicate that the plane strain compression specimens recover to within 93% of their original height at temperatures above the glass transition. In contrast, at temperatures below the glass transition very little (on the order of 10 to 15 %) of the strain is recovered at all final strain levels.

Figure 2-7 demonstrates the strain rate dependence of strain recovery. Less recovery is observed upon unloading at lower strain rates than at higher strain rates. This is because at low rates more of the deformation is accommodated by molecular relaxation than at high rates, where deformation is due primarily to network orientation. Since the deformation due to molecular relaxation is permanent and the deformation due to orientation is recoverable, specimens which are deformed at higher rates are able to recover more. Again, due to the quenching phenomenon, it is difficult to pinpoint exact numbers, but at 90 ° C, the material recovers by approximately 75% at -1.0 sec^{-1} and only recovers by 45% at -.005 sec^{-1}.

Each of these trends is consistent with the trends exhibited by PET, with the exception of strain recovery[25, 35]. PET exhibits substantially less recovery at temper-

atures above the glass transition due to strain-induced crystallization. For example, at 90 °C, -1.0 sec^{-1} PETG recovers by approximately 75%, whereas PET under the same conditions undergoes less than 50% recovery.

Figures 2-25 through 2-28 show plane strain compression data at each temperature. Figures 2-29 through 2-34 show the same data plotted at constant strain rate.

The plane strain compression data indicates the same trends as were observed in the uniaxial compression data. In figures 2-35 through 2-38 the comparison of plane strain with uniaxial deformation modes is depicted. In figure 2-35 it is important to note that the room temperature plane strain data appears to have a rather compliant initial response as evidenced by the lower initial modulus in plane strain than in uniaxial compression. The initial elastic response in plane strain should, in fact, be higher. This indicates that there is some additional compliance in the plane strain fixturing which is not present in the uniaxial setup. If a correction were made for this, the plane strain curves would be shifted to the left by as much as 10 percent.

It is also interesting to note that the higher rate data exhibits the effects of thermal softening due to adiabatic heating during deformation. This effect is present in both uniaxial compression and plane strain compression, but is more pronounced in plane strain due to the larger stress levels in the material. This effect manifests itself in the crossover of the stress-strain curves at large strains. For example, in figure 2-25, this can be observed as the -0.5 sec^{-1} data crosses over the -0.05 sec^{-1} data at a strain level of about -0.9. In the absence of thermal softening, the higher rate data would be expected to sustain a higher stress level throughout the deformation.

Figures 2-35 through 2-38 also demonstrate that in plane strain compression, the material begins to strain harden at a lower logarithmic strain level than in uniaxial compression. Note that if the correction for test fixture compliance were included, this effect would be even more pronounced. In modeling polymer deformation, Arruda and Boyce[4] considered an effective chain stretch to account for state of strain dependence of strain hardening, where the amount of stretch a polymer chain will undergo during deformation depends on the strain state. The effective chain stretch at a particular nominal axial strain level is greater in plane strain compression than in uniaxial
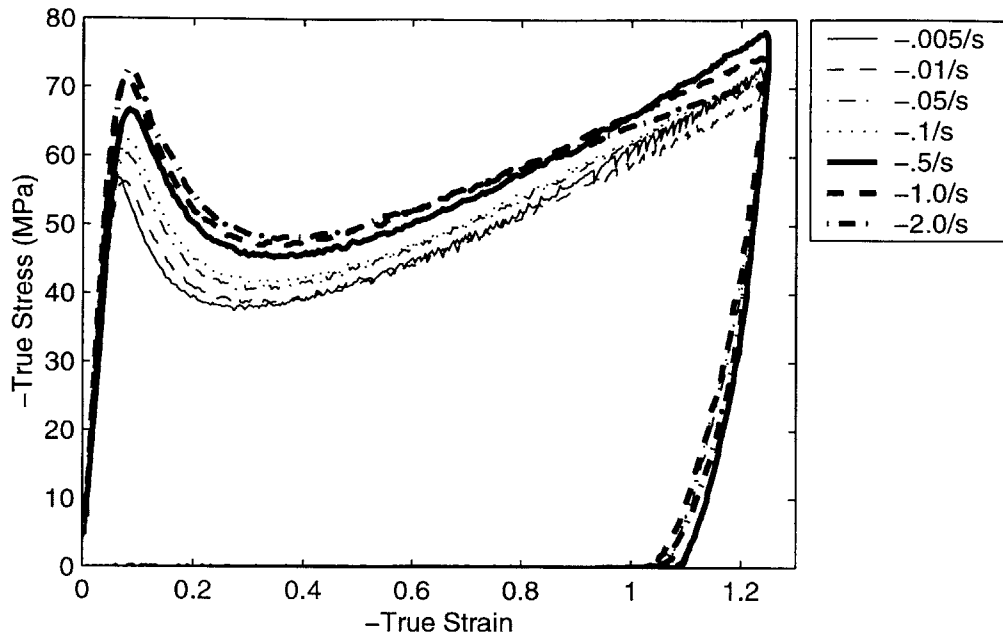
Figure 2-3: Uniaxial Compression Data, Temperature = 25 ° C

compression. Since the hardening behavior of the polymer is presumably a function of this chain stretch, it is consistent for the plane strain curves to exhibit earlier hardening behavior than the uniaxial compression curves.
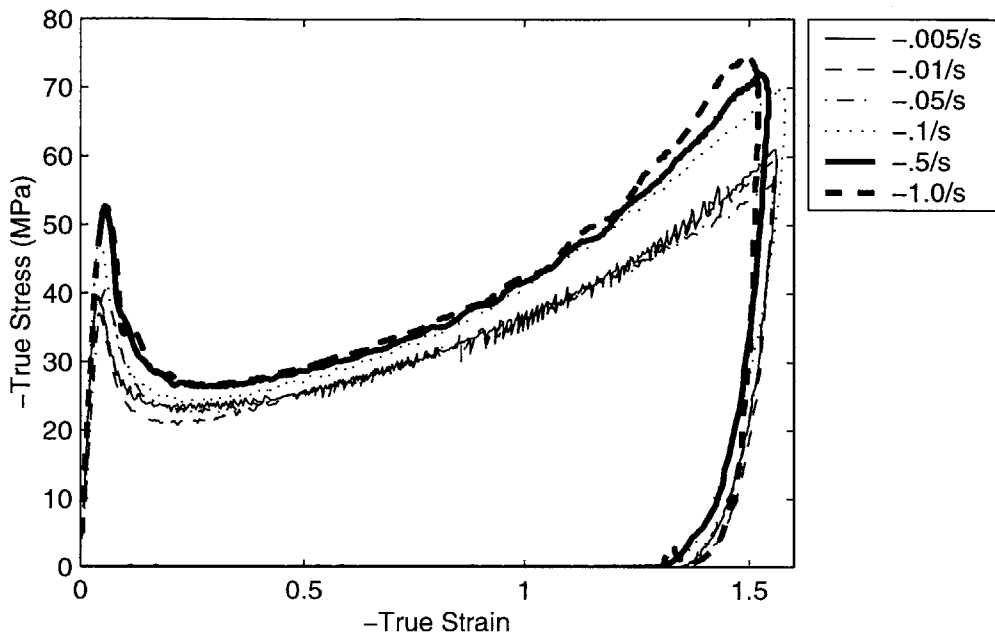
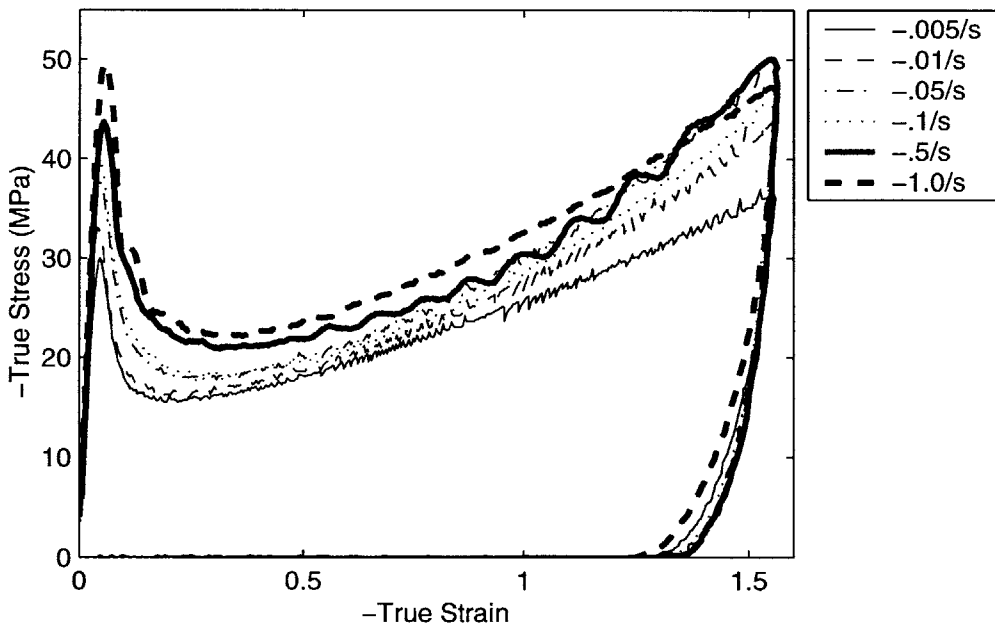Figure 2-4: Uniaxial Compression Data, Temperature = 60 ° C

Figure 2-5: Uniaxial Compression Data, Temperature = 70 ° C
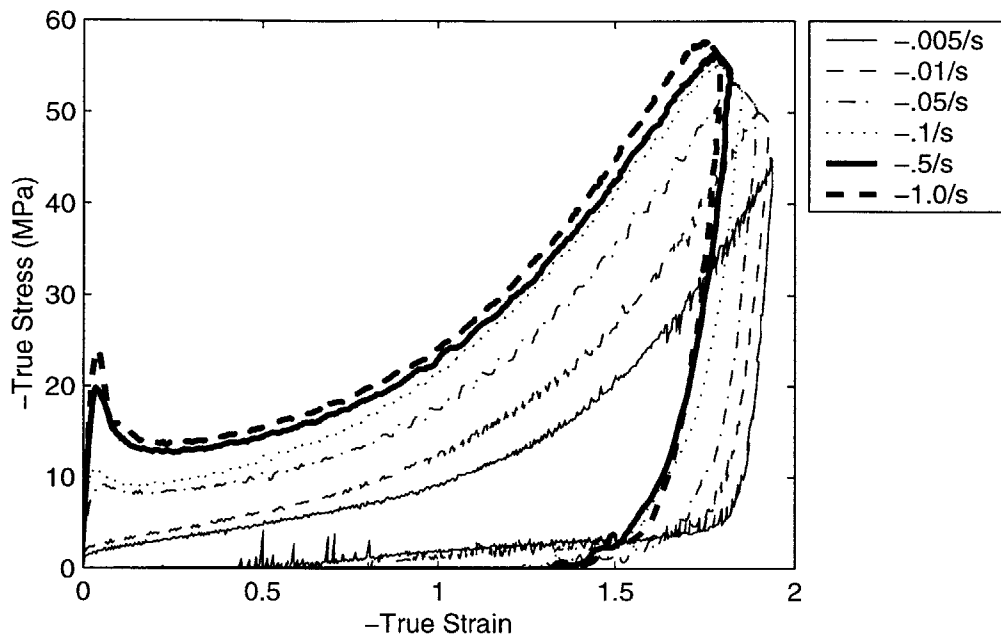
27

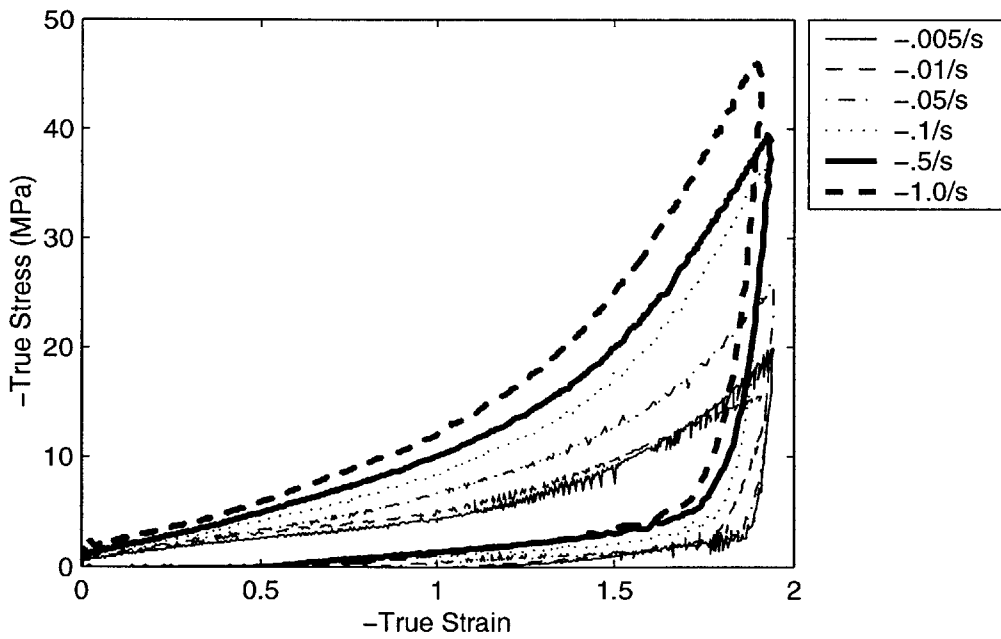Figure 2-6: Uniaxial Compression Data, Temperature = 80 ° C

Figure 2-7: Uniaxial Compression Data, Temperature = 90 ° C

28
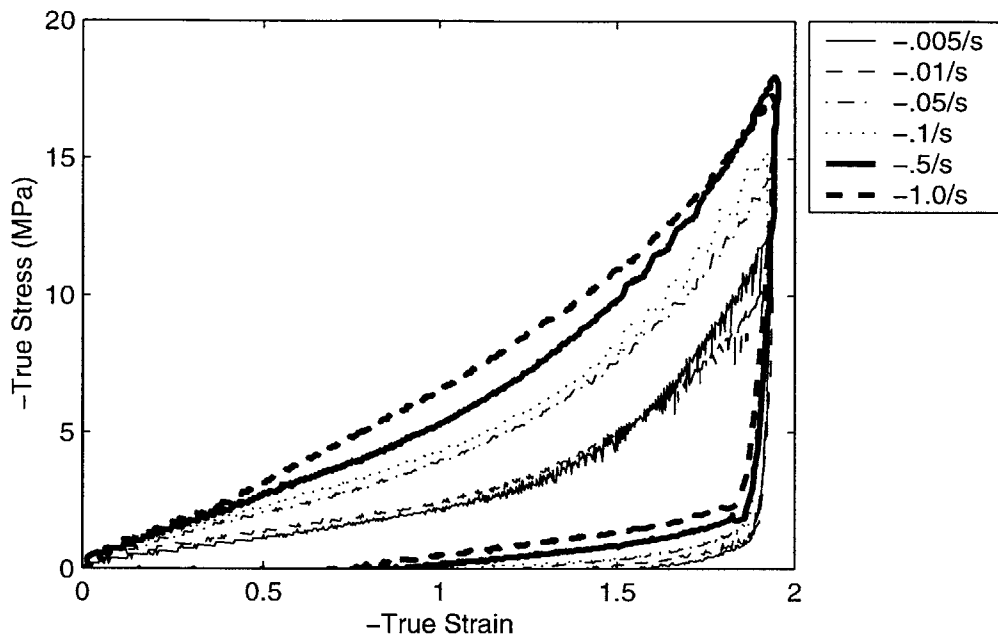
Figure 2-8: Uniaxial Compression Data, Temperature = 100 ° C
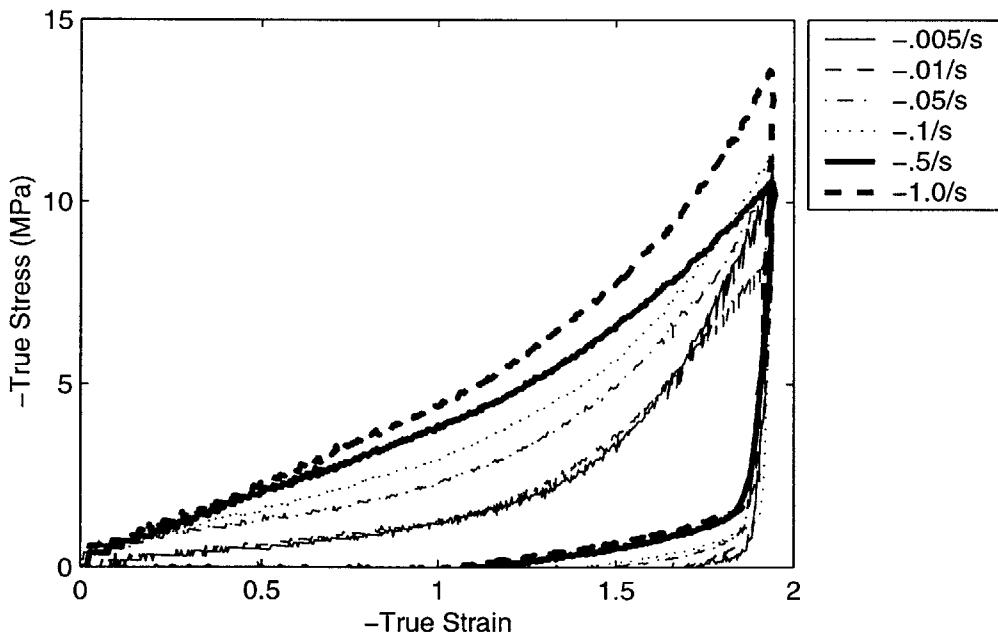
Figure 2-9: Uniaxial Compression Data, Temperature = 110 ° C
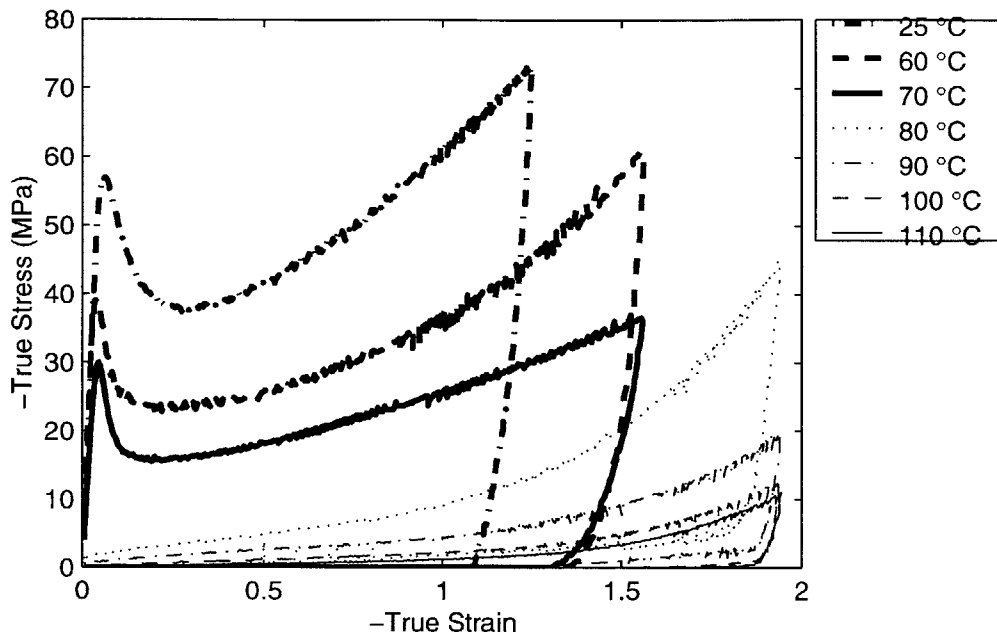
Figure 2-10: Uniaxial Compression Data, $\dot{\varepsilon} = -.005/\text{s}$
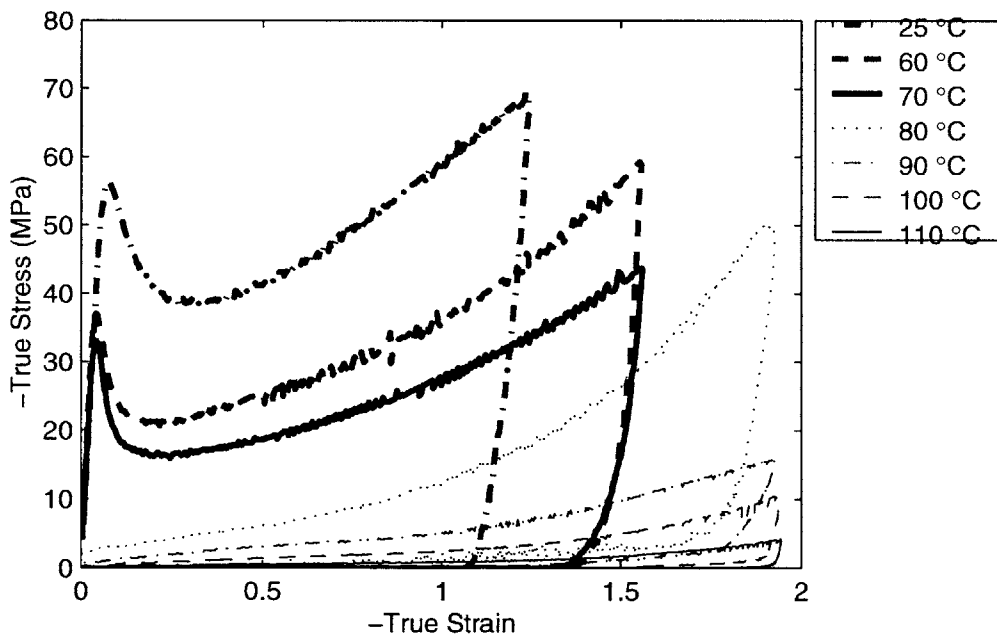
Figure 2-11: Uniaxial Compression Data, $\dot{\varepsilon} = -.01/\text{s}$

30
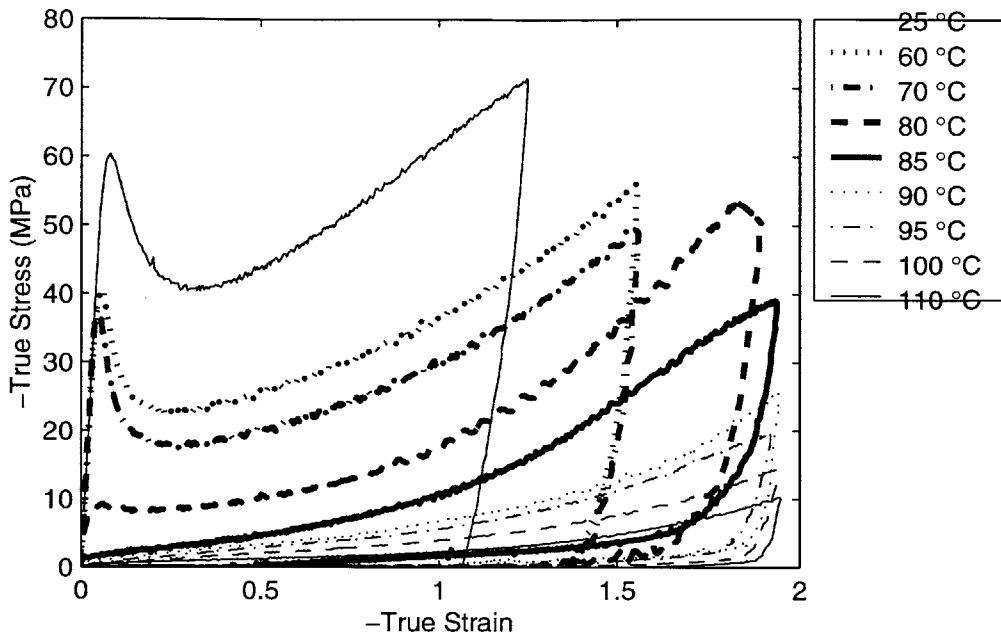
Figure 2-12: Uniaxial Compression Data, $\dot{\varepsilon} = -.05/\text{s}$
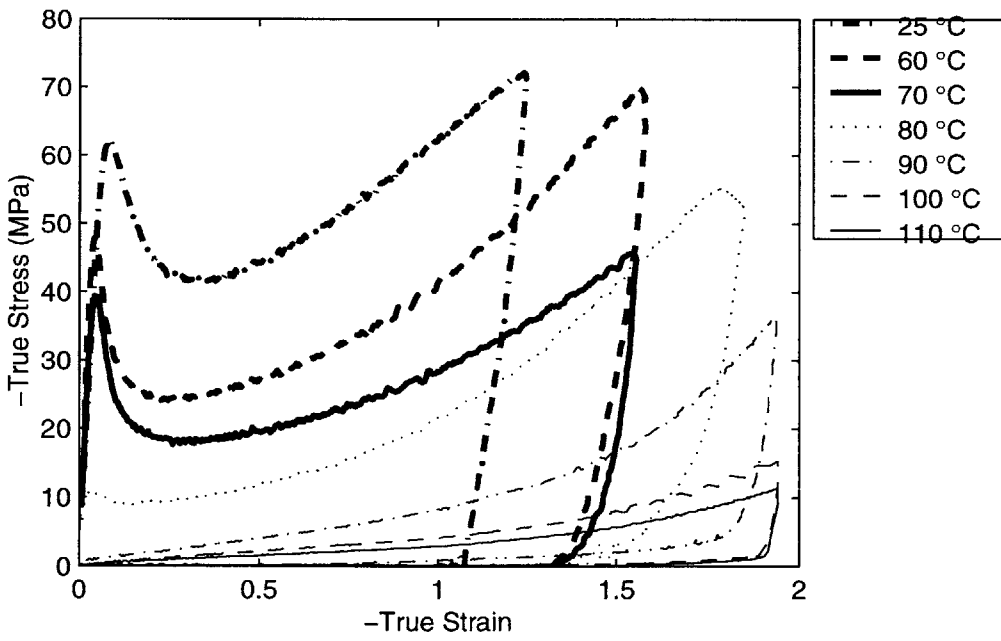
Figure 2-13: Uniaxial Compression Data, $\dot{\varepsilon} = -.1/\text{s}$

31
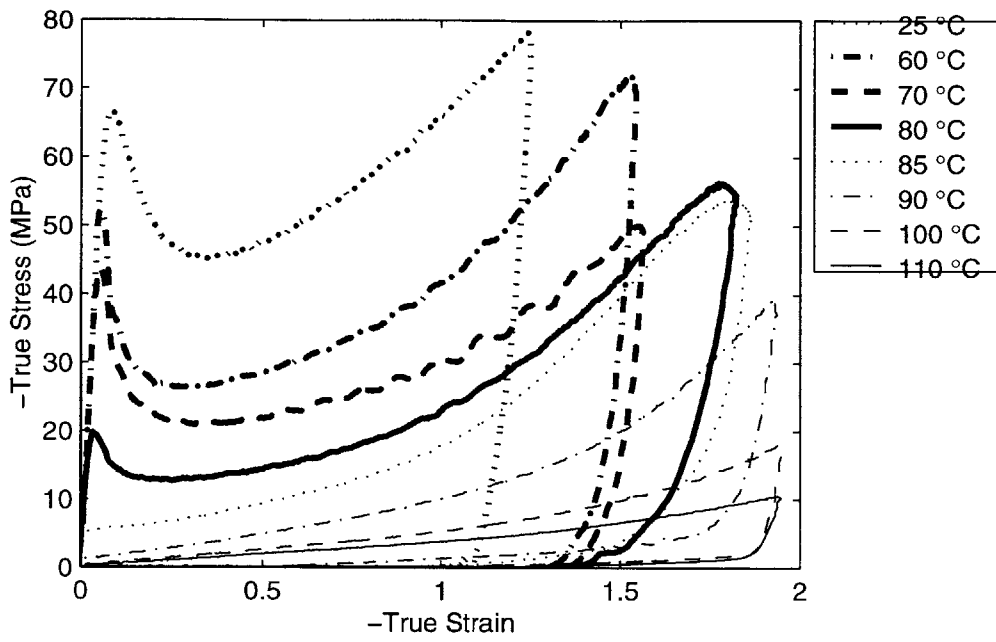
Figure 2-14: Uniaxial Compression Data, $\dot{\varepsilon} = -.5/\text{s}$
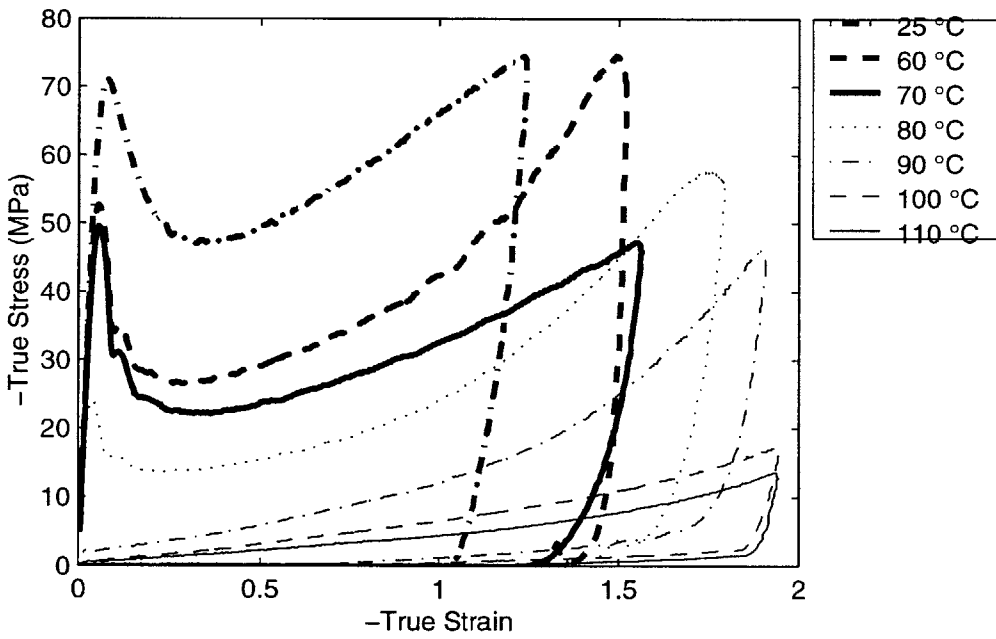
Figure 2-15: Uniaxial Compression Data, $\dot{\varepsilon} = -1.0/\text{s}$

32
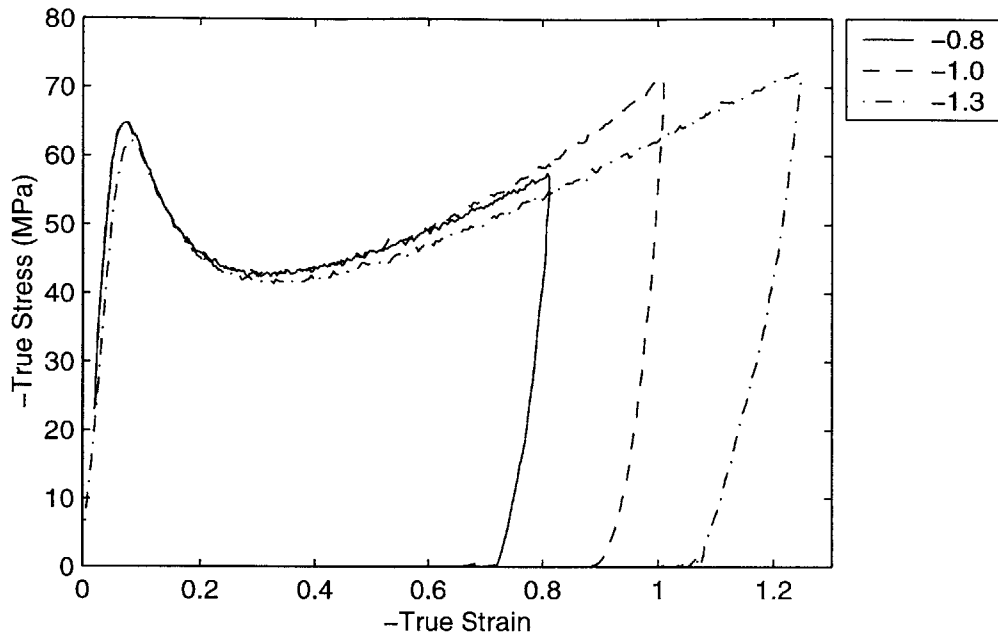
Figure 2-16: Uniaxial Compression Data, Temperature = 25 °C, $\dot{\varepsilon}$ = -.1/s, Loaded to different final strains
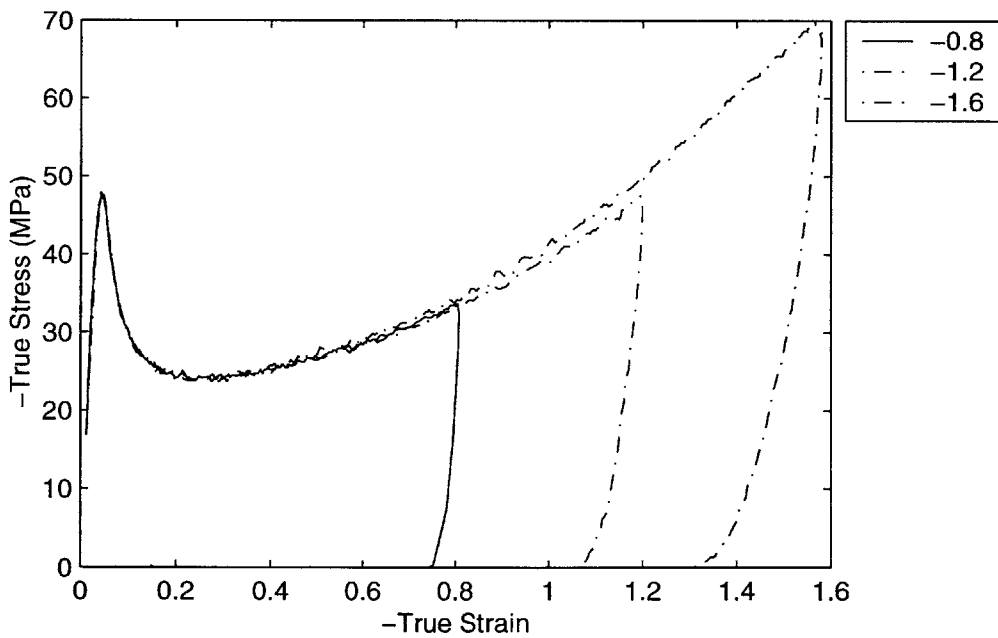
Figure 2-17: Uniaxial Compression Data, Temperature = 60 °C, $\dot{\varepsilon}$ = -.1/s, Loaded to different final strains
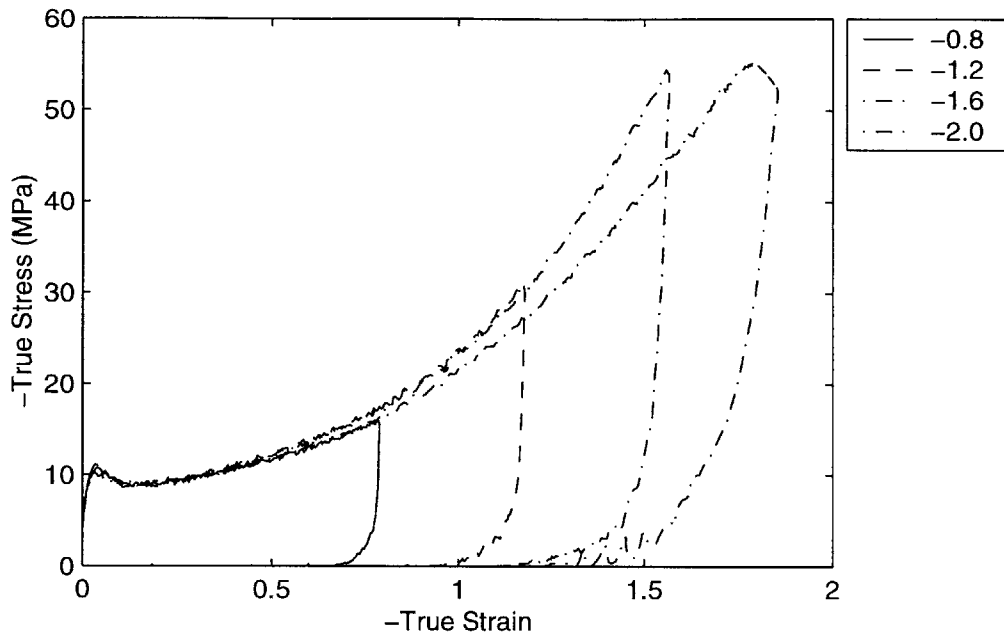
Figure 2-18: Uniaxial Compression Data, Temperature = 80 ° C, $\dot{\varepsilon}$ = -.1/s, Loaded to different final strains
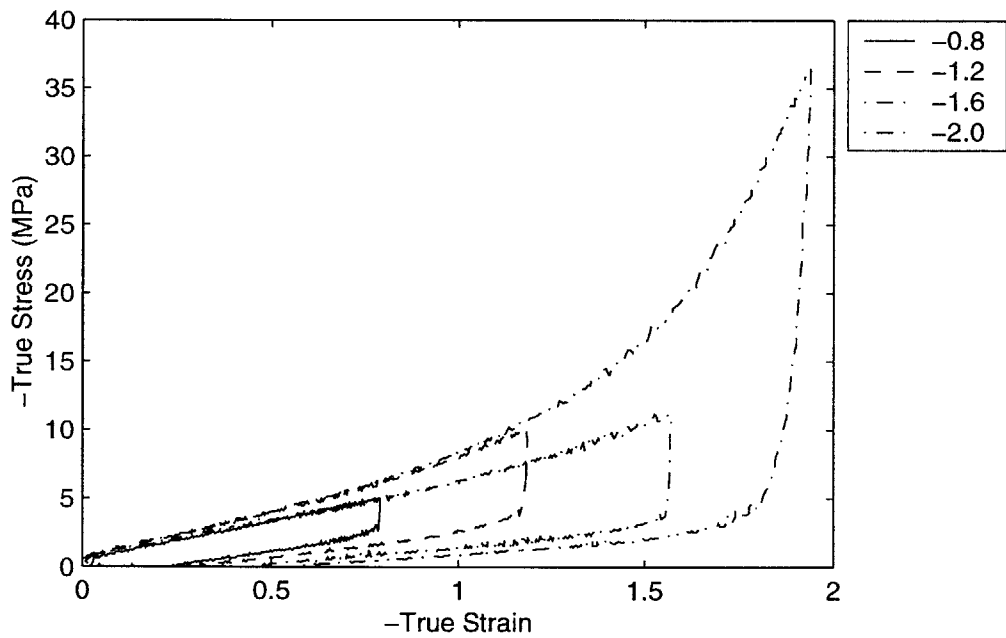
Figure 2-19: Uniaxial Compression Data, Temperature = 90 ° C, $\dot{\varepsilon}$ = -.1/s, Loaded to different final strains
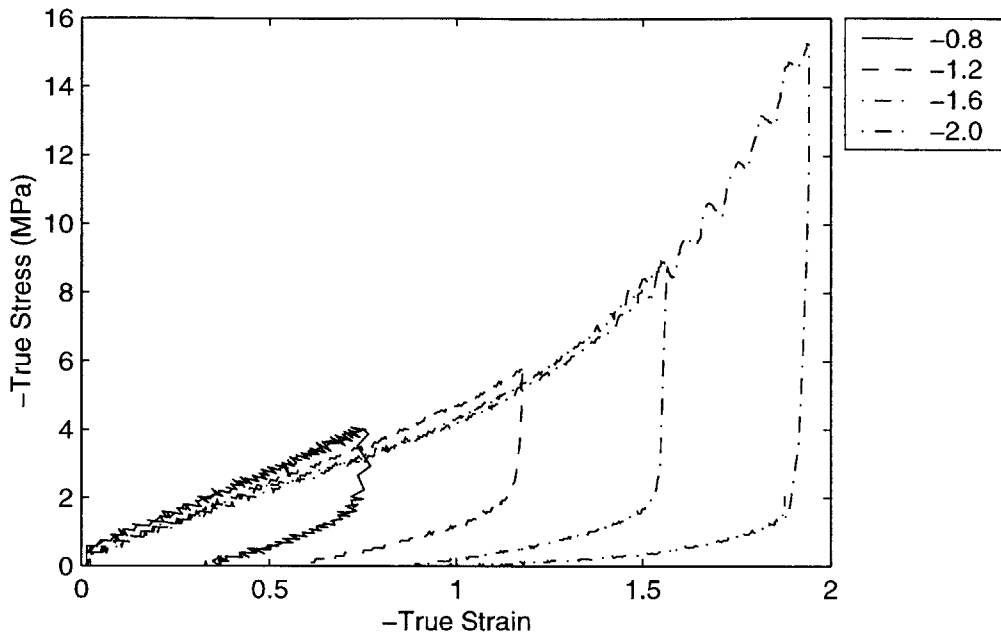
Figure 2-20: Uniaxial Compression Data, Temperature = 100 ° C, $\dot{\varepsilon}$ = -.1/s, Loaded to different final strains
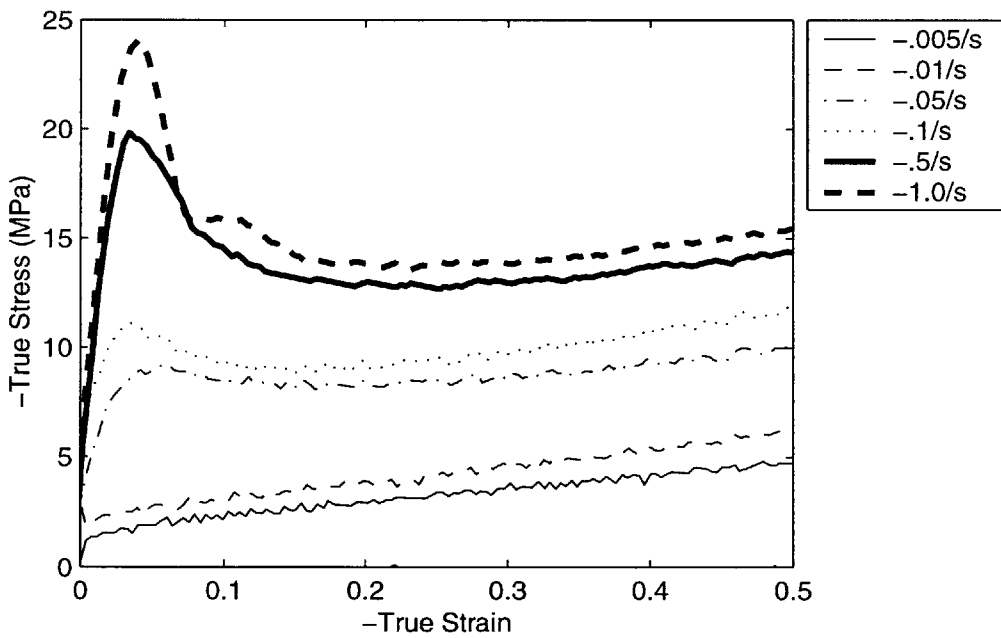
Figure 2-21: Uniaxial Compression Data, Temperature = 80 ° C, Enlarged to show initial modulus and flow stress
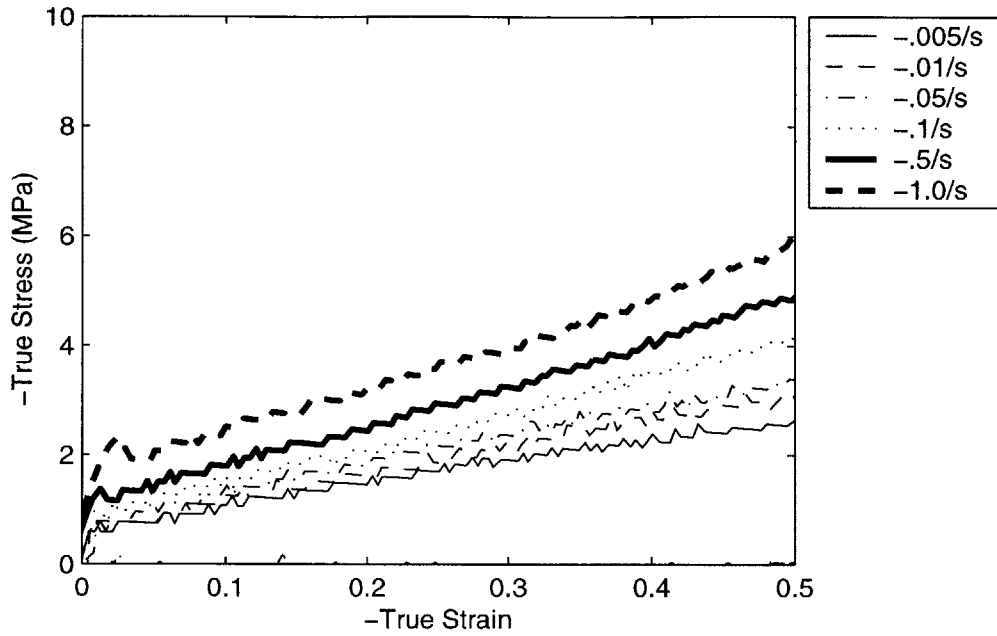
Figure 2-22: Uniaxial Compression Data, Temperature = 90 °C, Enlarged to show initial modulus and flow stress
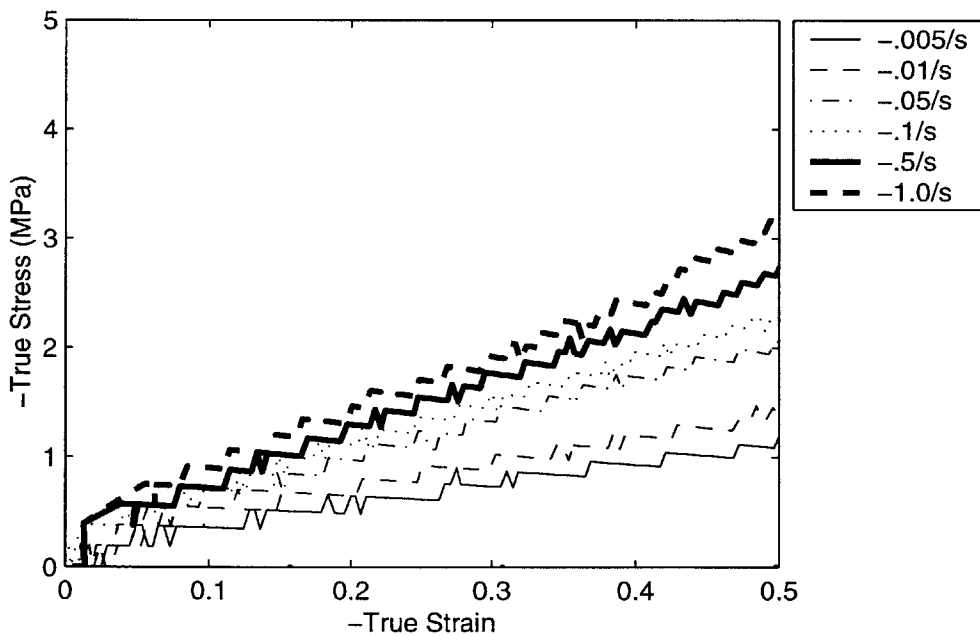
Figure 2-23: Uniaxial Compression Data, Temperature = 100 °C, Enlarged to show initial modulus and flow stress

36
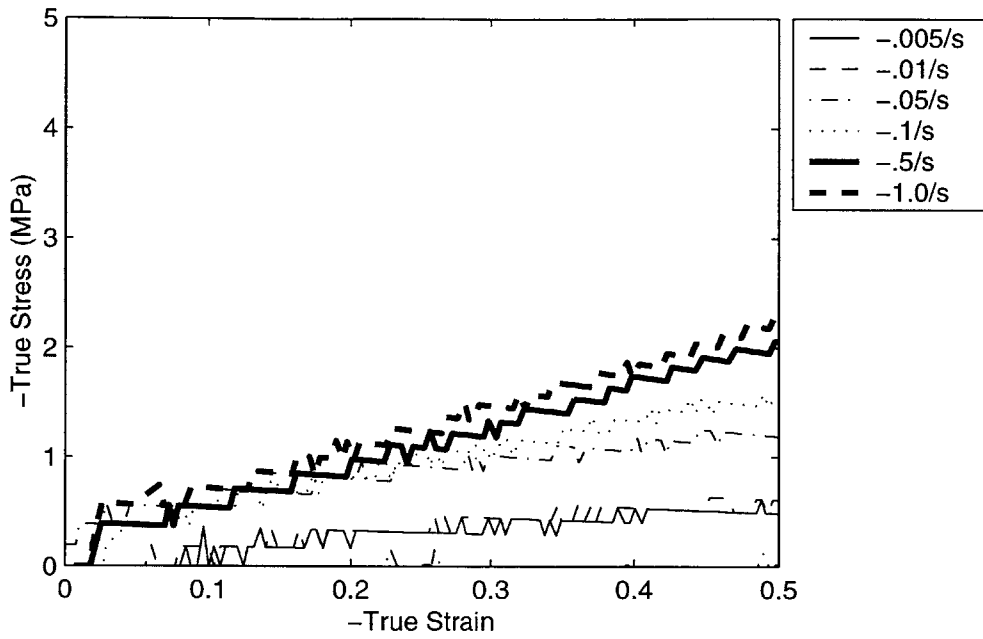
Figure 2-24: Uniaxial Compression Data, Temperature = 110 ° C, Enlarged to show initial modulus and flow stress
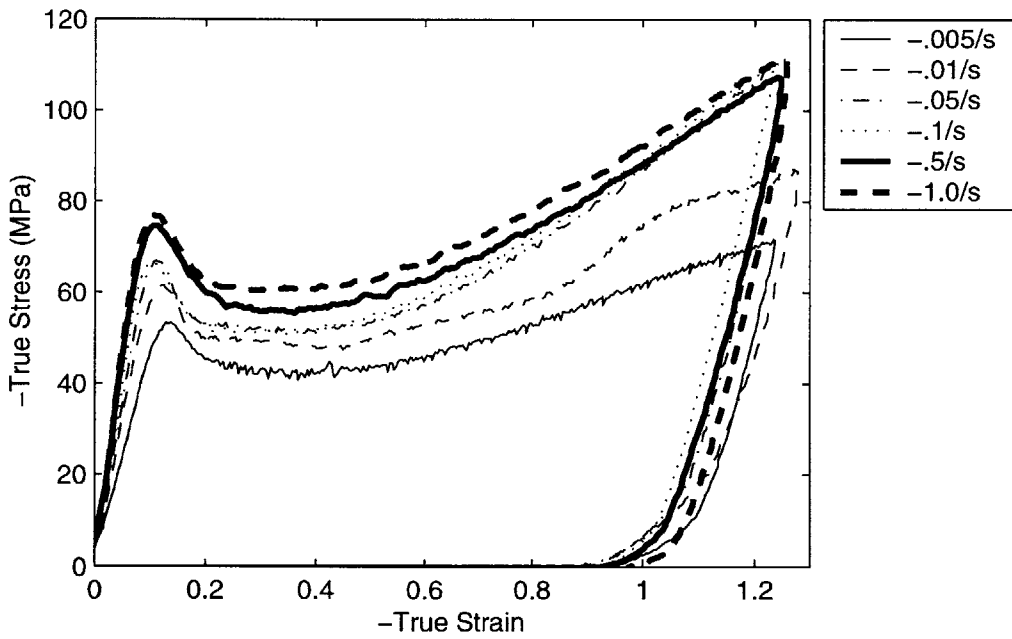
Figure 2-25: Plane Strain Compression Data, Temperature = 25 ° C
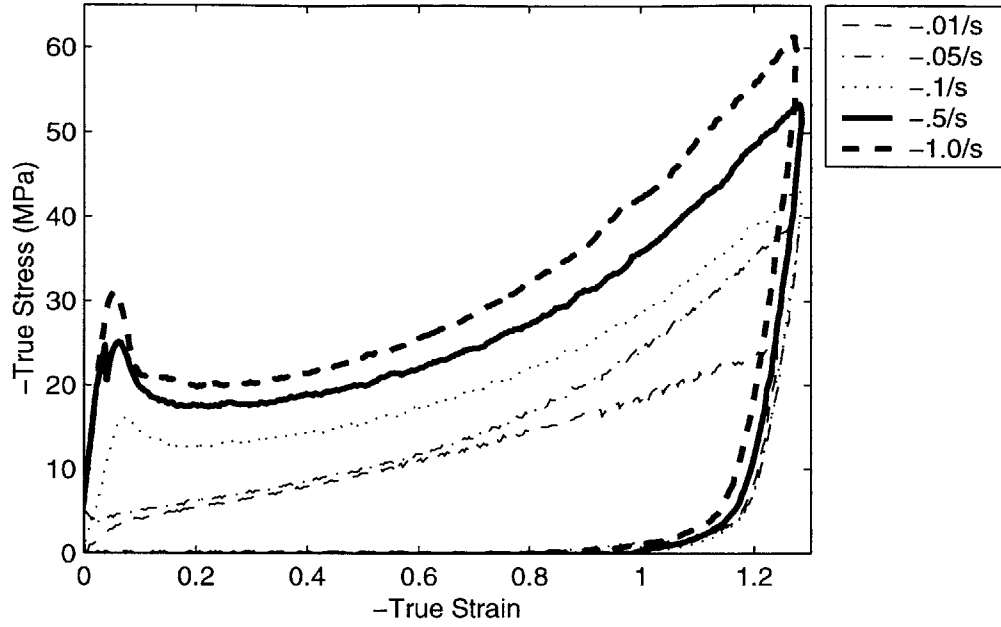
Figure 2-26: Plane Strain Compression Data, Temperature = 80 ° C
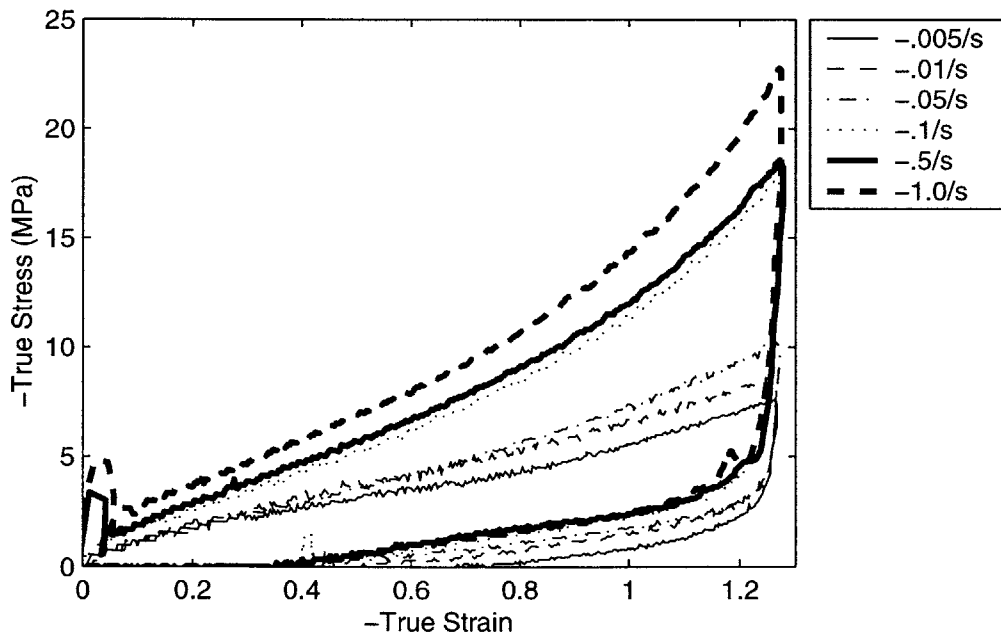
Figure 2-27: Plane Strain Compression Data, Temperature = 90 ° C
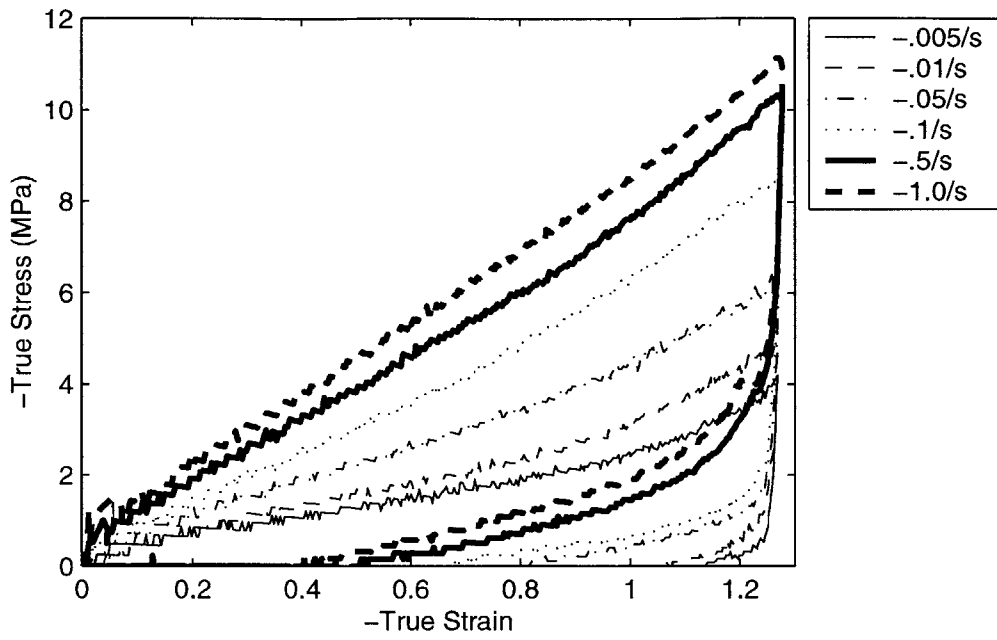
Figure 2-28: Plane Strain Compression Data, Temperature $= 100\,^\circ$ C
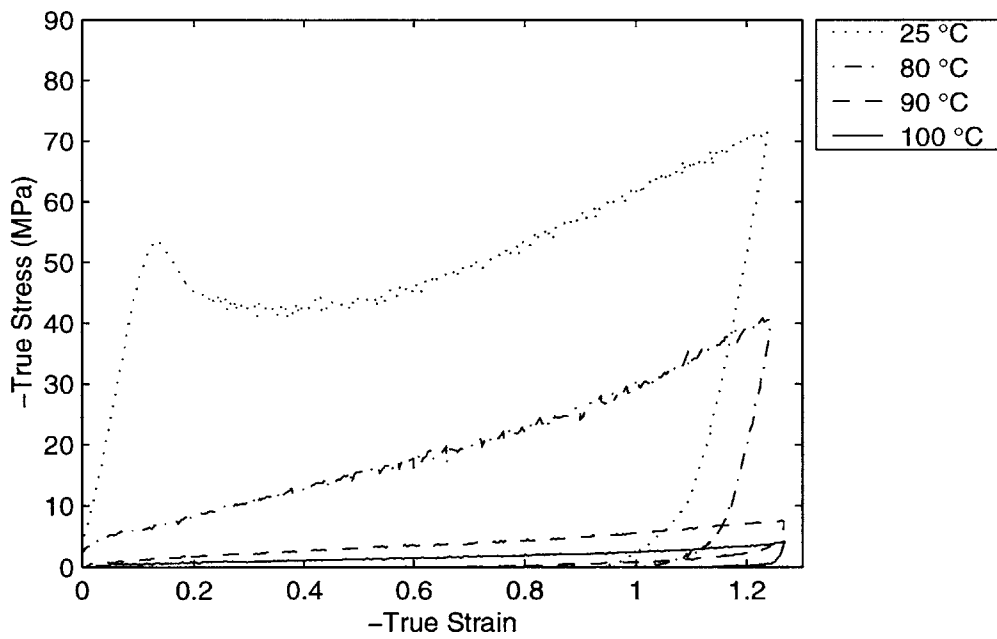
Figure 2-29: Plane Strain Compression Data, $\dot{\varepsilon} = -.005/\mathrm{s}$

39
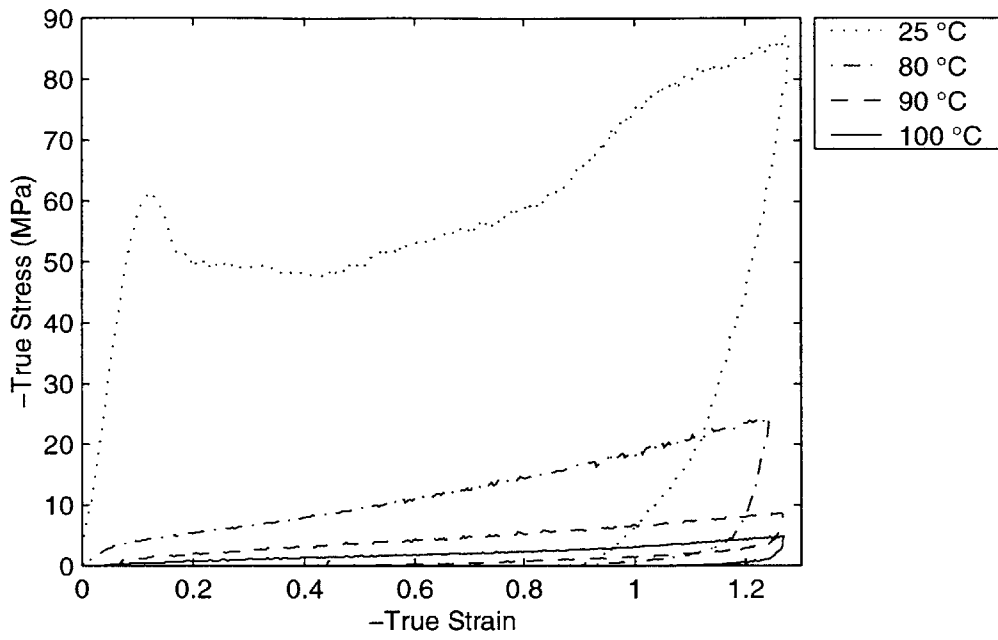
Figure 2-30: Plane Strain Compression Data, $\dot{\varepsilon} = -.01/s$
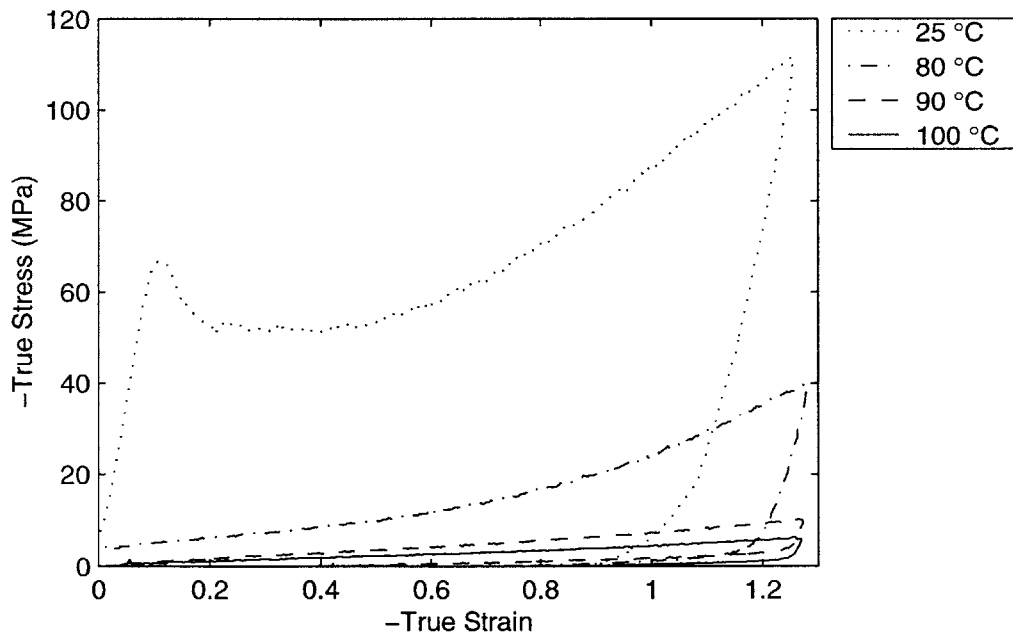
Figure 2-31: Plane Strain Compression Data, $\dot{\varepsilon} = -.05/s$

40
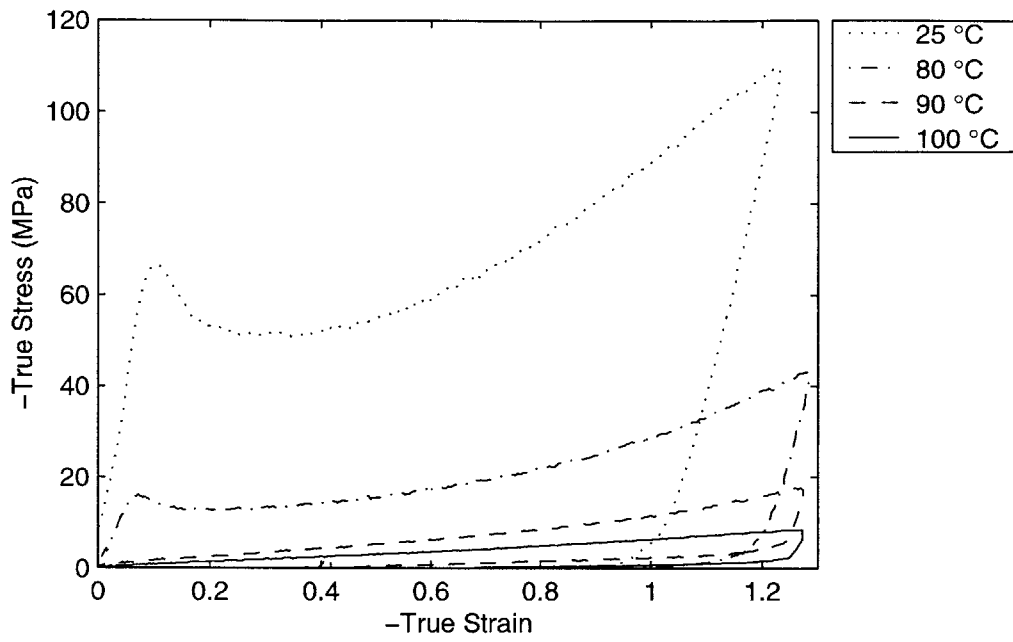
Figure 2-32: Plane Strain Compression Data, $\dot{\varepsilon} = -.1/\text{s}$
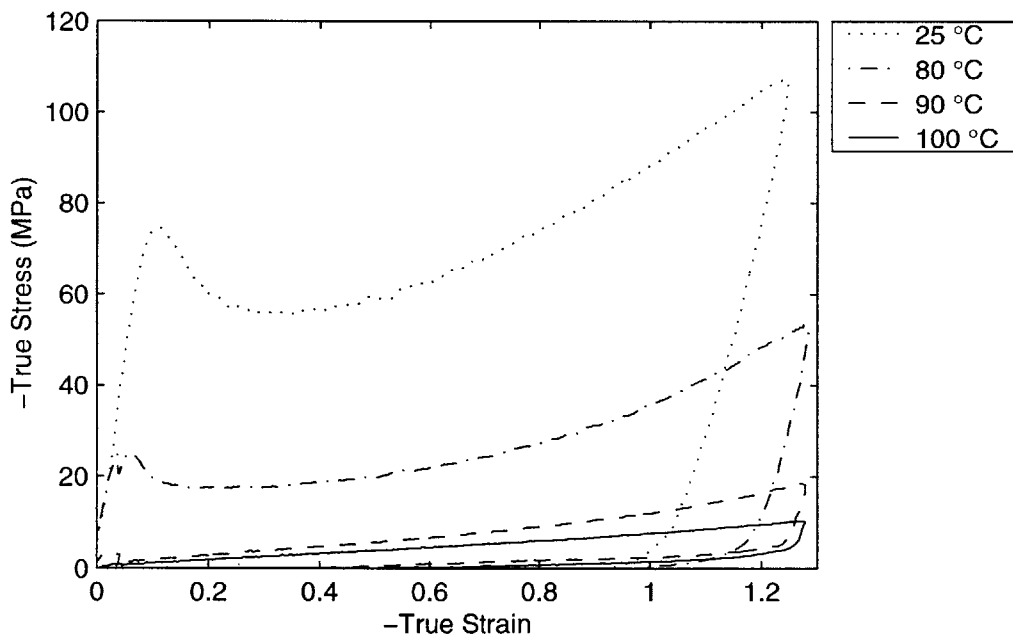
Figure 2-33: Plane Strain Compression Data, $\dot{\varepsilon} = -.5/\text{s}$
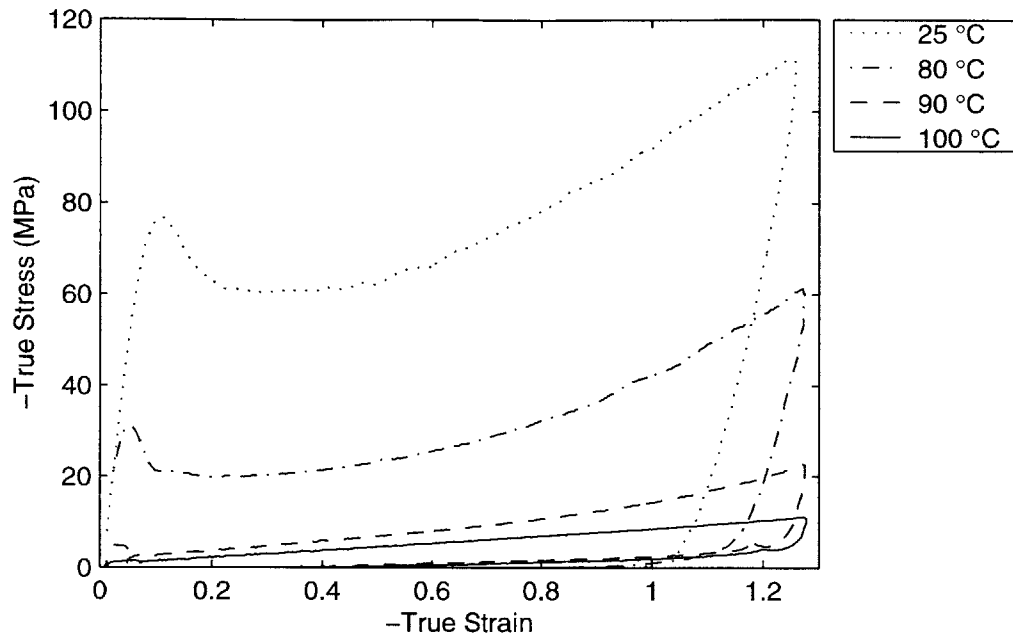
Figure 2-34: Plane Strain Compression Data, $\dot{\varepsilon} = -1.0/\mathrm{s}$
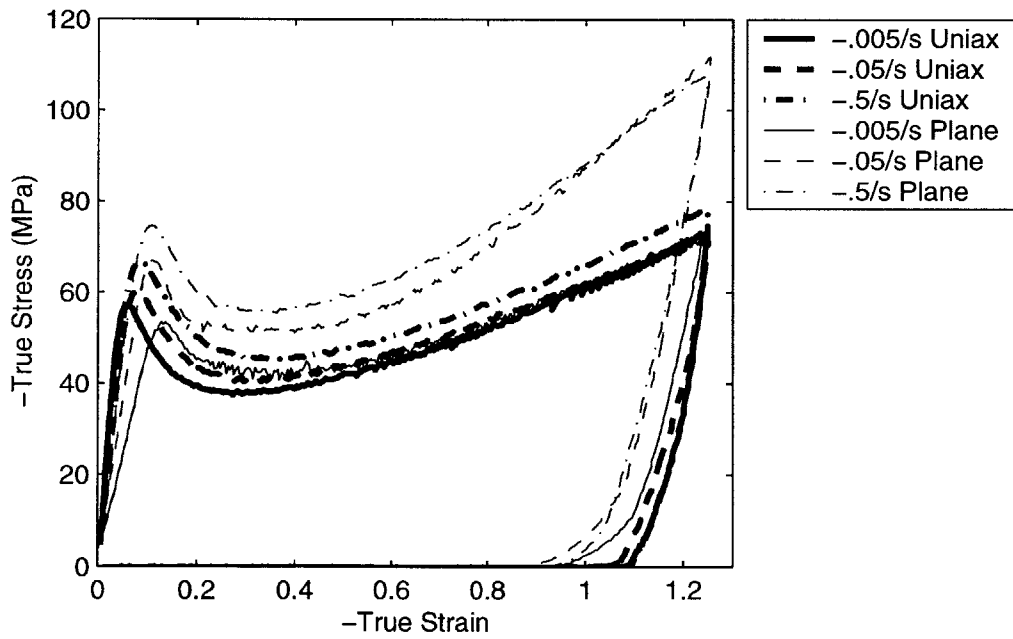
Figure 2-35: Uniaxial and Plane Strain Compression Data, Temperature $= 25\,^\circ$C

42
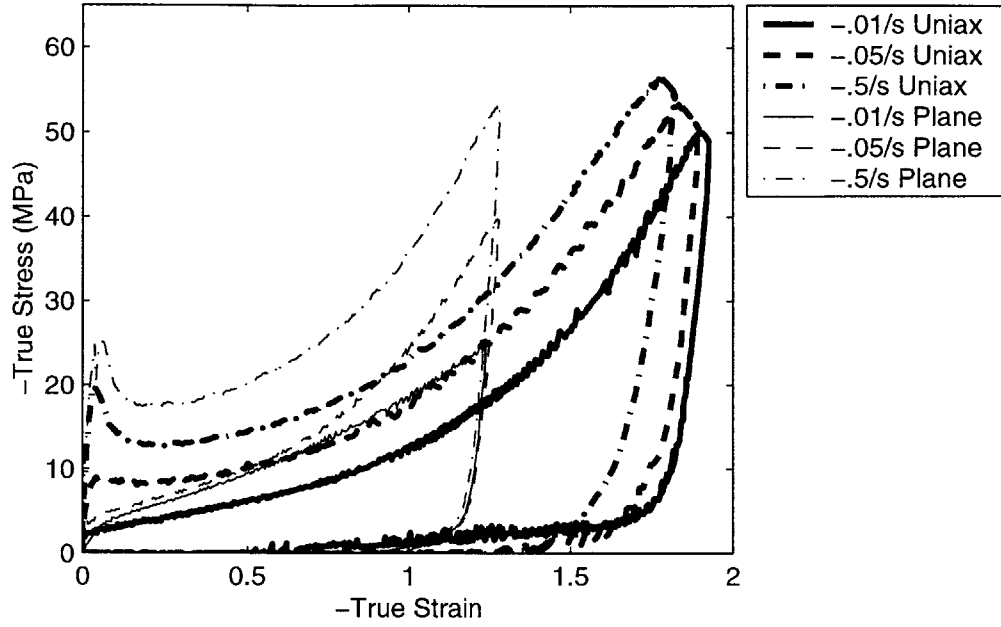
Figure 2-36: Uniaxial and Plane Strain Compression Data, Temperature = 80 ° C
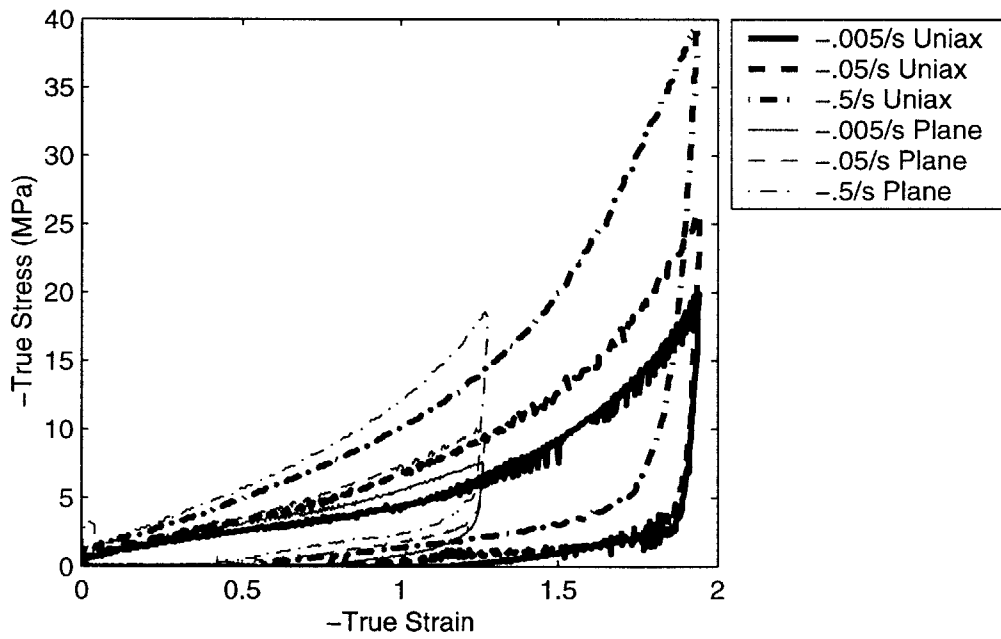
Figure 2-37: Uniaxial and Plane Strain Compression Data, Temperature = 90 ° C

43
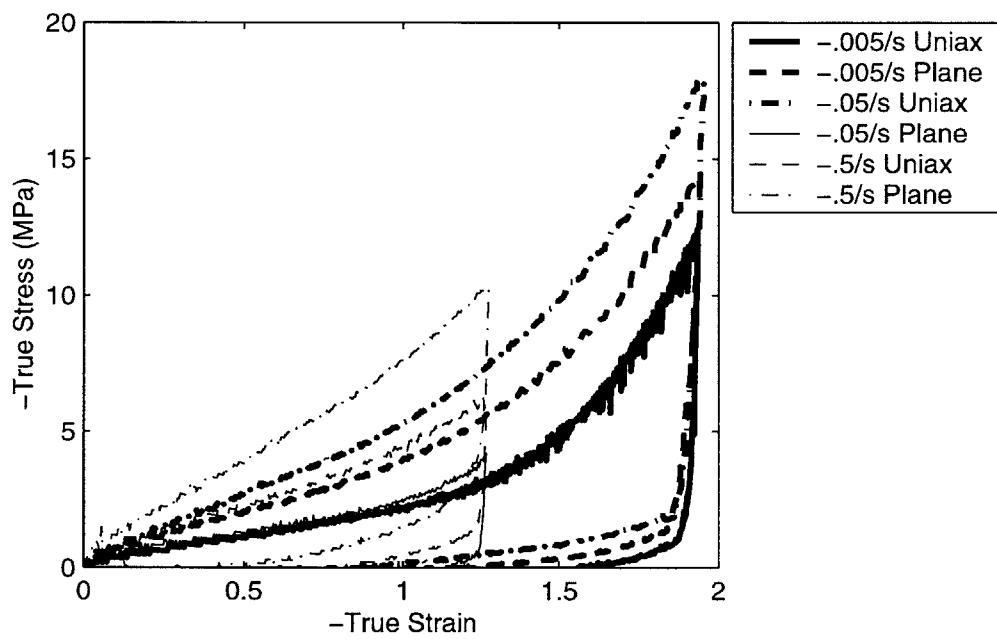
Figure 2-38: Uniaxial and Plane Strain Compression Data, Temperature = 100 ° C

Chapter 3

Constitutive Model

3.1 Background and Development

The constitutive modeling approach as well as many of the details correspond to that described by Boyce, Socrate, and Llana[12]. The full description will be included here for completeness.

The constitutive response of the polymer can be interpreted as follows: the polymer must overcome two sources of deformation resistance, an intermolecular resistance to flow and a resistance due to molecular orientation. This is shown in figure 3-1 with two separate networks providing the two distinct resistances. Network A relates to the intermolecular resistance. This gives the material its initial stiffness and results in a finite stress at which the polymer will flow, termed the flow stress. Network B causes the polymer to harden at large strains and allows for molecular relaxation at higher temperatures. The two resistances are modeled as being in parallel, so the deformation gradient in each network is equal to the total deformation gradient,

$$\mathbf{F}_A = \mathbf{F}_B = \mathbf{F} \tag{3.1}$$

These two network descriptions will be developed separately:
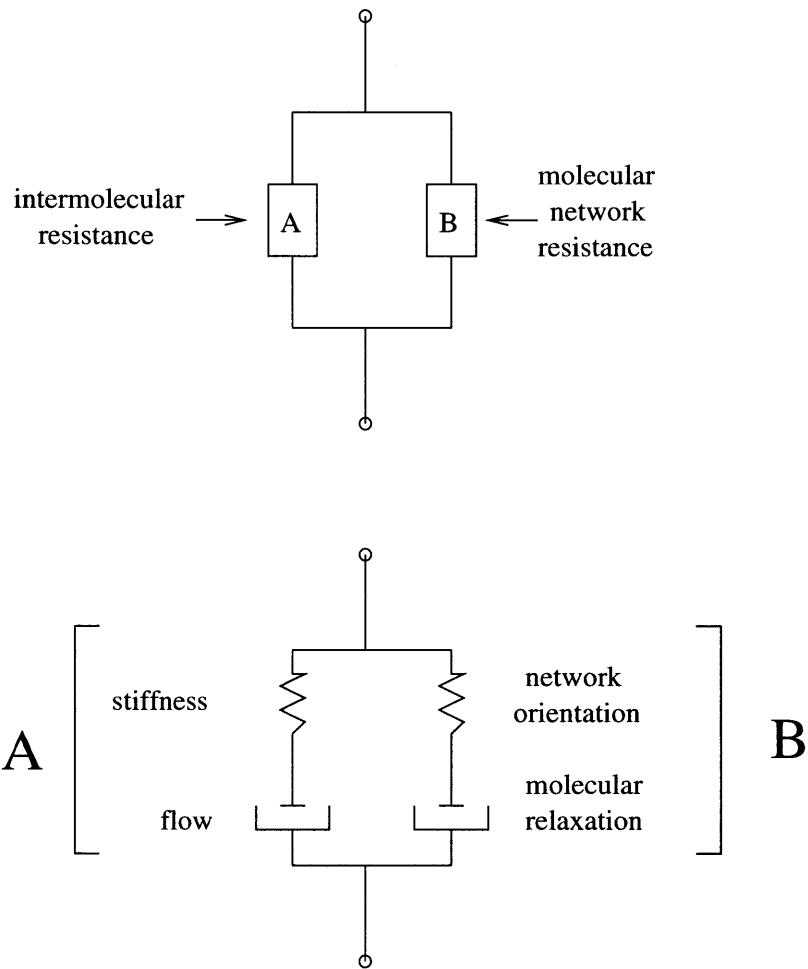
Figure 3-1: Schematic representation of the material resistances in the two networks

3.1.1 Network A

The deformation gradient of network A is decomposed into elastic and plastic components in a multiplicative manner

$$\mathbf{F}_A = \mathbf{F}_A^e \mathbf{F}_A^p \tag{3.2}$$

and is then decomposed into stretch and rotation components

$$\mathbf{F}_A^e = \mathbf{V}_A^e \mathbf{R}_A^e \tag{3.3}$$

$$\mathbf{F}_A^p = \mathbf{V}_A^p \mathbf{R}_A^p \tag{3.4}$$

The rate kinematics are described by the velocity gradient, $\mathbf{L}_A$

$$\mathbf{L}_A = \dot{\mathbf{F}}_A \mathbf{F}_A^{-1} \tag{3.5}$$

By substitution of the elastic and plastic contributions to the deformation gradient this becomes

$$\mathbf{L}_A = \dot{\mathbf{F}}_A^e \mathbf{F}_A^{e-1} + \mathbf{F}_A^e \dot{\mathbf{F}}_A^p \mathbf{F}_A^{p-1} \mathbf{F}_A^{e-1} = \mathbf{L}_A^e + \tilde{\mathbf{L}}_A^p \tag{3.6}$$

Note that $\tilde{\mathbf{L}}_A^p = \tilde{\mathbf{D}}_A^p + \tilde{\mathbf{W}}_A^p$. The representation is made unique by prescribing the spin to be zero: $\tilde{\mathbf{W}}_A^p = 0$.

The rate of stretching is constitutively described by

$$\tilde{\mathbf{D}}_A^p = \dot{\gamma}_A^p \mathbf{N}_A \tag{3.7}$$

Note that $\mathbf{N}_A$ is the normalized deviatoric stress in network A

$$\mathbf{N}_A = \frac{1}{\sqrt{2}\tau_A} \mathbf{T}_A' \tag{3.8}$$

$$\tau_A = \left[\frac{1}{2} \mathbf{T}_A' \mathbf{T}_A' \right]^{1/2} \tag{3.9}$$

47

$\mathbf{T}_A$ is related to the elastic deformation gradient by the constitutive relation

$$\mathbf{T}_A = \frac{1}{J_A}\mathcal{L}^e[\ln \mathbf{V}_A^e] \tag{3.10}$$

where $J_A = \det \mathbf{F}_A^e$ is the volume change, $\mathcal{L}^e$ is the fourth order tensor of elastic constants, and $\ln \mathbf{V}_A^e$ is the Hencky strain. The plastic strain rate, $\dot{\gamma}_A^p$, is assumed to follow a thermally activated process

$$\dot{\gamma}_A^p = \dot{\gamma}_{0A} \exp\left[-\frac{\Delta G(1 - \tau_A/s)}{k\theta}\right] \tag{3.11}$$

where $\dot{\gamma}_{0A}$ is the pre-exponential factor, ΔG is the activation energy which must be overcome for flow to begin, s is the shear resistance, taken to be $.15G$ (G is the shear modulus), k is Boltzmann's constant, and θ is the absolute temperature. The shear resistance can be further modified to account for pressure as in Boyce et al.[11]:

$$\tilde{s} = s(1 + \alpha p/s) \tag{3.12}$$

where the pressure $p = -\frac{1}{3}tr\mathbf{T}$ and α is the pressure coefficient.

Equations 3.1 to 3.12 complete the constitutive prescription for network A.

3.1.2 Network B

Two mechanisms are involved in the deformation of network B: first, the stretching and orientation of the polymer chain network and second, molecular relaxation. Network B can be thought of as a non-linear spring in series with a viscous element (see figure 3-1). As such, the deformation of this element can also be multiplicatively decomposed into a network and flow portion:

$$\mathbf{F}_B = \mathbf{F}_B^N \mathbf{F}_B^F \tag{3.13}$$

The velocity gradient is then

$$\mathbf{L}_B = \dot{\mathbf{F}}_B \mathbf{F}_B^{-1} \tag{3.14}$$

48

$$\mathbf{L}_B = \dot{\mathbf{F}}_B^N \mathbf{F}_B^{N-1} + \mathbf{F}_B^N \dot{\mathbf{F}}_B^F \mathbf{F}_B^{F-1} \mathbf{F}_B^{N-1} = \mathbf{L}_B^N + \tilde{\mathbf{L}}_B^F \qquad (3.15)$$

Again, $\tilde{\mathbf{L}}_B^F = \tilde{\mathbf{D}}_B^F + \tilde{\mathbf{W}}_B^F$ is made unique by setting the spin to zero, $\tilde{\mathbf{W}}_B^F = 0$.

The Arruda-Boyce eight-chain rubber elasticity model[4, 3] is used to prescribe the stress arising from the network orientation of the polymer. The stretch of each chain in the network is given by an effective chain stretch, or the root-mean square of the distortional applied stretch: $\bar{\lambda}_N = [\frac{1}{3}tr(\bar{\mathbf{B}}^N)]^{1/2}$, where $\bar{\mathbf{B}}^N = \bar{\mathbf{F}}_B^N \bar{\mathbf{F}}_B^{NT}$, $\bar{\mathbf{F}}_B^N = (J_B)^{-1/3}\mathbf{F}_B^N$, and $J_B = \det \mathbf{F}_B^N$. The relationship between the chain stretch and the network stress is then

$$\mathbf{T}_B = \frac{1}{J_B} \frac{nk\theta}{3} \frac{\sqrt{N}}{\bar{\lambda}_N} \mathcal{L}^{-1} \left[\frac{\bar{\lambda}_N}{\sqrt{N}} \right] [\bar{\mathbf{B}}^N - (\bar{\lambda}_N)^2 \mathbf{I}] \qquad (3.16)$$

The parameters in this expression are as follows: n is the chain density, N is the number of rigid links between entanglements, and $nk\theta$ is a rubbery modulus, which is proportional to the initial hardening modulus of the strain hardening curve, or the initial slope of the stress-strain curve at the onset of flow, before much hardening has occurred. $\mathcal{L}^{-1}$ is the inverse Langevin function given by $\mathcal{L}(\beta) = \coth(\beta) - (1/\beta)\mathcal{L}^{-1}[\bar{\lambda}_N/\sqrt{N}]$. This derives from a non-Gaussian probability function which accounts for the fact that the chains have a finite extensibility so as $\bar{\lambda}_N$ approaches $\sqrt{N}$, the stress rises dramatically.

The rate of molecular relaxation is given by

$$\tilde{\mathbf{D}}_B^F = \dot{\gamma}_B^F \mathbf{N}_B \qquad (3.17)$$

where $\mathbf{N}_B$ is

$$\mathbf{N}_B = \frac{1}{\sqrt{2}\tau_B} \mathbf{T}'_B \qquad (3.18)$$

$$\tau_B = \left[\frac{1}{2} \mathbf{T}'_B \mathbf{T}'_B \right]^{1/2} \qquad (3.19)$$

and $\mathbf{T}_B$ is prescribed using the Arruda-Boyce model. The only remaining unknown is the rate of relaxation, $\dot{\gamma}_B^F$. The assumed mechanism is chain reptation, the physical picture being one of polymer chains sliding through tube-like paths created by the

49

entangled chains around them. A model by Bergstrom and Boyce[9] based on the Doi and Edwards[19] theory of reptational motion is used to model this relaxation:

$$\dot{\gamma}_B^F = C\left(\frac{1}{\lambda_F - 1}\right)\tau_B \tag{3.20}$$

where $\lambda_F = [\frac{1}{3}tr(\mathbf{F}_B^F \mathbf{F}_B^{FT})]^{1/2}$ and the relaxation temperature dependence is captured by an exponential expression for C

$$C = D\exp\left\{-\frac{Q}{R\theta}\right\} \tag{3.21}$$

It will be shown that these relations for the molecular relaxation were not able to fully capture the strain rate dependence for PETG. The relation is therefore modified to better capture the observed strain rate dependence:

$$\dot{\gamma}_B^F = C\left[\left(\frac{1}{\lambda_F - 1}\right)\tau_B\right]^3 \tag{3.22}$$

Equations 3.1 and 3.13 through 3.22 describe the constitutive behavior of network B.

Now the total stress acting on the system is the sum of the stress in the two networks

$$\mathbf{T} = \mathbf{T}_A + \mathbf{T}_B \tag{3.23}$$

3.2 Determination of Material Constants

3.2.1 Network A

The initial elastic response of the material is governed by the elastic element in network A. The initial modulus is determined from the stress-strain curves for uniaxial compression, in combination with the time-temperature relationship obtained from the DMA experiments. The equations are cast in terms of the shear modulus and the bulk modulus. Using the uniaxial compression data at 25 $^\circ$ C and at 90 $^\circ$ C, the

Young's modulus is found to be 1.25 GPa and 75 MPa, respectively. Assuming that the Poisson's ratio is approximately .33 at room temperature and .49 above the glass transition temperature, the bulk modulus can be determined at each temperature using the relation

$$B = \frac{E}{3(1 - 2\nu)} \tag{3.24}$$

This gives a temperature independent value for the bulk modulus of 1.25 GPa. The temperature dependence of the shear modulus is approximated with a hyperbolic tangent function:

$$G = \alpha - \beta \tanh(\gamma(\theta - \theta_g)) + \phi(\theta - \theta_g) \tag{3.25}$$

where α is the modulus at the glass transition temperature[1] , β is one-half the modulus drop as the material goes through the glass transition region, γ is the slope, $-\frac{dG}{d\theta}$, in the glass transition region, and ϕ is proportional to the slope outside the transition region (see figure 3-2). The constants α, β, and γ are determined from the DMA data, which is scaled by a factor of 0.5 to correlate with the uniaxial compression experiments. The data is then converted into shear modulus data using the relation

$$G = \frac{3EB}{9B - E} \tag{3.26}$$

For example, at 25 ° C, the DMA data gives a value for Young's modulus of 2.5 GPa. This corresponds to an initial slope of 1.25 GPa in uniaxial compression, and from equation 3.26 the shear modulus is found to be .47 GPa at 25 ° C. A curve fit using the data points at $\dot{\epsilon} = -.1$ sec^{-1} yields:

$$\alpha = 0.235 \text{ GPa}$$

$$\beta = 0.2 \text{ GPa}$$

---

[1]The glass transition temperature is defined as the temperature at which the material softens from a glassy solid to a rubbery material. In the DMA data, this is indicated by the dramatic drop in modulus with temperature around 80 ° C. Since the drop does not occur instantaneously, but occurs gradually over about 5 ° C, the value of the glass transition temperature is taken as the temperature half way between where the low temperature plateau ends and the high temperature plateau begins in the DMA data.
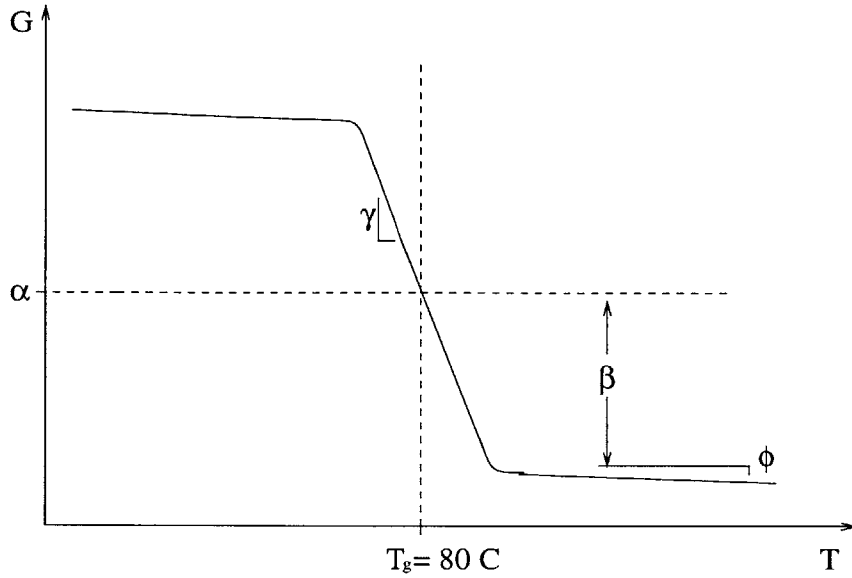
Figure 3-2: Description of initial modulus curve fit and parameters

$$\gamma = .2 \ \mathrm{K}^{-1}$$

The 90 ˚ C and 100 ˚ C data at $\dot{\epsilon} = -.005 \ \mathrm{sec}^{-1}$ provides the information needed to determine the slope outside the transition region, ϕ. This value is determined to be -.001 GPa K^{-1} for PETG.

The initial modulus in the transition region is also strain-rate dependent. This is accounted for using time-temperature superposition to shift the glass transition temperature with strain rate. The following expression provides a good fit for the relation between the glass transition temperature, θ_g, and the strain rate, $\dot{\gamma}_A$:

$$\theta_g - \theta_g^* = A \log_{10} \dot{\gamma}_A + B \tag{3.27}$$

The equivalent strain rate in network A, $\dot{\gamma}_A$, is approximated as $\sqrt{3}\dot{\epsilon}$, with $\dot{\epsilon}$ being the machine strain rate. θ_g^* is taken to be the reference transition temperature, or 80 ˚ C at $\dot{\epsilon} = -.1 \ \mathrm{sec}^{-1}$.

Figures 3-3 and 3-4 show how the DMA data compares with the data from the uniaxial compression experiments. In figure 3-3 the DMA data is plotted along with

Figure 3-3: DMA Data combined and reduced data points for discrete strain rates

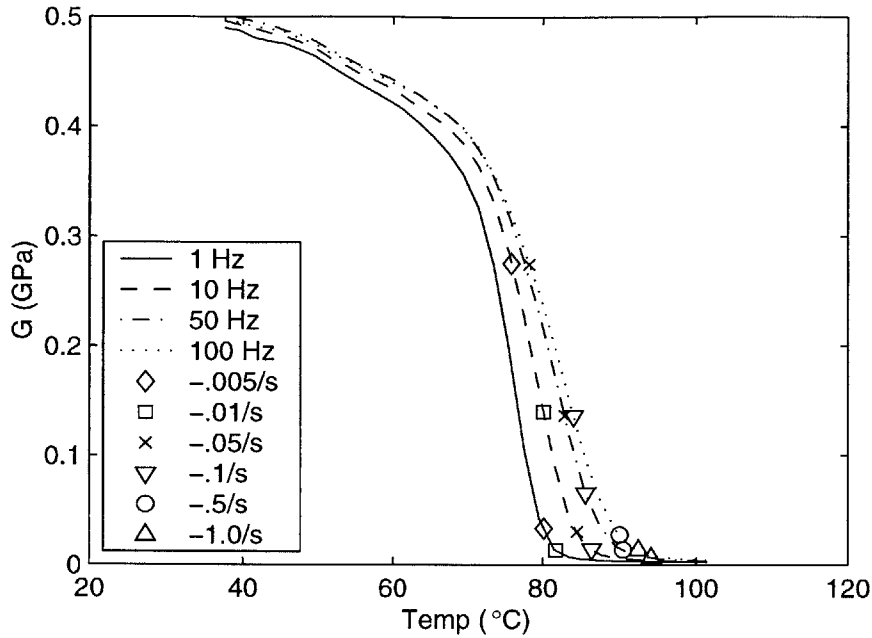points for each strain rate as determined from the DMA test setup, where the cyclic load is converted into an equivalent strain rate. Figure 3-4 includes the data points from the uniaxial compression data. These indicate good agreement between the DMA and uniaxial test results. Figure 3-5 shows the curve fit at $\dot{\epsilon} = -.1 \ \mathrm{sec}^{-1}$, again indicating quite good agreement, and figure 3-6 shows the time-temperature superposition effect on the curve plotted with the data points from the uniaxial compression data. Again, very good correlation is seen.

Next, the rate dependence of the flow stress is incorporated using the equation for the thermally activated process:

$$\dot{\gamma}_A^p = \dot{\gamma}_{0A} \exp\left[-\frac{\Delta G(1 - \tau_A/s)}{k\theta}\right] \tag{3.28}$$

The intermolecular resistance, s, is temperature dependent, and is modeled as $s(\theta) = 0.15G_A(\theta)$, where G_A is the initial shear modulus as determined above.

The constants $\dot{\gamma}_{0A}$ and ΔG are determined from the intial flow stress at each strain rate for a particular temperature. In this case, the 90 ° C data was used. Equation 3.28
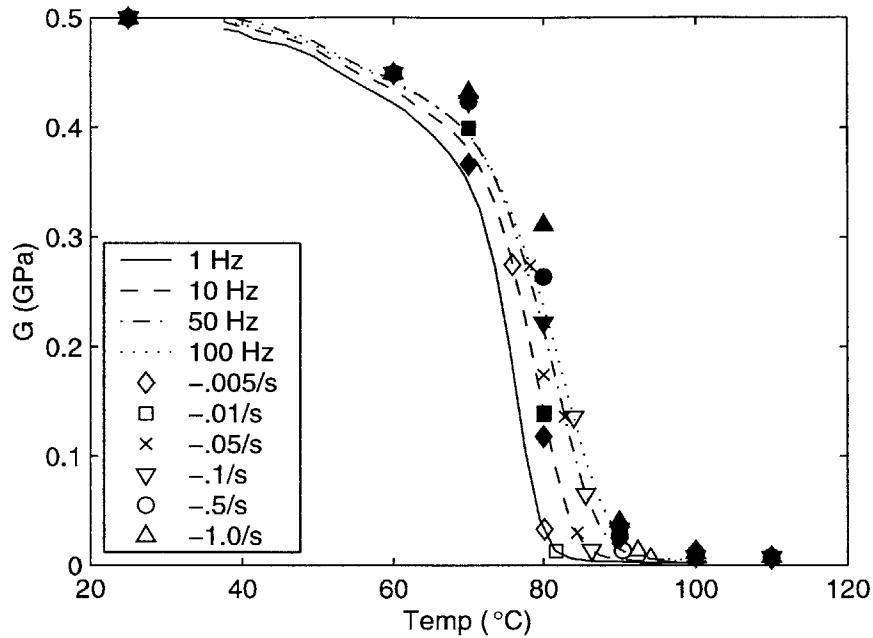
53

Figure 3-4: DMA Data combined with uniaxial initial modulus data (open symbols are DMA data at the indicated strain rates; filled symbols are the compression test data

is rearranged to a linear form

$$A \ln \left(\dot{\gamma}_A^p \right) - B = \left(\frac{1}{k\theta} \left(\frac{\tau}{s} - 1 \right) \right) \tag{3.29}$$

where A=1/ΔG and B=Aln$\dot{\gamma}_{0A}$. A least squares fit of the data gives the values for A and B, and in turn for ΔG and $\dot{\gamma}_{0A}$. For PETG, the values are:

$$\Delta G = 1.70 \times 10^{-19} \, \text{J}$$

$$\dot{\gamma}_{0A} = 2.0 \times 10^{12} \, \text{sec}^{-1}$$

Figure 3-7 shows a plot of the flow stress, τ, as a function of the logarithm of the shear strain rate, $\ln \dot{\gamma}$, along with the least squares curve fit of the data. This figure demonstrates that very good agreement is obtained using the thermally activated mechanism. It is interesting to note that the curve fit is not a straight line. This is due to the rate dependence of the intermolecular resistance, s, which comes in through
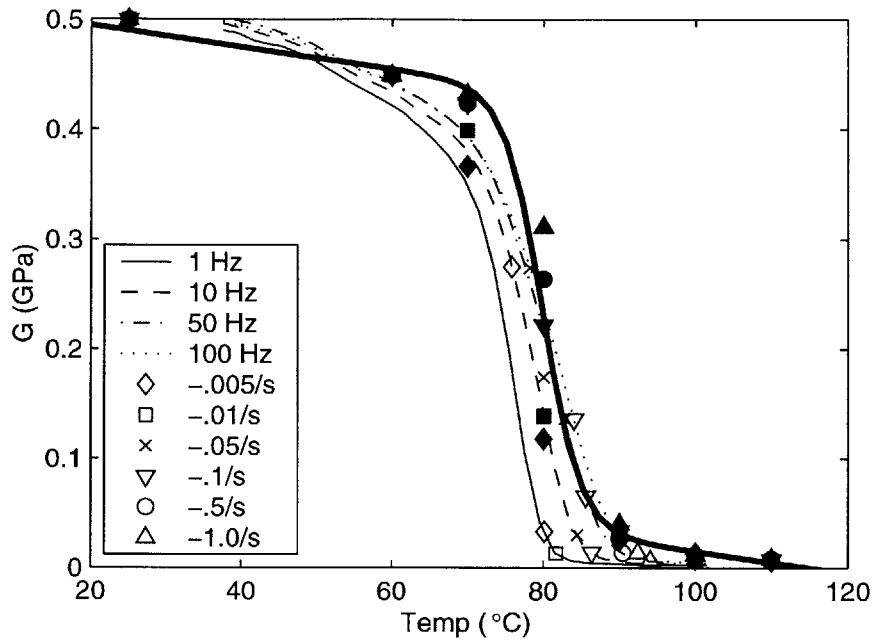
Figure 3-5: DMA Data combined with uniaxial initial modulus data and curve fit (open symbols are DMA data at the indicated strain rates; filled symbols are the compression test data)
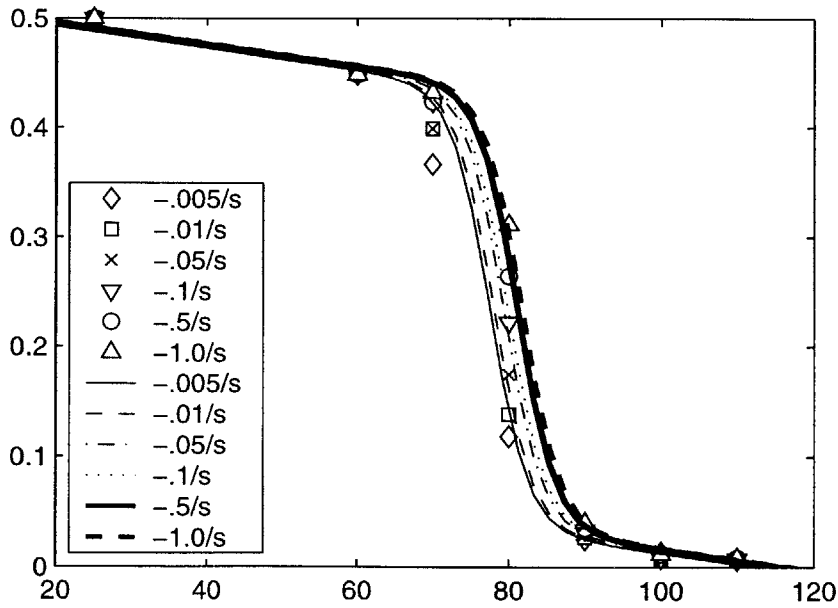
Figure 3-6: Uniaxial initial modulus data and curve fit at various strain rates
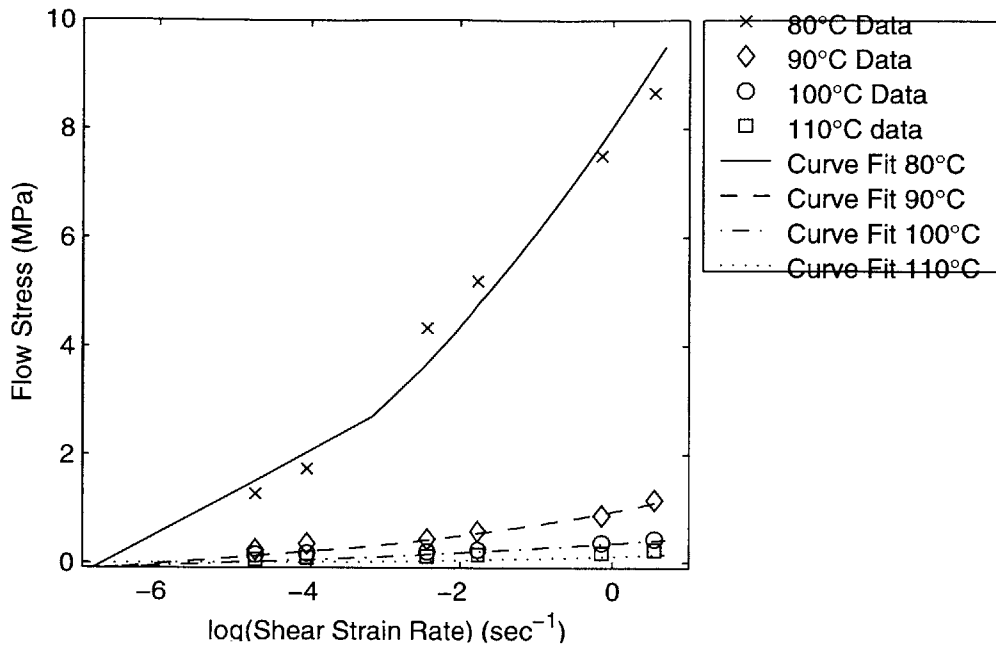
Figure 3-7: Flow stress as a function of strain rate

the rate dependence of the glass transition temperature and the shear modulus, as was discussed previously. The result is a non-linear curve for the flow stress as a function of the logarithm of the strain rate. The 80 ° C data shows particularly good correlation.

3.2.2 Network B

The material properties needed for the hardening/stiffening portion of network B are an initial hardening slope, $nk\theta$, and the number of rigid links between entanglements, N, which correlates with the effective stretch where the dramatic upturn in slope occurs. Fitting to the 25 ° C uniaxial compression data at $\dot{\epsilon} = -0.1$ sec^{-1} gives:

$$nk\theta = 9 \times 10^6 \text{ Pa}$$

$$N = 6$$

Figure 3-8: Uniaxial Compression Data, Temperature $= 25\,^\circ$C, $\dot{\epsilon} = -1.0/s$, plotted with the strain hardening curve

Figures 3-8 and 3-9 show how well the strain hardening is captured at 25 $^\circ$ C in uniaxial compression. The agreeme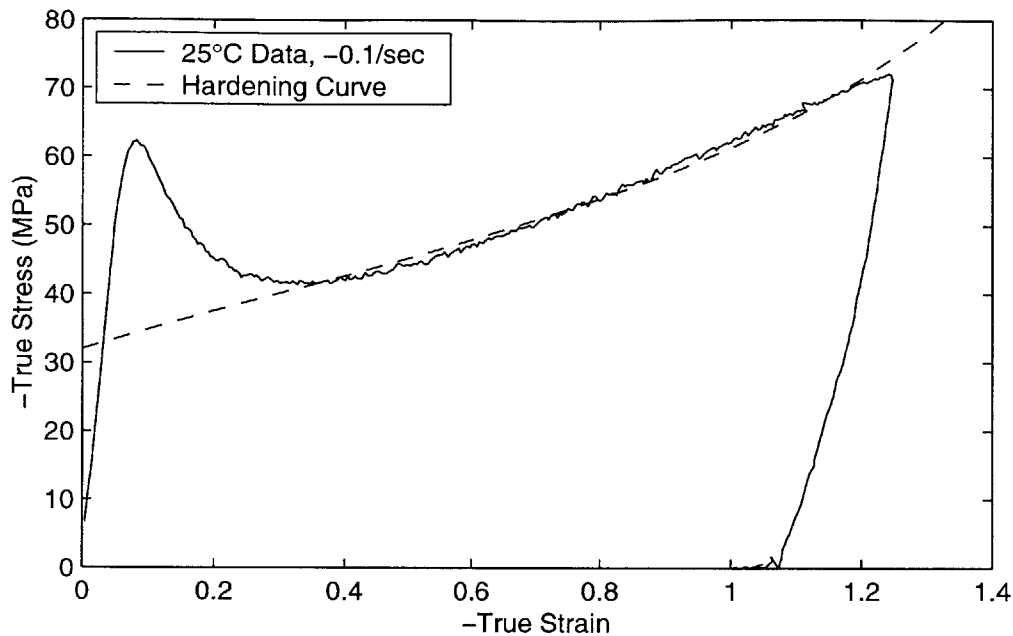nt is not nearly as good in plane strain compression. The discrepancy, in part, is due to the initial compliance that appears in the plane strain data as well as the subsequent thermal softening which acts to lower the overall hardening slope[5]. It is possible that better agreement could be achieved in both deformation modes using slightly different values for $nk\theta$ and N, but due to the excellent agreement with the uniaxial compression data, these values have been used for the subsequent computer simulations. It will be shown that this strain hardening overprediction in plane strain will consistently influence the ability of the model to predict deformation in plane strain at higher temperatures. Future work will address finding a better fit for the plane strain compression data. Work will also be done to incorporate a correction for the plane strain test fixture compliance. This should greatly decrease the discrepancy in predicting the hardening behavior in plane strain compression.

The molecular relaxation in network B is temperature dependent and was origi-
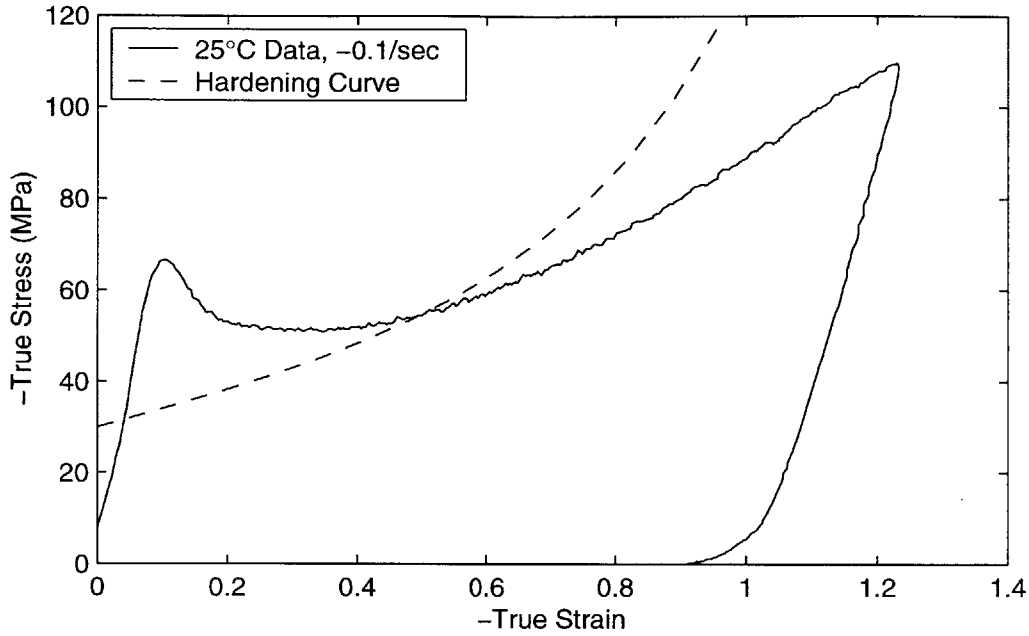
Figure 3-9: Plane Strain Compression Data, Temperature $= 25\,^{\circ}$C, $\dot{\epsilon} = -1.0/s$, plotted with the strain hardening curve

nally modeled as

$$\dot{\gamma}_B^F = C \left(\frac{1}{\lambda_F - 1}\right) \tau_B \tag{3.30}$$

with C being a temperature dependent parameter:

$$C = D \exp\left\{-\frac{Q}{R\theta}\right\} \tag{3.31}$$

Figure 3-10 shows the result of fitting the molecular relaxation coefficient, C, to the $90\,^{\circ}$ C data at a strain rate of -.5 sec^{-1}. This expression is inadequate in predicting the strain rate dependence of the material behavior at $90\,^{\circ}$ C, as is evident from the extreme over-relaxation at the lower strain rates of -.05 sec^{-1} and -.005 sec^{-1}.

To better capture the strain rate dependence, equation 3.30 is modified to be:

$$\dot{\gamma}_B^F = C \left[\left(\frac{1}{\lambda_F - 1}\right) \tau_B\right]^3 \tag{3.32}$$

Through trial and error curve fitting at $90\,^{\circ}$ C, $100\,^{\circ}$ C, and $110\,^{\circ}$ C of the -0.5 sec^{-1}
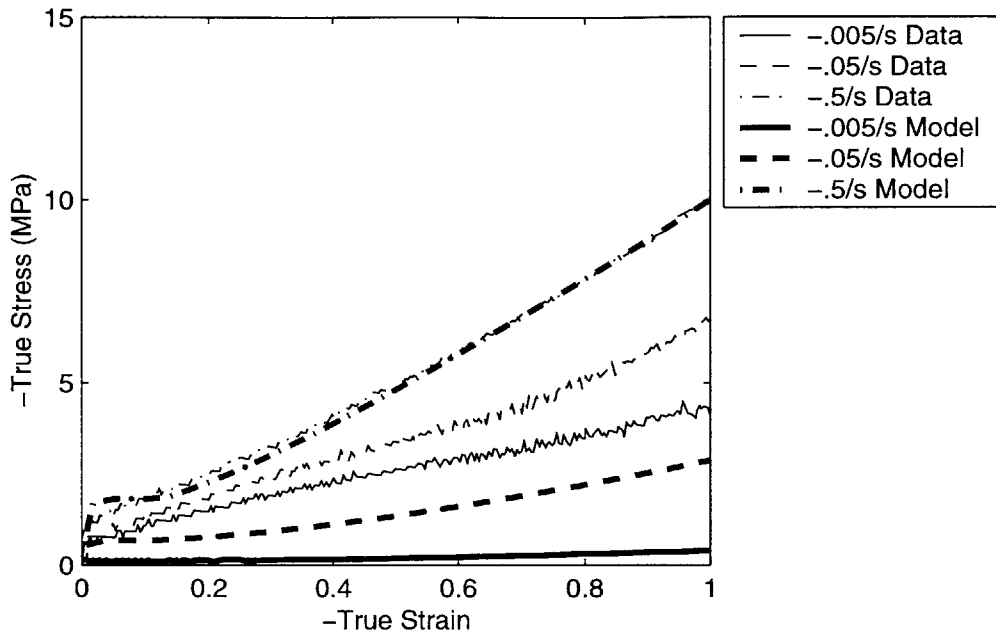
Figure 3-10: Uniaxial Compression, Temperature = 90 ° C, Comparison of model prediction with experimental data

data the value of C at each temperature can be determined:

$$C(90 \degree C, -.5s^{-1}) = 1.0 \times 10^{-23}(\text{Pa s})^{-1}$$

$$C(100 \degree C, -.5s^{-1}) = 25.0 \times 10^{-23}(\text{Pa s})^{-1}$$

$$C(110 \degree C, -.5s^{-1}) = 140.0 \times 10^{-23}(\text{Pa s})^{-1}$$

and using a least-squares curve fit of these values, D and Q/R are obtained:

$$D = 1.74 \times 10^{18}(\text{Pa s})^{-1}$$

$$Q/R = 3.444 \times 10^{4}\text{K}$$

This fully specifies the material properties needed for this model.

59

3.3 Comparison with Experimental Data

The following figures show the results of the computer simulation for uniaxial compression and plane strain compression. Figures 3-11 to 3-14 show the results of the uniaxial compression simulations at each temperature from 80 °C to 110 °C. Figures 3-15 to 3-20 show the same results, plotted at constant strain rate. Figures 3-21 and 3-23 show the results at constant temperature for plane strain simulations.

The figures indicate that the material model captures the general trends of the stress-strain behavior of PETG quite well, including the initial modulus, roll over to flow, initial hardening slope, and strain hardening. The model is very good at predicting the temperature dependence of these various elements as well as the strain rate dependence. Figures 3-24 and 3-25 show enlarged views of the model predictions. Figure 3-24 shows the simulation at 90 °C at different strain rates and indicates that as strain rate increases, the model correctly predicts that the initial modulus, flow stress, and hardening modulus all increase. Figure 3-25 shows the simulation at -.05 sec^{-1} at different temperatures. It demonstrates that the model correctly captures the decrease in initial modulus, flow stress, and initial hardening modulus with increasing temperature. The model also captures some elements of the recovery of the material upon unloading, but in general it tends to underpredict what is observed in experiments. This will be found to be due to underpredicting the orientation hardening, which in turn drives recovery.

Figures 3-26 through 3-29 show the comparison between the computer simulations and the experimental data for uniaxial compression. Figures 3-30 and 3-32 show the same comparison for plane strain. The model does a fairly good job of predicting the deformation behavior up to a strain of about -1.0. The initial modulus and flow stress are predicted especially well at 80 °C, as shown in figures 3-26 and 3-30. At higher strain levels, the model is not quite as effective at predicting the material behavior. In plane strain, the model tends to overpredict the strain hardening at large strains, as is expected from the initial fit of the hardening parameters. In uniaxial compression, on the other hand, it appears that the model is predicting too much relaxation. For

60

example, at 90 ° C (see figure 3-27), the model simply does not predict the dramatic strain hardening that is observed in experiments. The trend is less pronounced at higher temperatures and high strain rates, but is still visible in the lower strain rates at 100 ° C and 110 ° C.

Since the material deformation is accommodated by a combination of strain due to the deforming network and strain due to molecular relaxation, the stress-strain curves can be decomposed into network stretch and flow stretch charts. This is approached as follows. Using the network orientation curve as a baseline for the material response in the absence of molecular relaxation, the strain hardening portion of each stress-strain curve is multiplicatively decomposed into network and flow portions. For example, at a total logarithmic strain of -1.0 (an axial stretch, λ_T, of .368), the data gives the stress level required to attain this strain. The baseline network orientation curve, however, indicates that this value of stress would have been reached at a much lower strain level, such as -0.7 (an axial stretch, λ_N, of .496) if network orientation were the only mechanism contributing to the polymer deformation. The remainder of the deformation is accounted for by molecular relaxation. The product of the network stretch and the flow stretch is therefore equal to the total stretch: $\lambda_N \lambda_F = \lambda_T$. In this example the flow stretch, λ_F, equals .741. This produces one point on the network stretch-flow stretch chart.

To illustrate, figure 3-33 shows the axial network stretch versus axial flow stretch curves for the 90 ° C experimental data. As deformation begins, the material has a network stretch and flow stretch equal to 1.0. As deformation progresses, it is accommodated by a combination of molecular relaxation and network orientation, and the relative amount that each contributes determines the slope of the curve. For the lower strain rates, the initial slope of the network stretch-flow stretch curve is steeper than at higher rates, indicating that more of the deformation is accommodated by molecular relaxation at low strain rates. This creates the general trend from the lower right to the upper left corner as strain rate increases. After the polymer reaches a certain level of network stretch (at approximately $\lambda_N = 0.6$ for -0.1 $\sec^{-1}$ in the 90 ° C data), the molecular relaxation ceases, indicated by the leveling off of the network

61

stretch-flow stretch curve. This leveling off occurs at earlier network stretch levels for lower strain rates.

Figures 3-34 through 3-36 show the network stretch versus flow stretch for uniaxial compression both for the experimental data and for the computer model at various temperatures. The plots help to explain why the model does not capture the dramatic increase in strain hardening at large strains in uniaxial compression. In comparing the experimental data with the computer simulations, it can be seen that the current model (indicated by filled symbols) initially follows the same trend as the experimental data (indicated by open symbols), but is unable to capture the cessation of flow. In their work with PET, Llana and Boyce[25] observed this phenomenon with PET and attributed it to the onset of strain-induced crystallization. While PETG is non-crystallizable, it seems to exhibit the same trend. In the next section, the model will be revised to incorporate this temperature and strain rate dependent cessation of flow to improve the ability of the model to capture the orientation hardening behavior of the material. This will also improve the ability of the model to predict the recovery upon unloading, as this recovery is directly related to the amount of strain which is accommodated by orientation hardening as opposed to molecular relaxation.

Figures 3-37 through 3-38 show the network stretch versus flow stretch for plane strain compression experiments and simulations. As was noted earlier, these plots consistently show how the model tends to overpredict the strain hardening in plane strain. Each of the simulated curves (filled symbols) lies above its corresponding experimental curve (open symbols), indicating that the simulation is predicting less molecular relaxation than is observed experimentally. It is also interesting to note that the plane strain curves do not exhibit such a distinct flow cutoff as was observed in the uniaxial compression experiments. This is likely because experiments were only carried out to a final strain of -1.3 due to the limited size of the plane strain compression fixture. It is suggested that if the experiments were carried out to higher strain levels, the same flow cessation would appear in the plane strain data as appears in the uniaxial data. This warrants additional testing in future work.
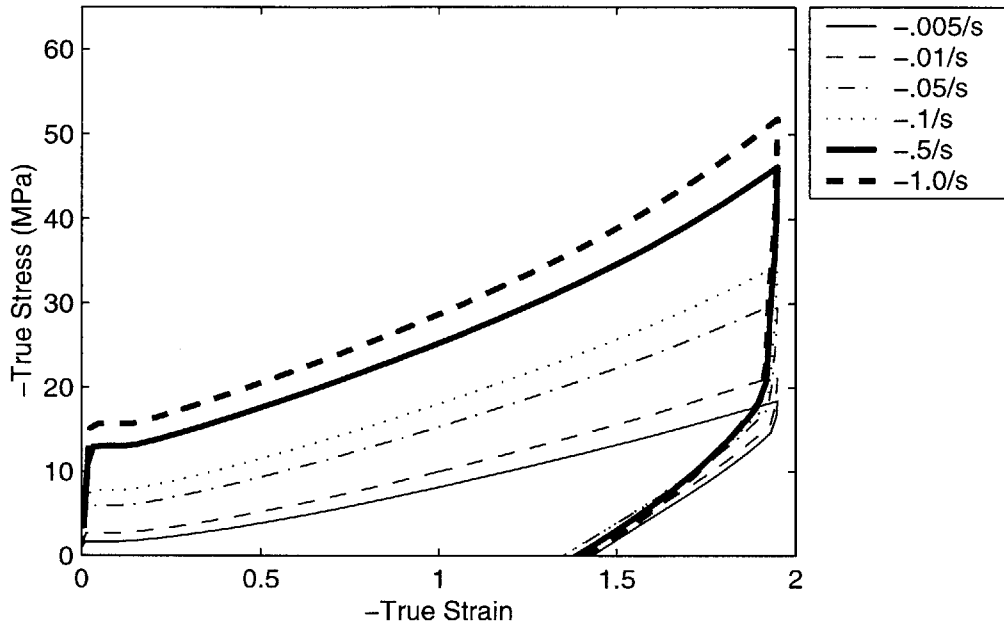
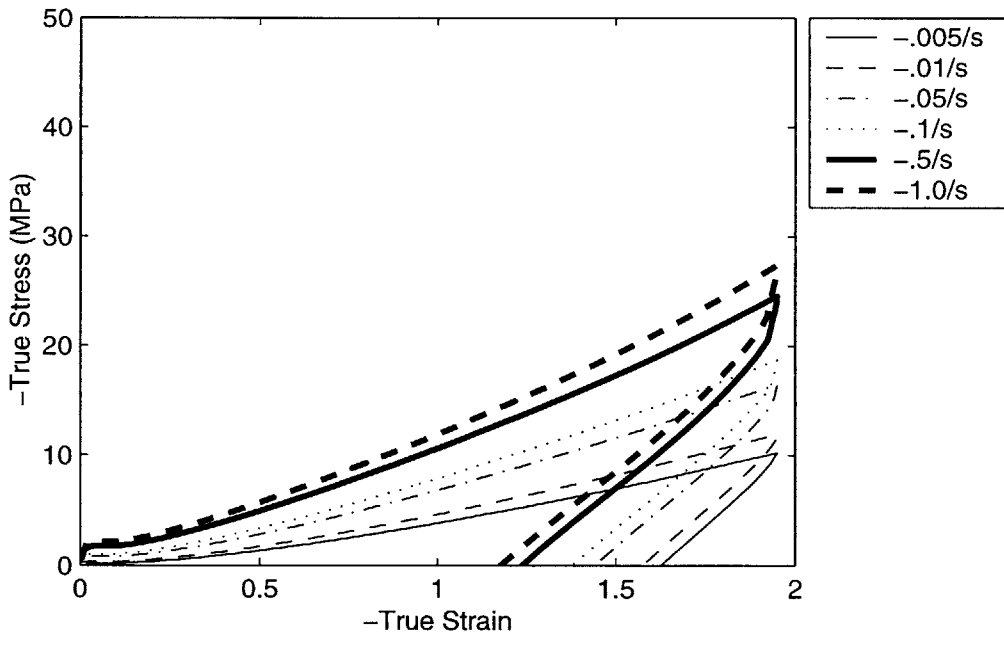Figure 3-11: Uniaxial Compression Simulation, Temperature = 80 ° C

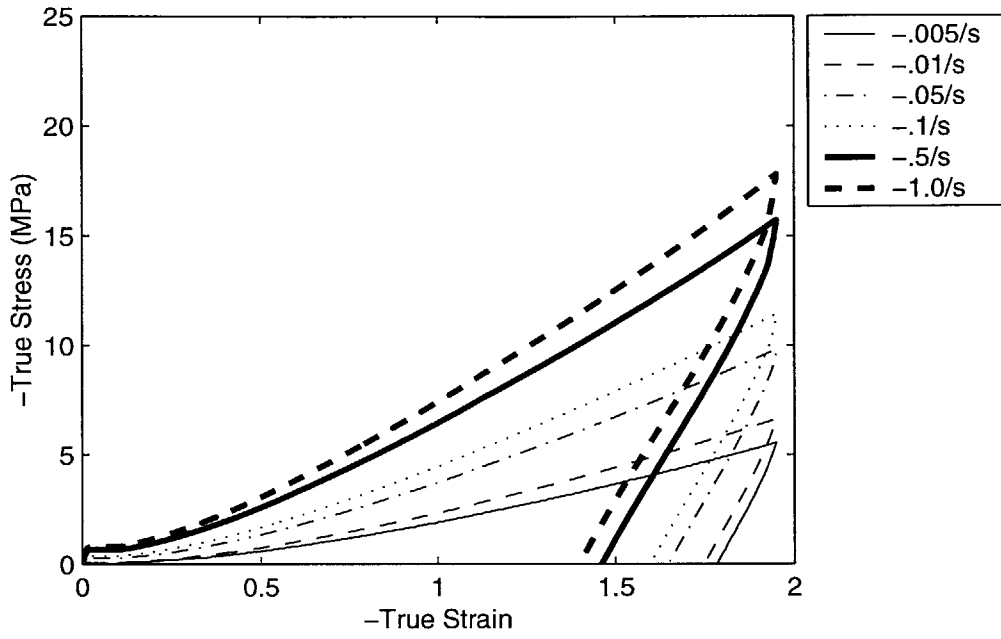Figure 3-12: Uniaxial Compression Simulation, Temperature = 90 ° C

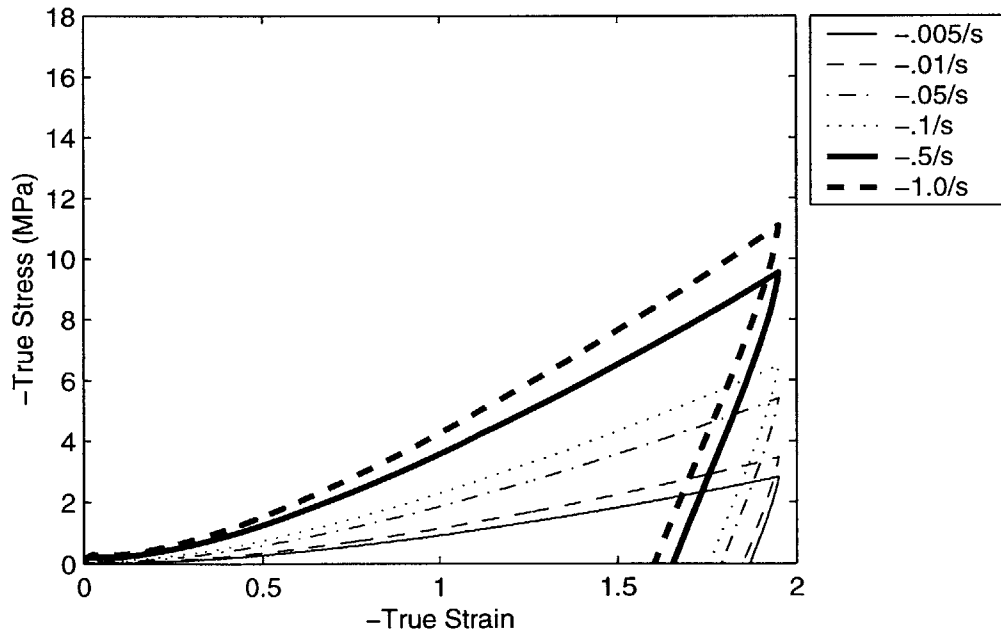Figure 3-13: Uniaxial Compression Simulation, Temperature = 100 ° C

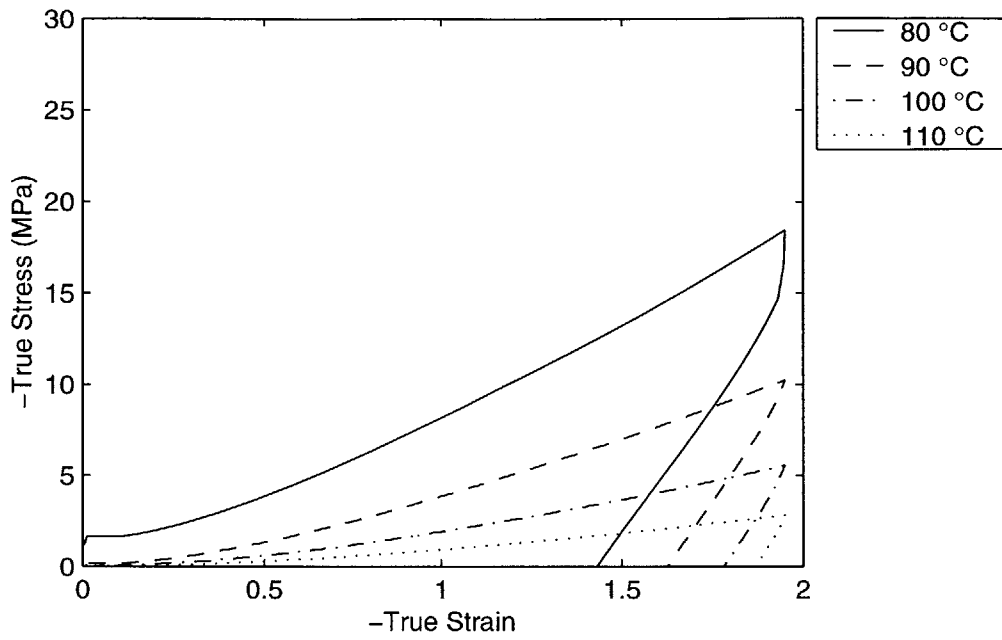Figure 3-14: Uniaxial Compression Simulation, Temperature = 110 ° C

64

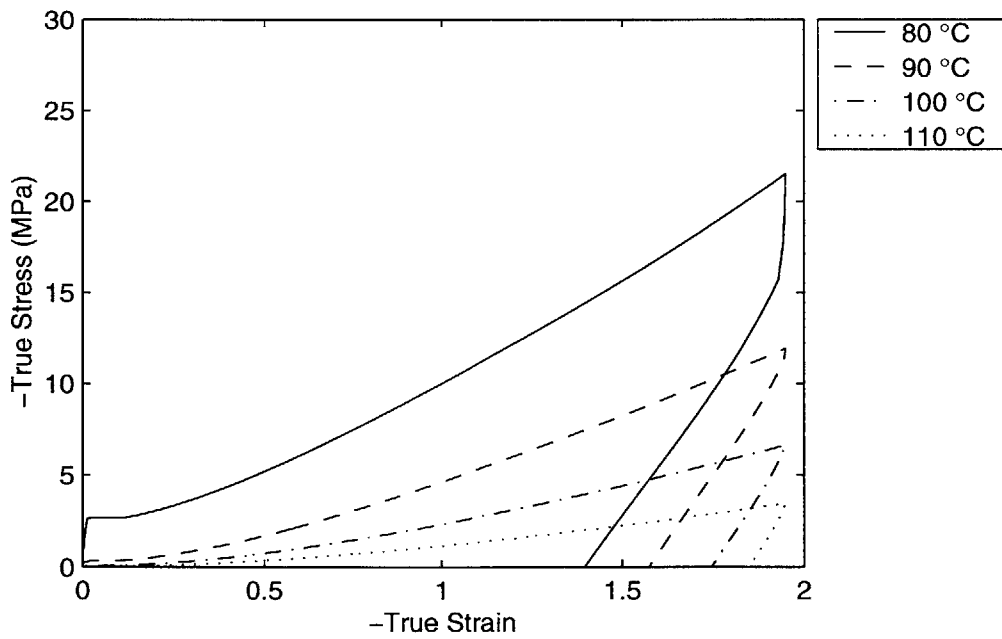Figure 3-15: Uniaxial Compression Simulation, $\dot{\varepsilon} = -.005/s$

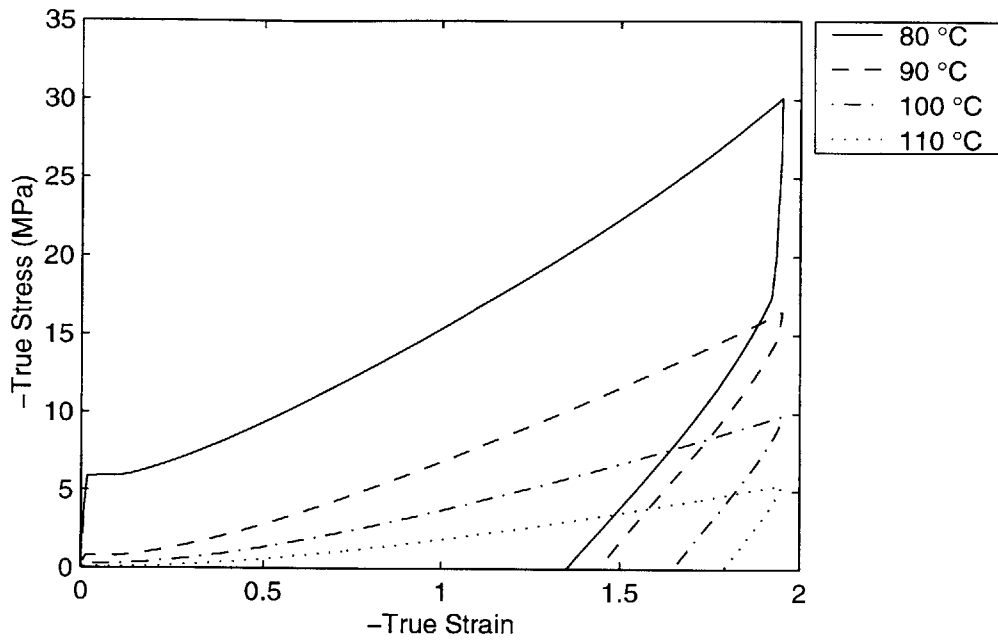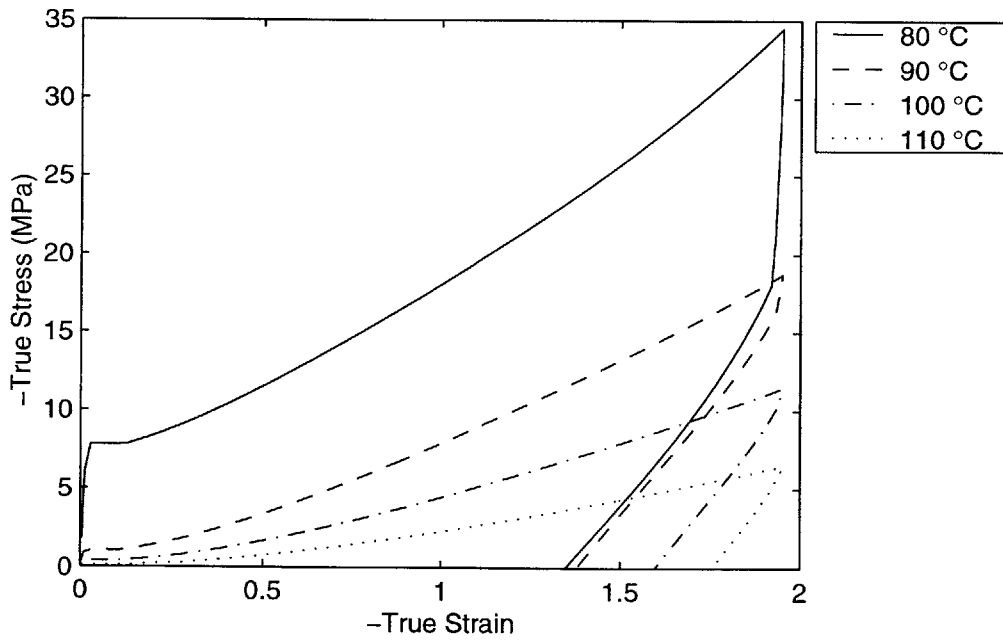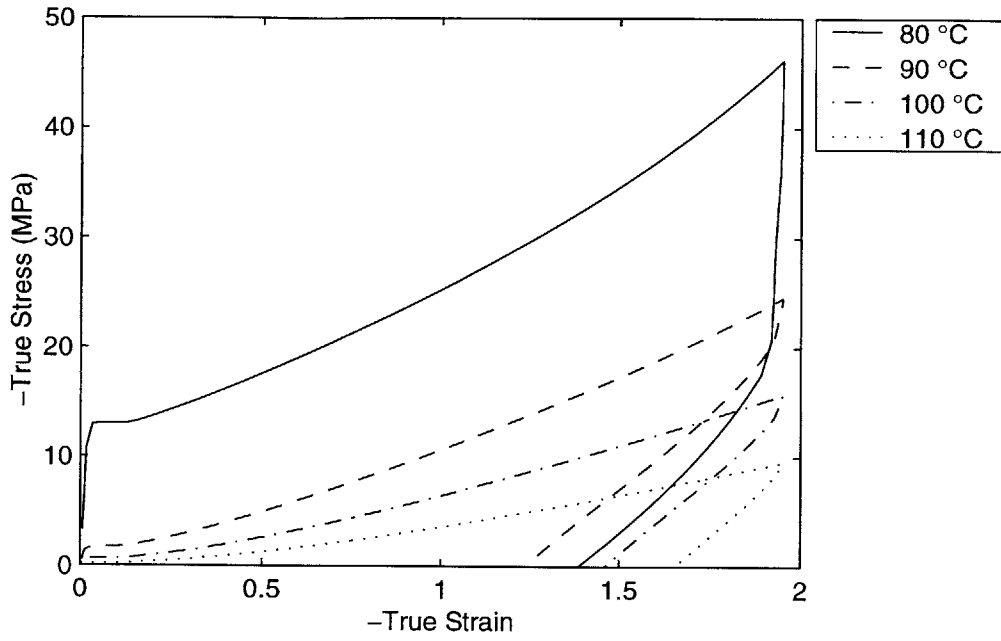Figure 3-16: Uniaxial Compression Simulation, $\dot{\varepsilon} = -.01/s$

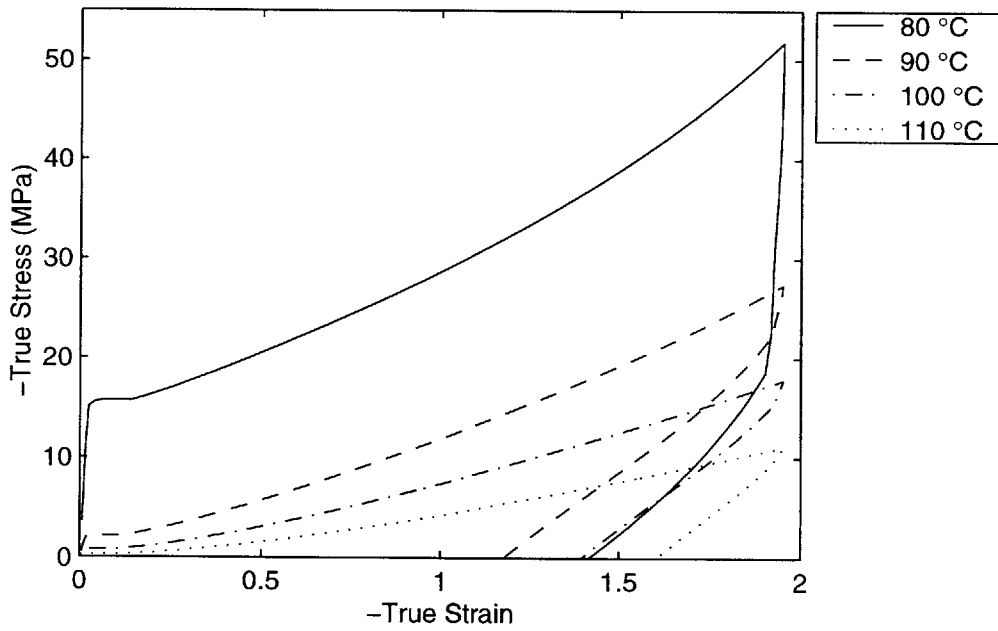Figure 3-17: Uniaxial Compression Simulation, $\dot{\varepsilon} = -.05/\mathrm{s}$

Figure 3-18: Uniaxial Compression Simulation, $\dot{\varepsilon} = -.1/\mathrm{s}$

Figure 3-19: Uniaxial Compression Simulation, $\dot{\varepsilon} = -.5/\text{s}$

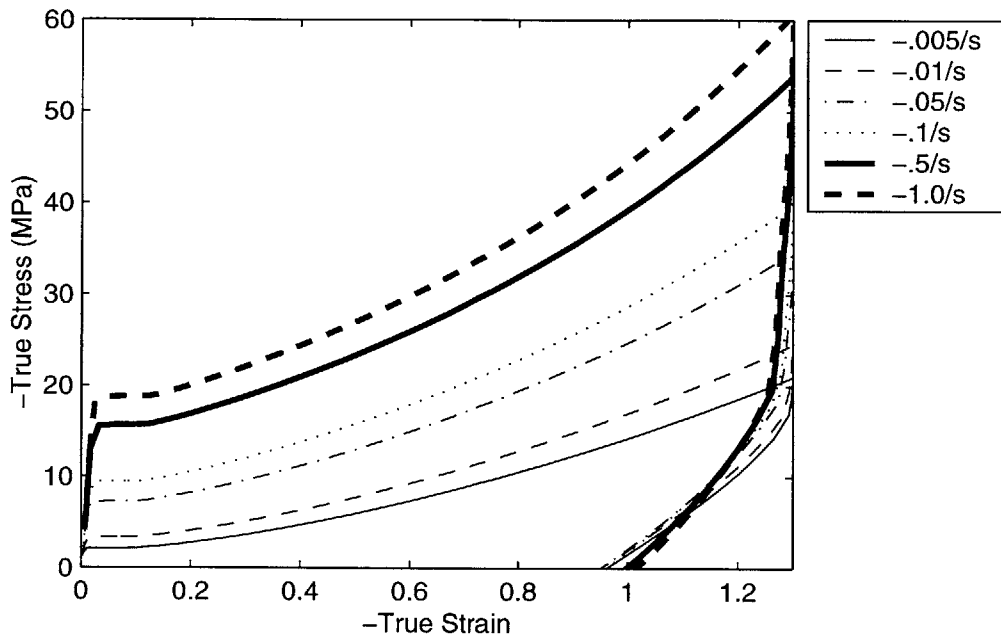Figure 3-20: Uniaxial Compression Simulation, $\dot{\varepsilon} = -1.0/\text{s}$

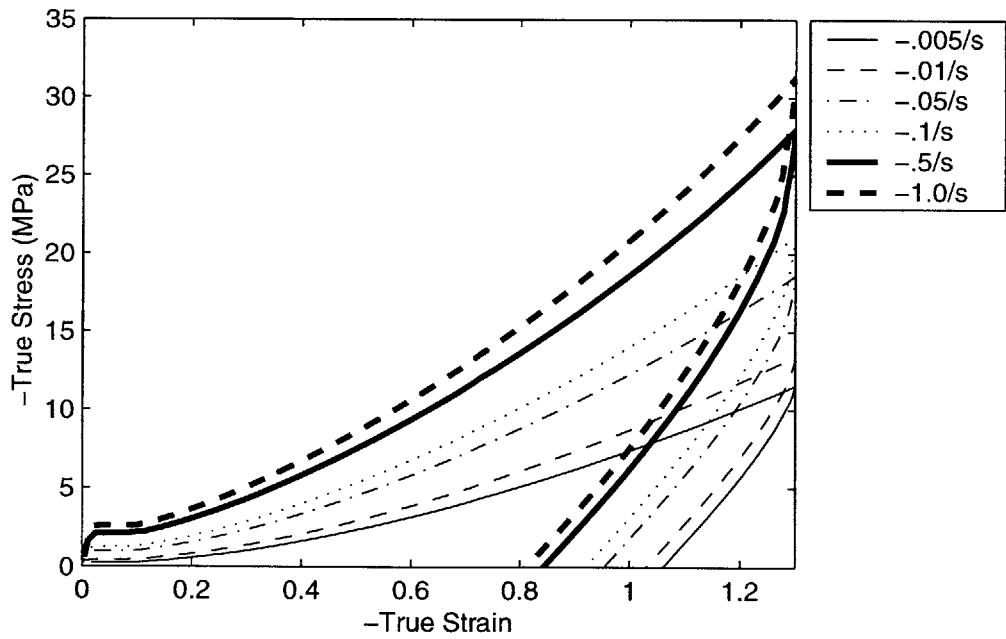Figure 3-21: Plane Strain Compression Simulation, Temperature = 80 ° C

Figure 3-22: Plane Strain Compression Simulation, Temperature = 90 ° C
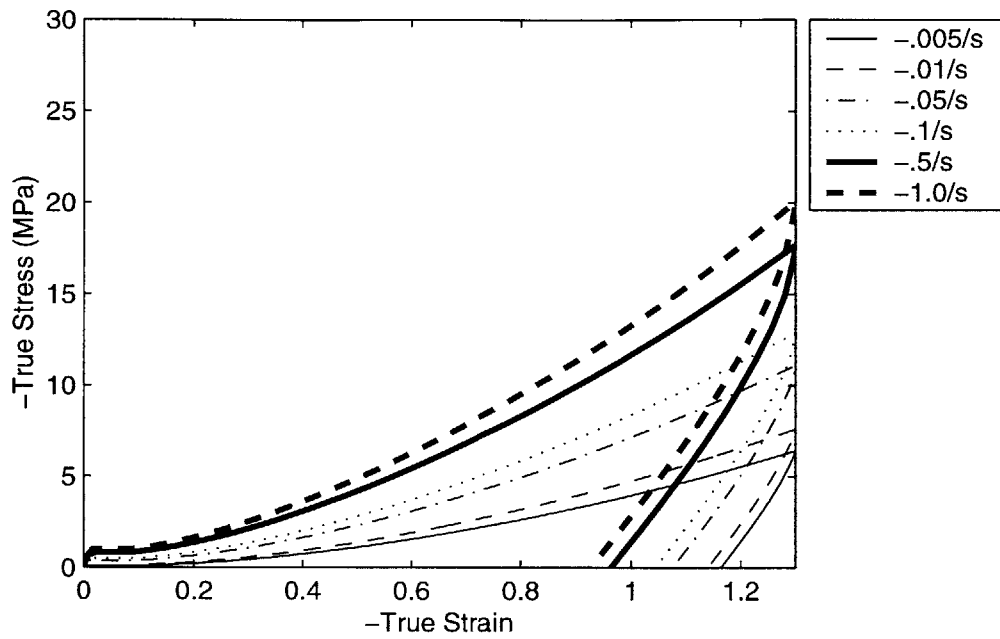
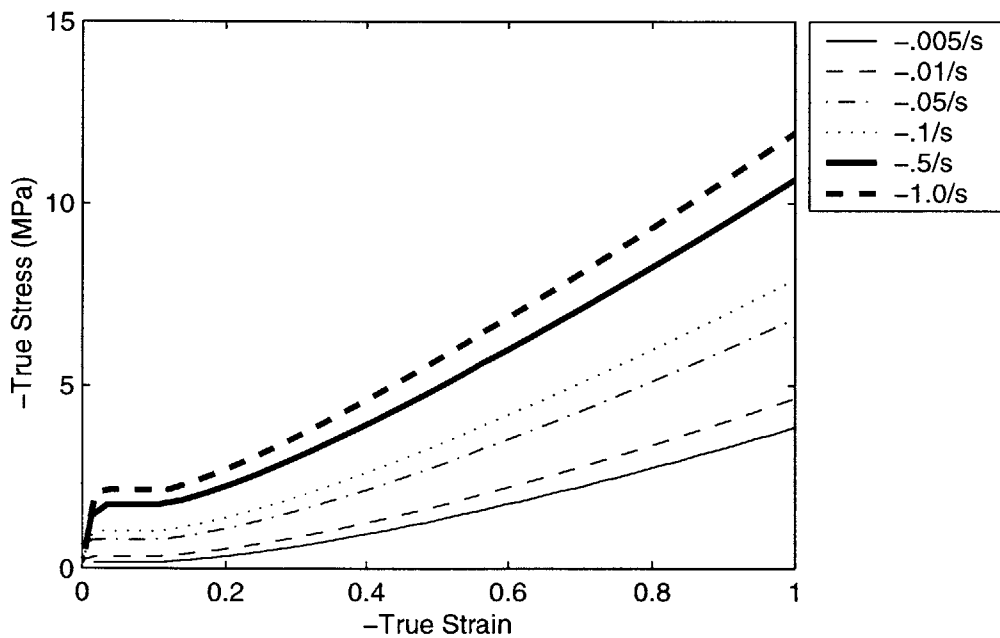Figure 3-23: Plane Strain Compression Simulation, Temperature = 100 ° C

Figure 3-24: Uniaxial Compression Simulation, Temperature = 90 ° C, Enlarged to show detail of initial modulus and flow stress
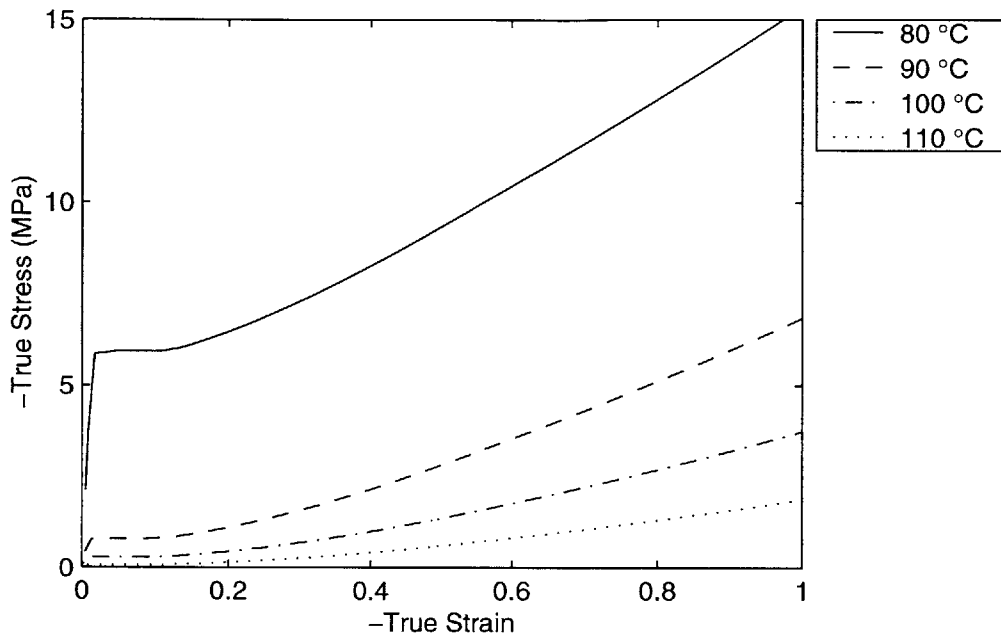
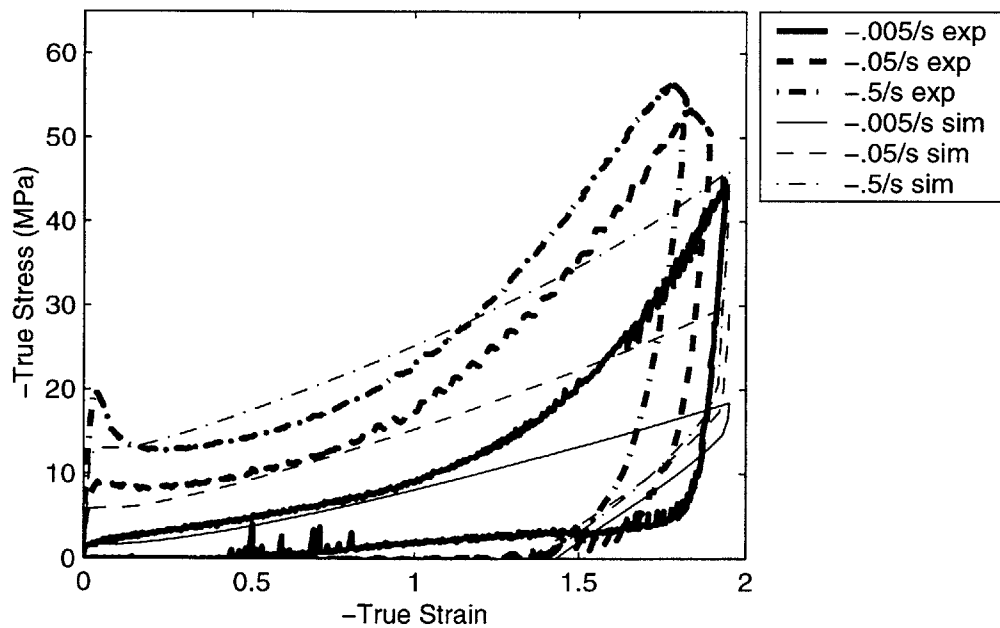Figure 3-25: Uniaxial Compression Simulation, $\dot{\varepsilon} = -.05/\text{s}$

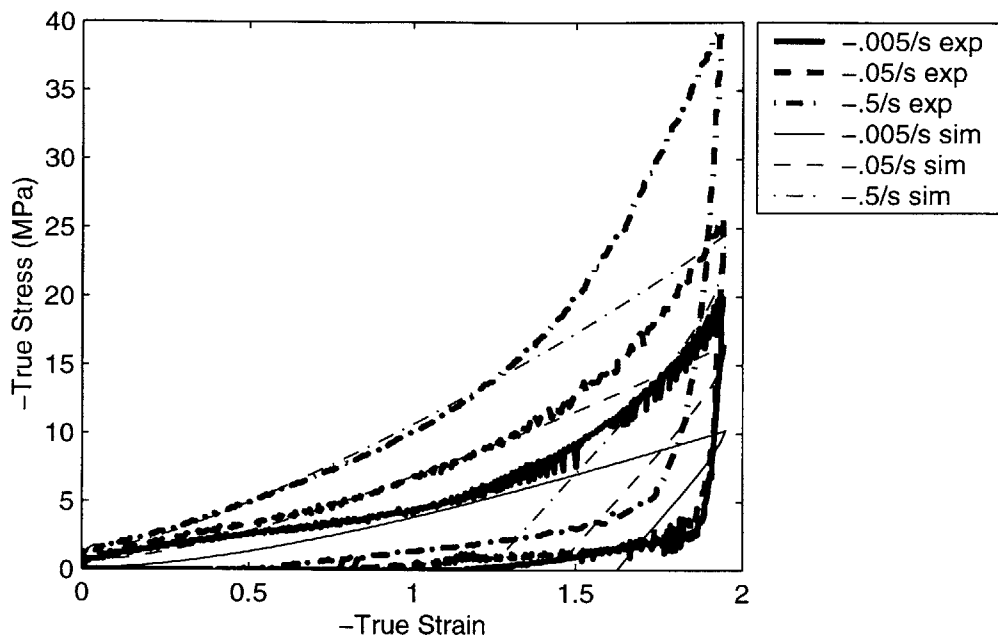Figure 3-26: Uniaxial Compression, Comparing Simulation with Experimental Data, Temperature = 80 °C

Figure 3-27: Uniaxial Compression, Comparing Simulation with Experimental Data, Temperature = 90 °C
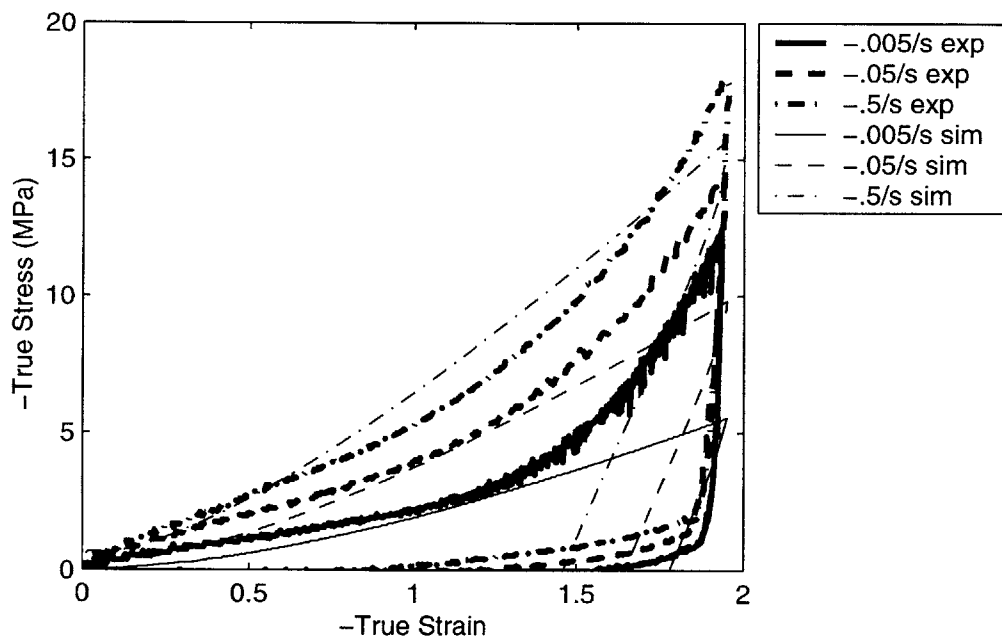

Figure 3-28: Uniaxial Compression, Comparing Simulation with Experimental Data, Temperature = 100 °C

71

Figure 3-29: Uniaxial Compression, Comparing Simulation with Experimental Data, Temperature = 110 ° C

Figure 3-30: Plane Strain Compression, Comparing Simulation with Experimental Data, Temperature = 80 ° C

Figure 3-31: Plane Strain Compression, Comparing Simulation with Experimental Data, Temperature = 90 ° C
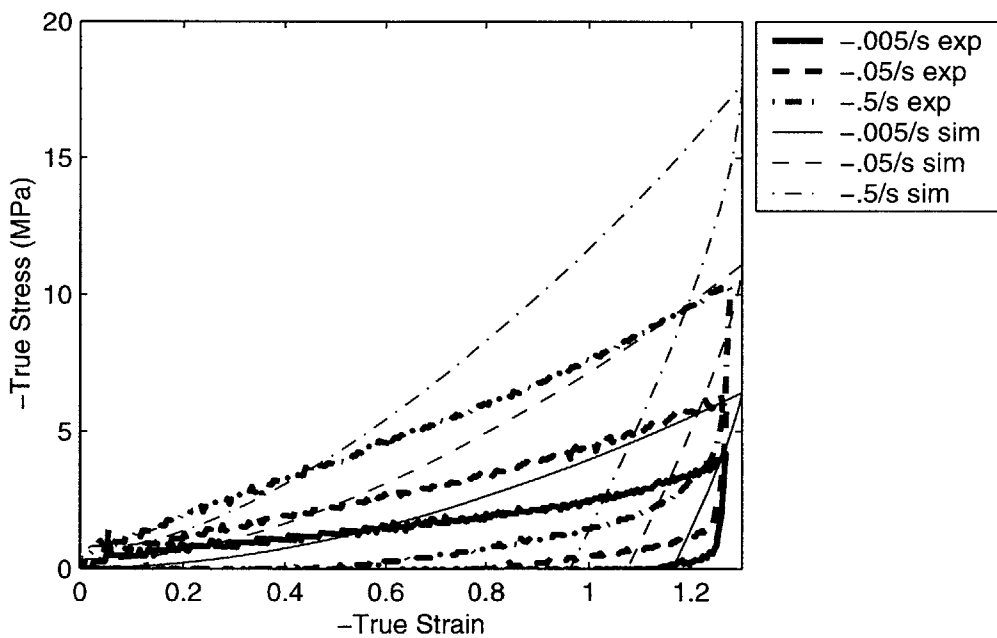
Figure 3-32: Plane Strain Compression, Comparing Simulation with Experimental Data, Temperature = 100 ° C
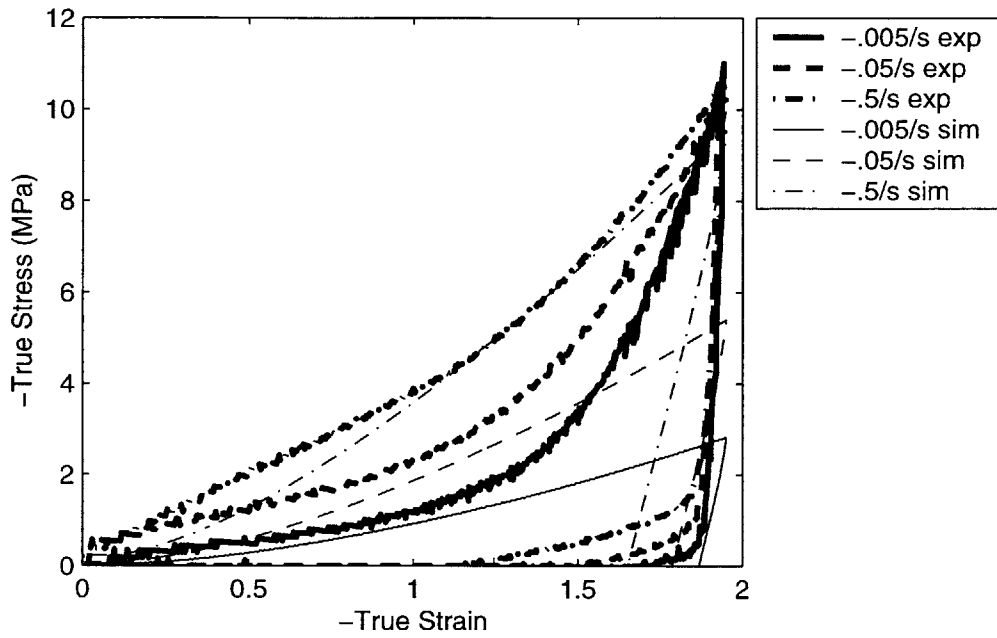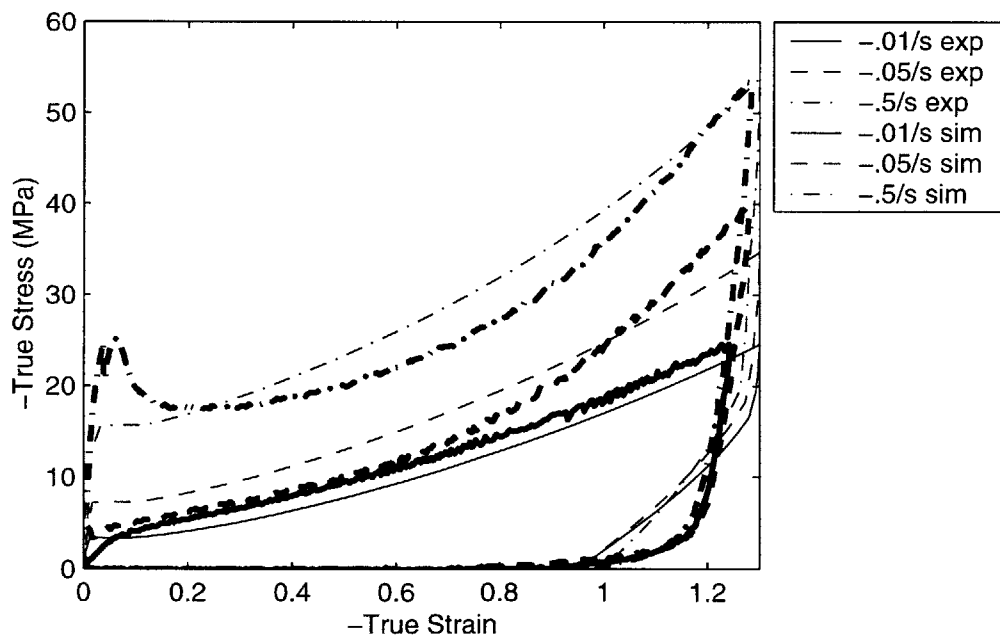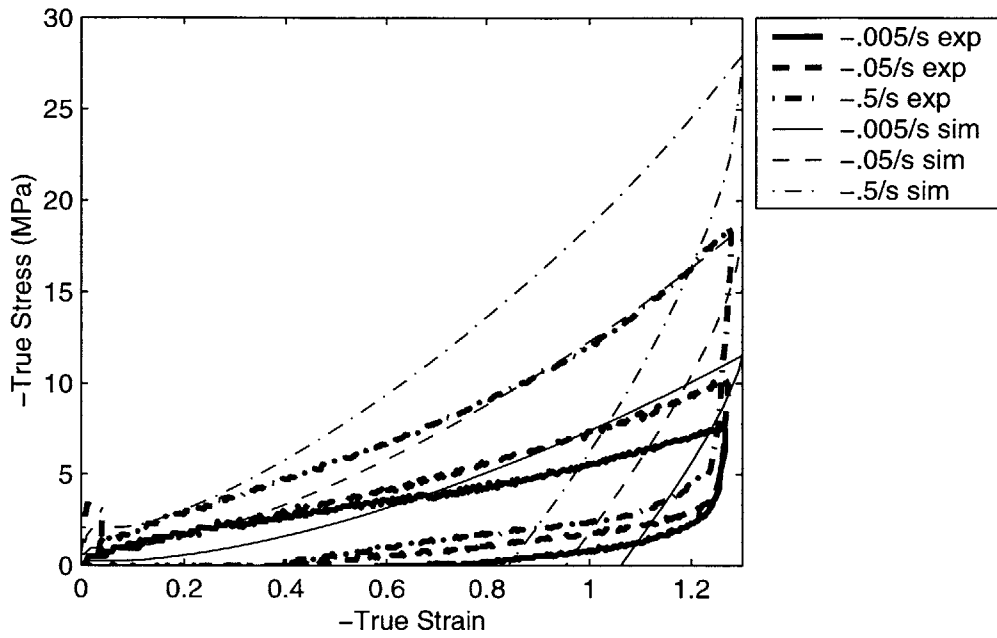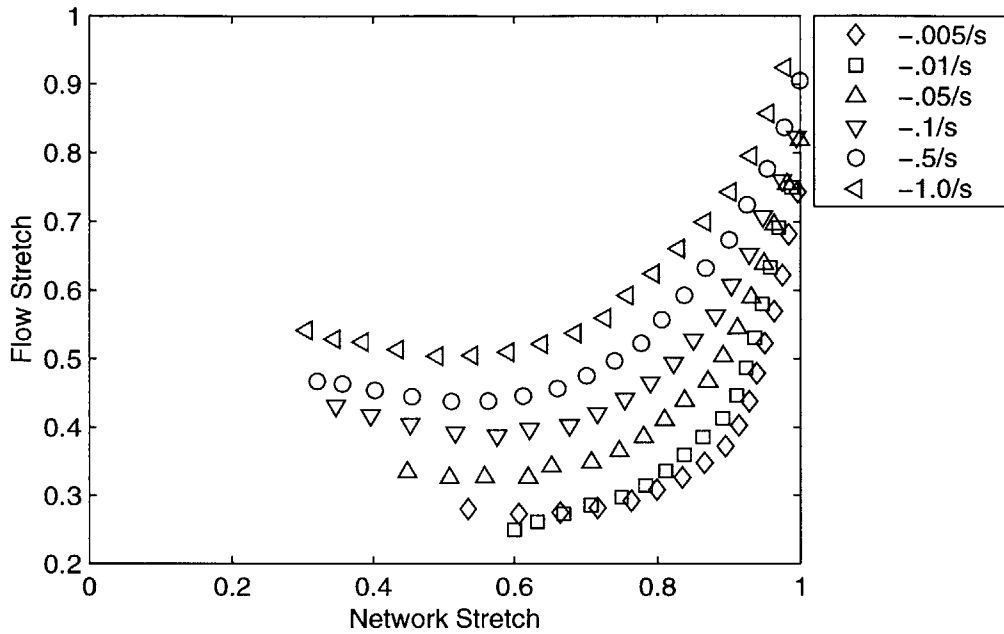
Figure 3-33: Network Stretch versus Flow Stretch, Uniaxial Compression, T = 90 ° C, Experimental data alone
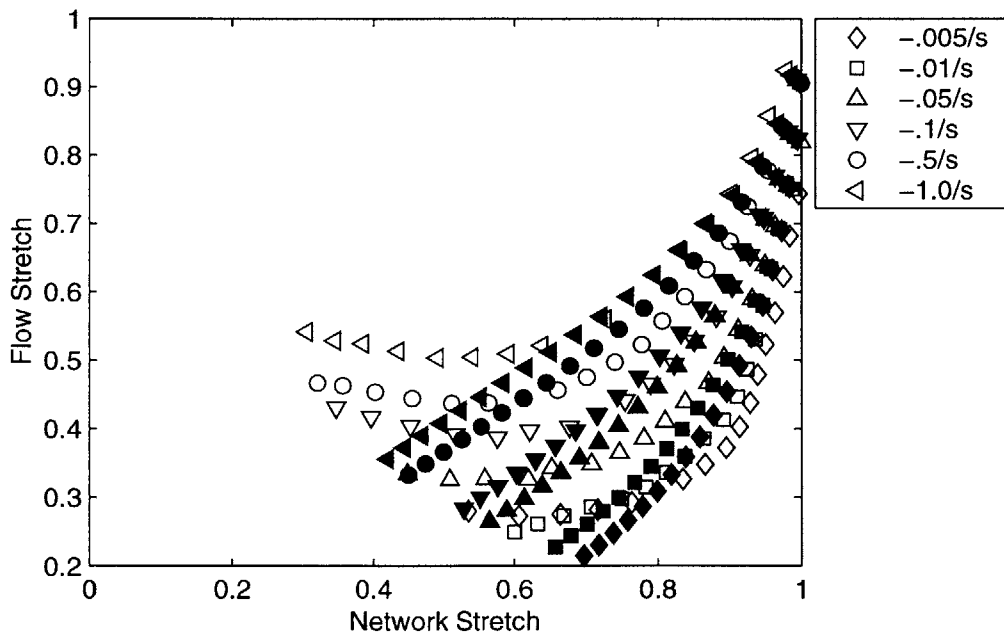
Figure 3-34: Network Stretch versus Flow Stretch, Uniaxial Compression, T = 90 ° C (open symbols are experimental data; filled symbols are computer simulations)
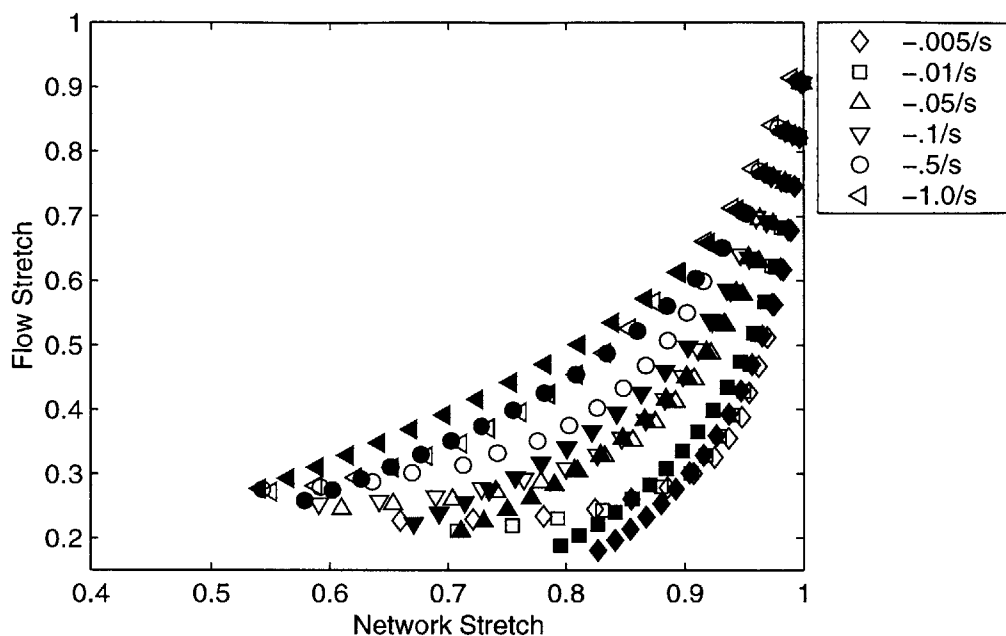
Figure 3-35: Network Stretch versus Flow Stretch, Uniaxial Compression, T = 100 ° C (open symbols are experimental data; filled symbols are computer simulations)

Figure 3-36: Network Stretch versus Flow Stretch, Uniaxial Compression, T = 110 ° C (open symbols are experimental data; filled symbols are computer simulations)

Figure 3-37: Network Stretch versus Flow Stretch, Plane Strain Compression, T = 90 ° C (open symbols are experimental data; filled symbols are computer simulations)

Figure 3-38: Network Stretch versus Flow Stretch, Plane Strain Compression, T = 100 ° C (open symbols are experimental data; filled symbols are computer simulations)

3.4   Revised Molecular Relaxation Model
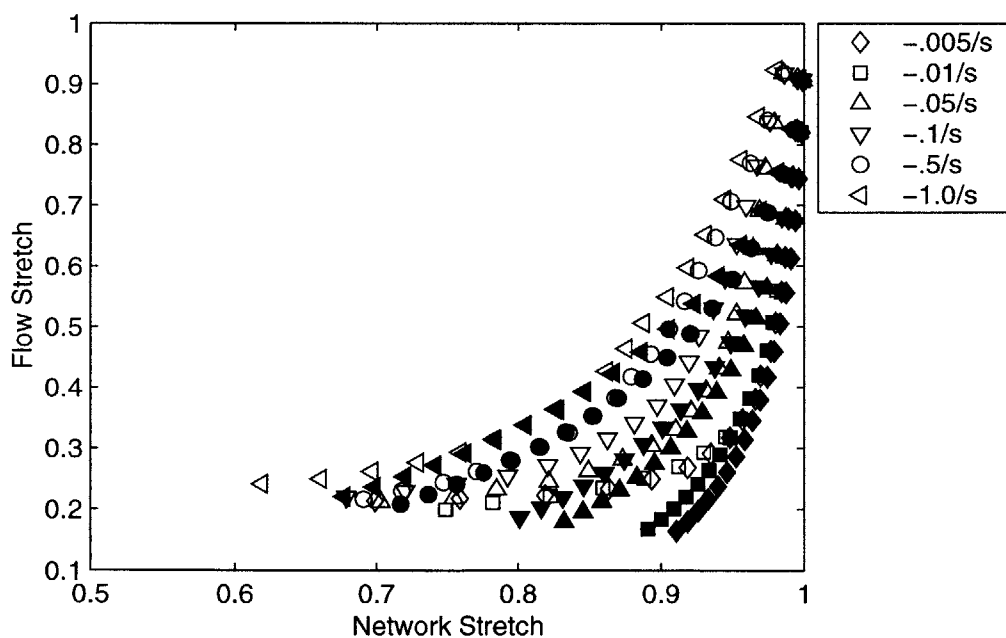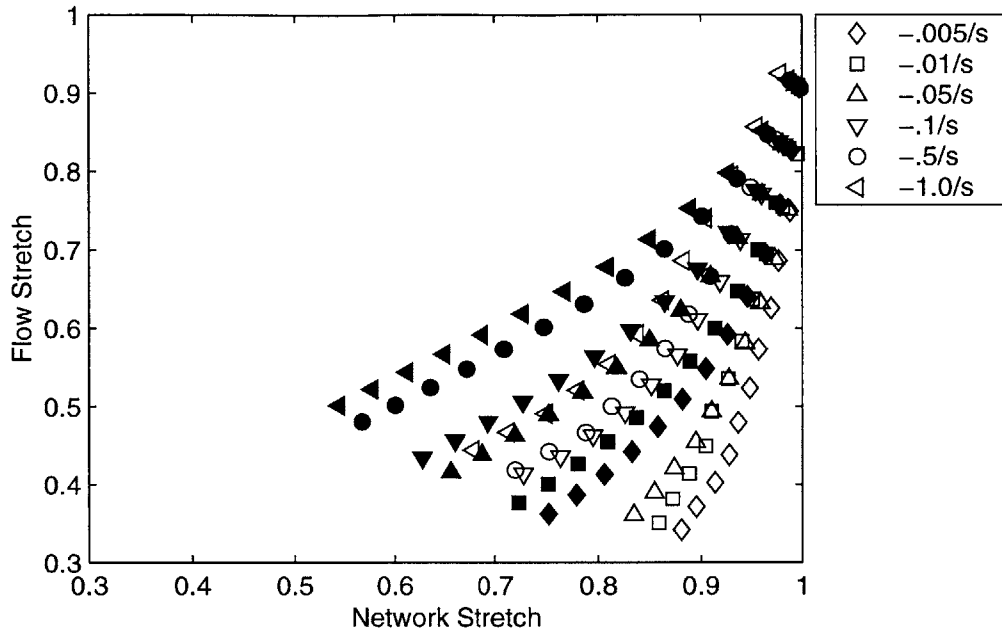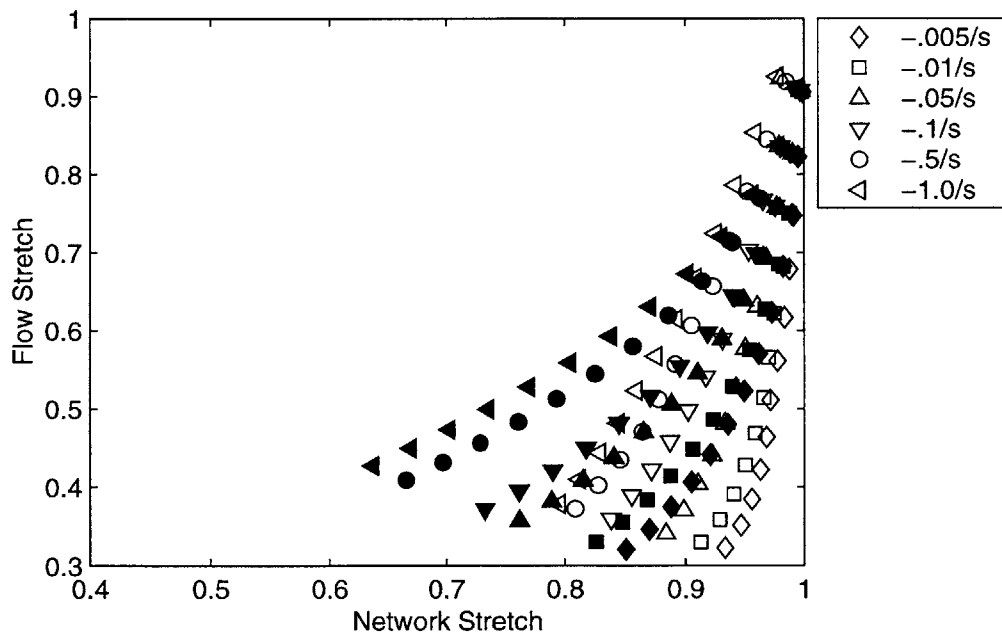
To account for the cessation of flow at large network stretch, the model is modified using the same approach as Adams et al.[2]. Equation 3.22 is modified to be:

$$\dot{\gamma}_B^F = C \frac{(\bar{\lambda}_{NC} - \lambda_N)}{(\bar{\lambda}_{NC} - 1)} \left[\left(\frac{1}{\lambda_F - 1} \right) \tau_B \right]^3 \tag{3.33}$$

where $\bar{\lambda}_{NC}$ is the critical network stretch where molecular orientation causes molecular relaxation to cease. This provides the functionality that as the network stretch, λ_N, approaches $\bar{\lambda}_{NC}$, the flow strain rate, $\dot{\gamma}_B^F$, goes to zero. When this occurs, all subsequent straining is accommodated by the network orientation element of Network B.

The temperature and strain-rate dependence of $\bar{\lambda}_{NC}$ is modeled phenomenologically based on the uniaxial compression data in a similar manner to Boyce et al.[12]

$$\bar{\lambda}_{NC} = \lambda^* + m \log_{10}(\dot{\gamma}_A^p / 0.0173) \tag{3.34}$$

where

$$\lambda^* = 1.06 - .0035(\theta - 363\text{K}) + .00005(\theta - 363\text{K})^2 \tag{3.35}$$

$$m = .06 + .0065(\theta - 363\text{K}) - .00035(\theta - 363\text{K})^2 \tag{3.36}$$

The computer simulation with this modification to the material model is illustrated in the following figures. Figures 3-39 through 3-48 show the results for uniaxial compression and figures 3-49 and 3-51 show the results for plane strain compression. These figures illustrate that the model still captures the strain and temperature dependence of the initial modulus, flow stress, and initial hardening modulus of the PETG. In addition, the model is now capable of predicting the large upswing in stress at large strains. An item of interest is the unloading behavior predicted by the model. The model now predicts more recovery than before the critical locking stretch modification was made, but still somewhat under predicts that observed in

77

experiment. Particularly in the low strain rate experiments, the unloading curve follows almost on top of the loading curve up to the strain level where the locking stretch is again achieved. This is because of the low flow stress values at these high temperatures and low strain rates. The model predicts an initial linear drop off upon unloading equal to twice the initial flow stress value. At lower temperatures, such as the 80 ° C curves, where the flow stress is quite large in magnitude (5 - 10 MPa) this initial drop off is quite large, as indicated in figure 3-39. In the higher temperature, lower strain rate curves, however, the flow stress approaches 0 MPa, so the unloading drop off is almost unobservable and the material unloads along the same path as during loading.

Another interesting feature in the unloading behavior is the apparent "kink" in the unloading curve which corresponds to the strain level at which molecular relaxation ceased upon loading. At this point, the material model predicts that relaxation will again become effective and therefore serves to increase the slope of the unloading curve and cause the material to sustain a higher residual strain than if the molecular relaxation had not again become effective. It is suggested that if this effect were eliminated from the model, the model may be able to better capture the final residual strain apparent in the experimental data. Further work with a series of experiments in which the material is loaded, unloaded, and reloaded needs to be done to better capture the material unloading behavior with the constitutive model.

Figures 3-52 through 3-58 show the comparison of simulation with experiment. It can be seen that the uniaxial compression experiments are much better approximated with the new model, particularly at large strains. The 80 ° C data shows especially good agreement at all strain rates, even though the model was not specifically fit to this data. The model also captures the behavior at 90 ° C and at 100 ° C quite well. At 110 ° C the fit is not quite as good, but is still better than without the added flow cutoff features. The plane strain simulation still rises above the plane strain compression data, as was anticipated due to the initial strain hardening curve fit.

Figures 3-59 through 3-63 again show the network stretch versus flow stretch for the experimental data and for the computer model at various temperatures and in

both deformation modes. These plots demonstrate that this form for the molecular relaxation cessation captures the flow cutoff quite well. For example, in figure 3-59 the -1.0 sec^{-1} simulation, indicated by filled triangles pointing left, lies virtually on top of the data for this strain rate, indicated by the open left pointing triangles. Similar correllation occurs at other strain rates and temperatures for the uniaxial compression experiments and simulations. In plane strain, the agreement is not as good, which is consistent with the overprediction of the strain hardening behavior in plane strain.

Overall, this series of experiments and simulations indicates the many features of the model adequately represent the mechanical behavior of PETG. The initial modulus is captured well, as is verified by both DMA experiments and uniaxial and plane strain compression experiments. The initial flow stress is captured very well using the thermally-activated mechanism. The Arruda-Boyce model captures the strain state dependence of the hardening curve, and the molecular relaxation expressions provide a good representation of the temperature and rate dependent large strain behavior. Future work is needed to refine the strain hardening fit to better capture the state of strain behavior. Future efforts will also need to investigate the unloading behavior of the material and the way in which the model attempts to capture this unloading so as to correctly predict the amount of residual strain left in the material after deformation.
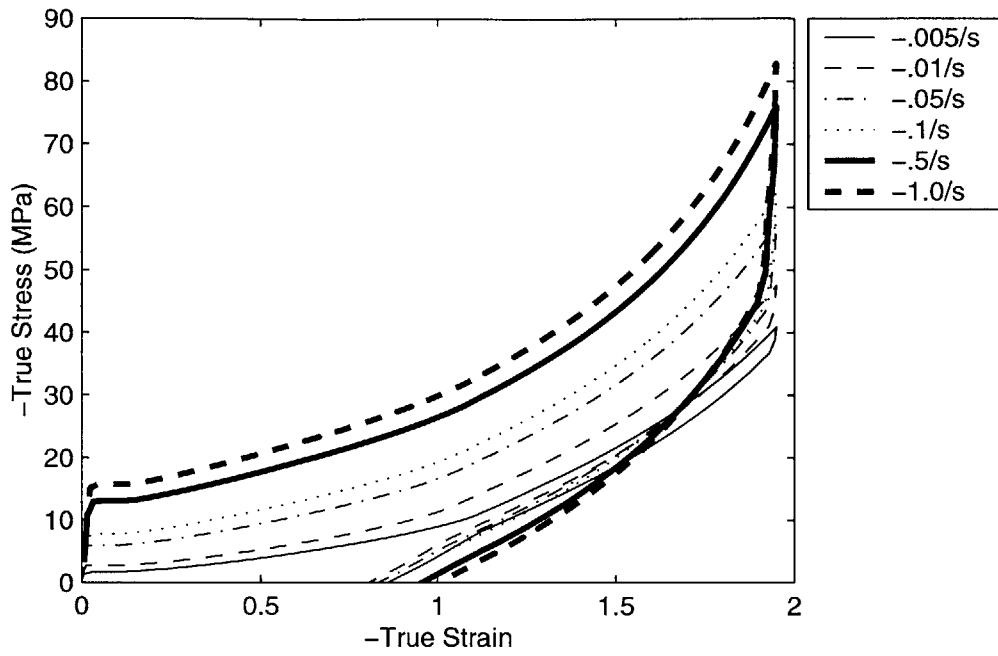
Figure 3-39: Uniaxial Compression Simulation, Temperature = 80 ° C
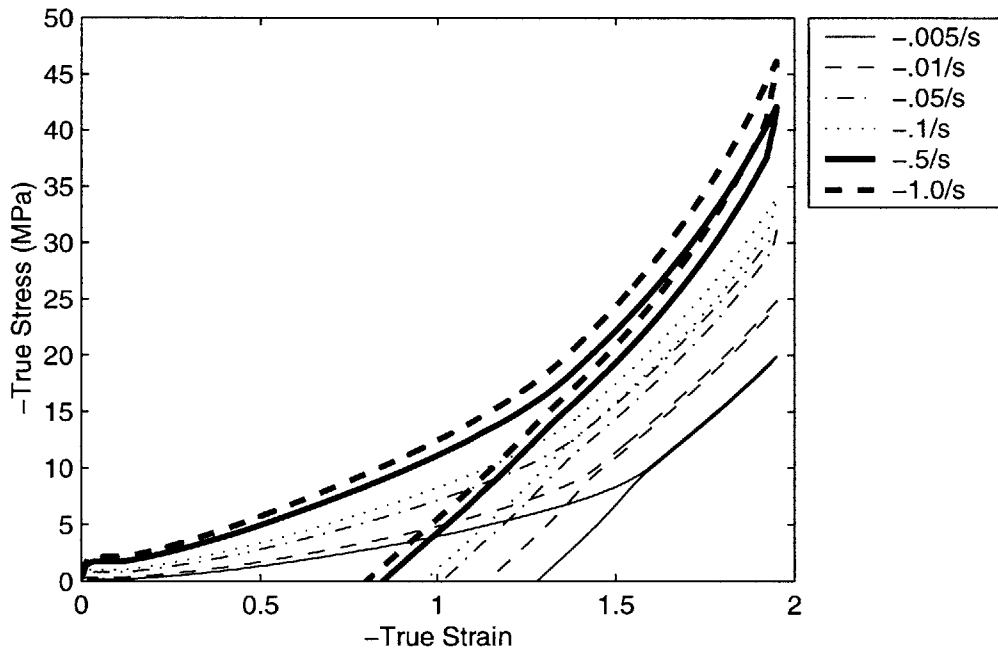

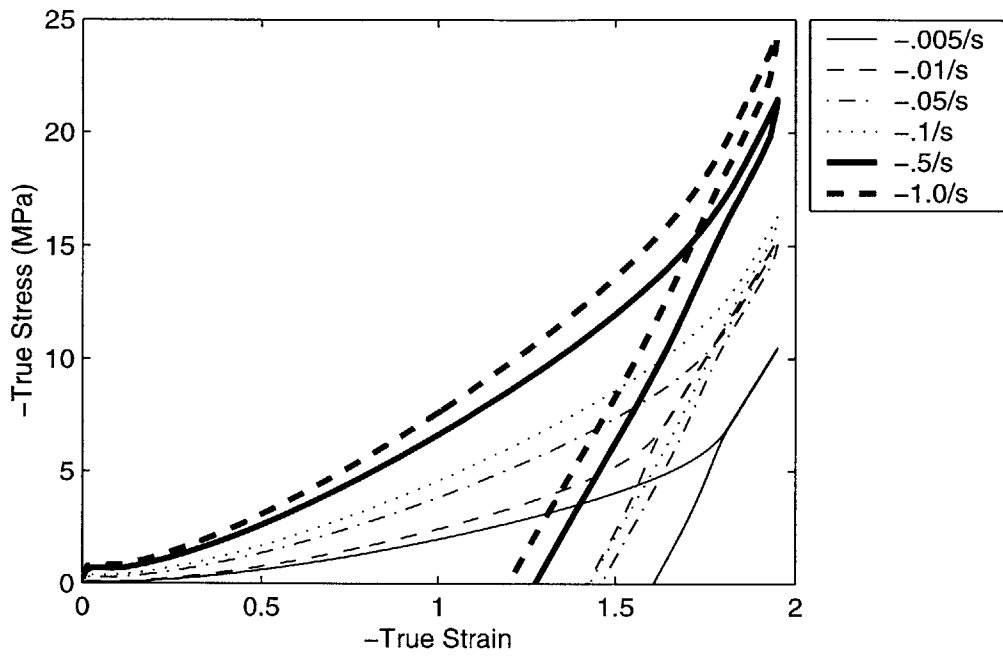Figure 3-40: Uniaxial Compression Simulation, Temperature = 90 ° C

Figure 3-41: Uniaxial Compression Simulation, Temperature = 100 ° C
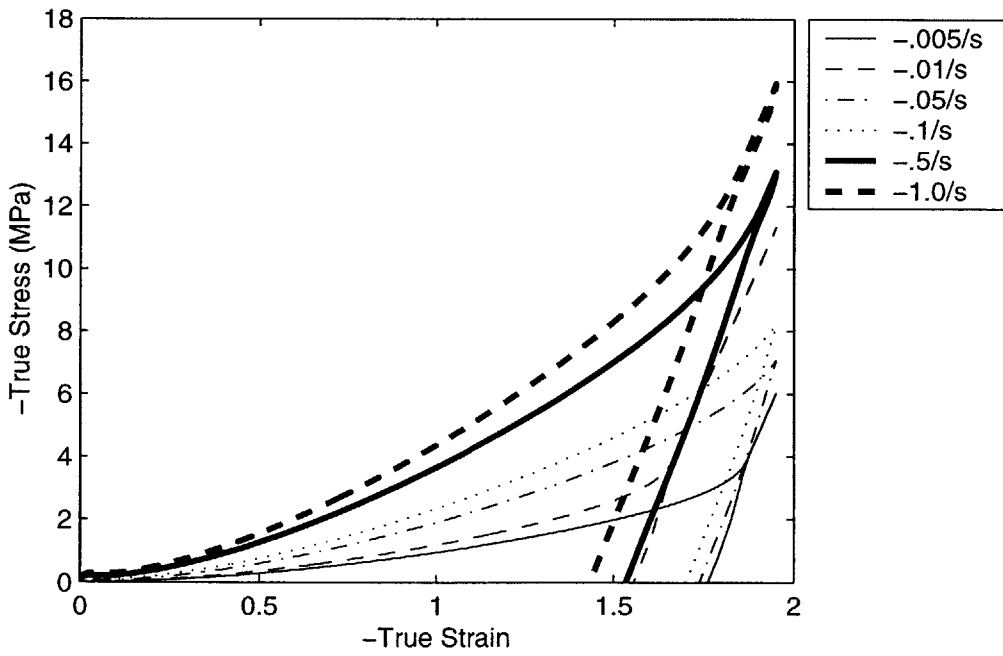

Figure 3-42: Uniaxial Compression Simulation, Temperature = 110 ° C

Figure 3-43: Uniaxial Compression Simulation, $\dot{\varepsilon} = -.005/\text{s}$

Figure 3-44: Uniaxial Compression Simulation, $\dot{\varepsilon} = -.01/\text{s}$
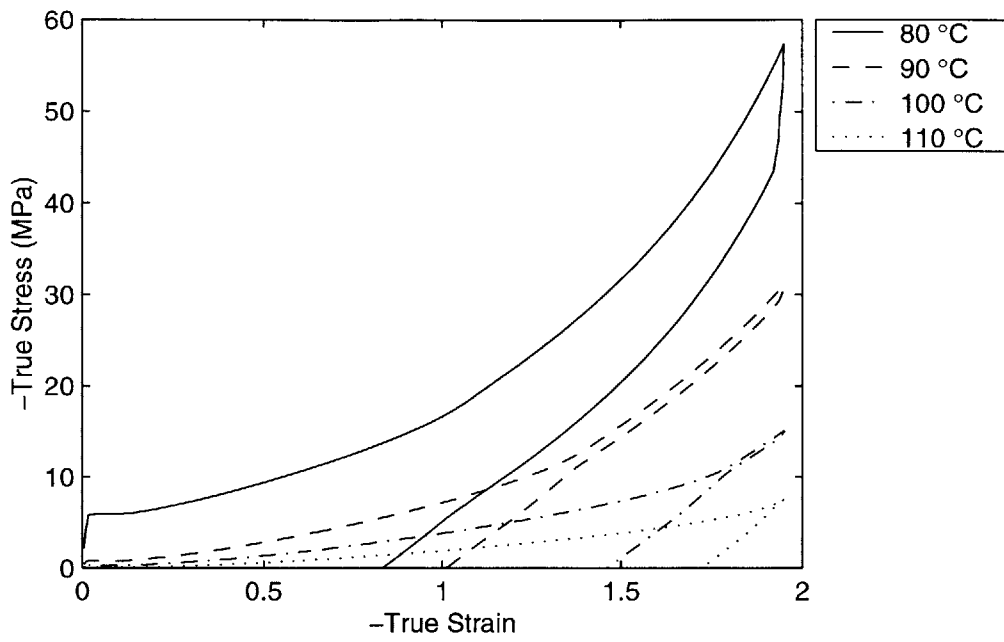
Figure 3-45: Uniaxial Compression Simulation, $\dot{\varepsilon} = -.05/\mathrm{s}$
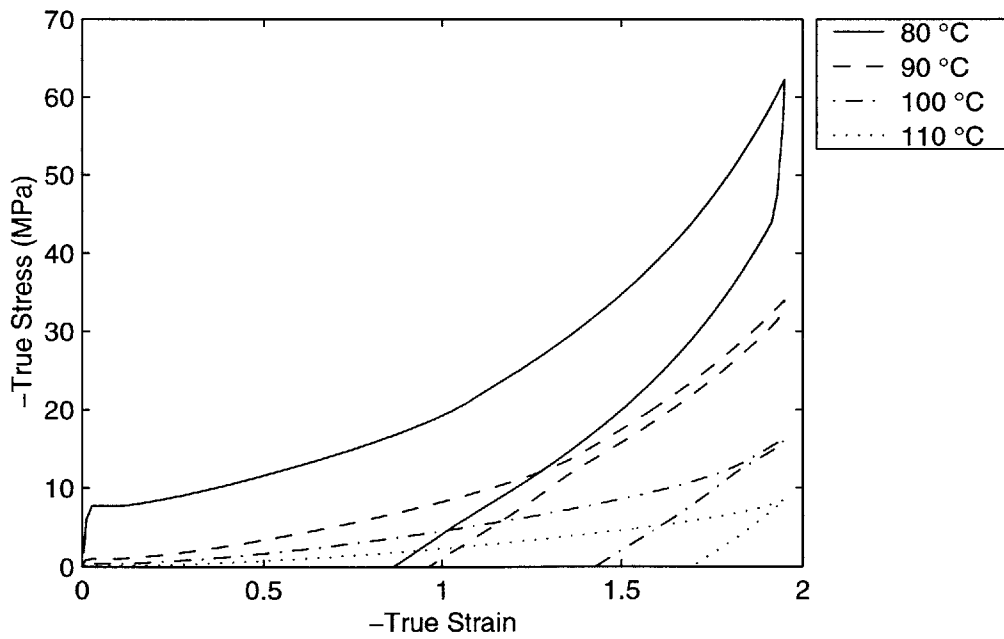
Figure 3-46: Uniaxial Compression Simulation, $\dot{\varepsilon} = -.1/\mathrm{s}$
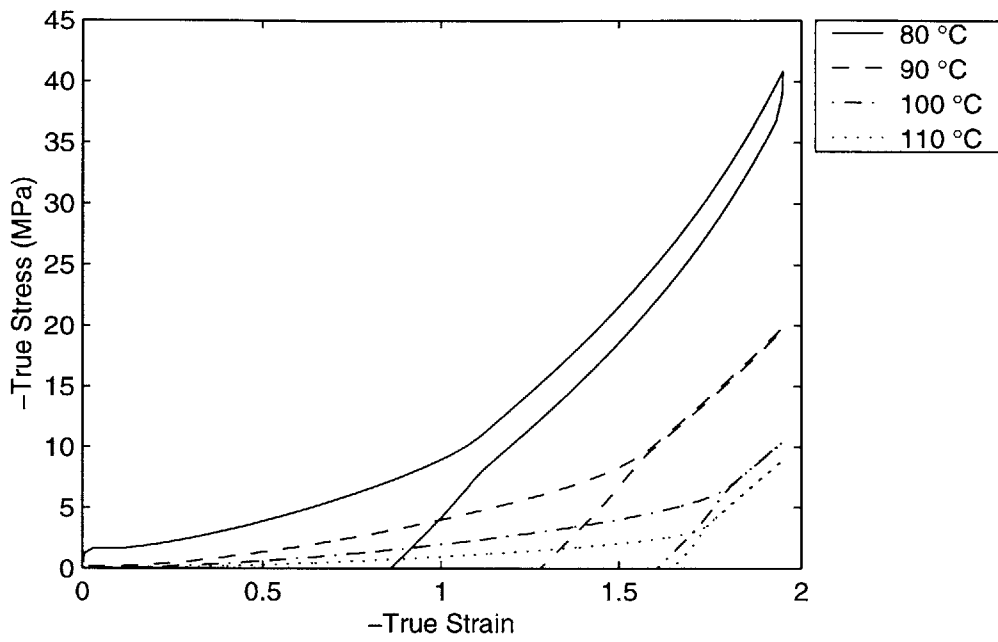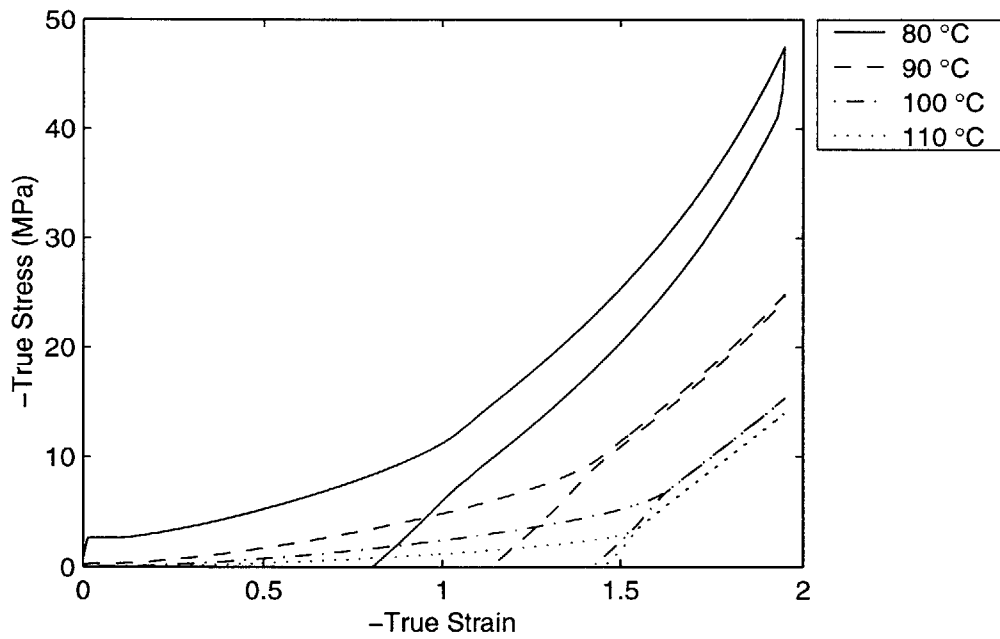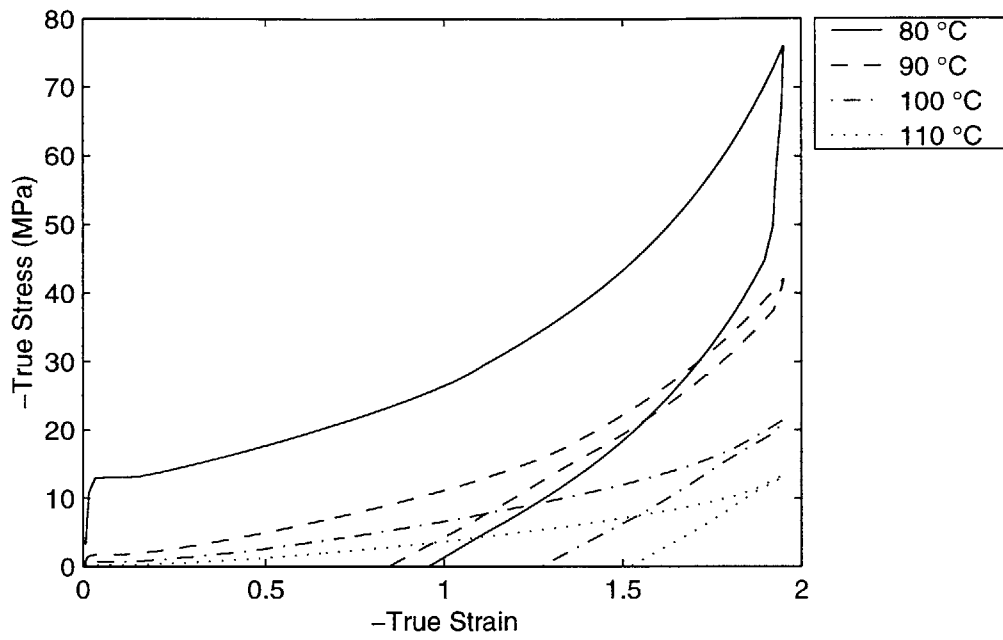
Figure 3-47: Uniaxial Compression Simulation, $\dot{\varepsilon} = -.5/s$
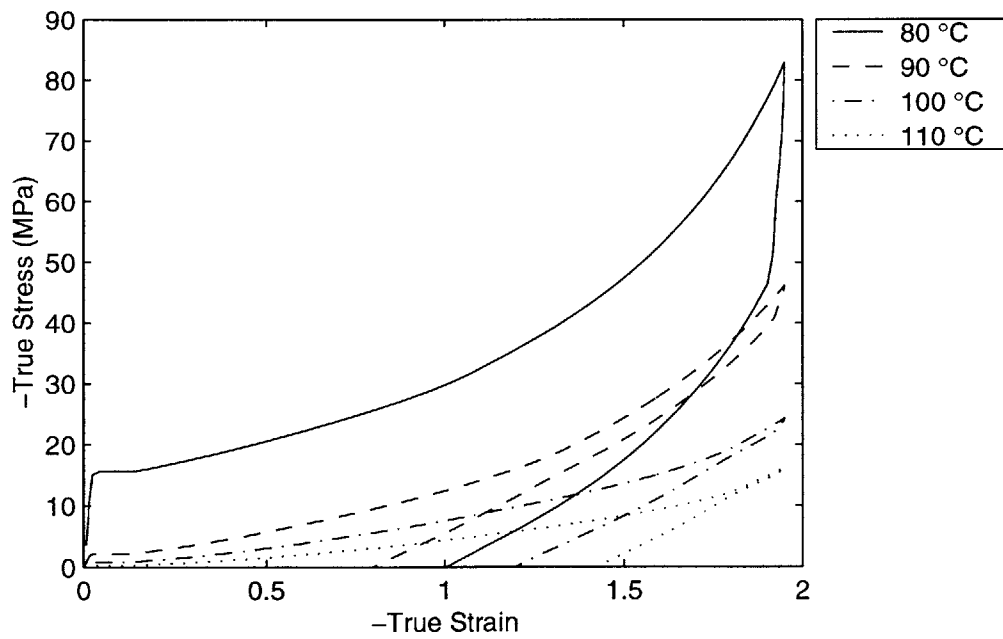
Figure 3-48: Uniaxial Compression Simulation, $\dot{\varepsilon} = -1.0/s$
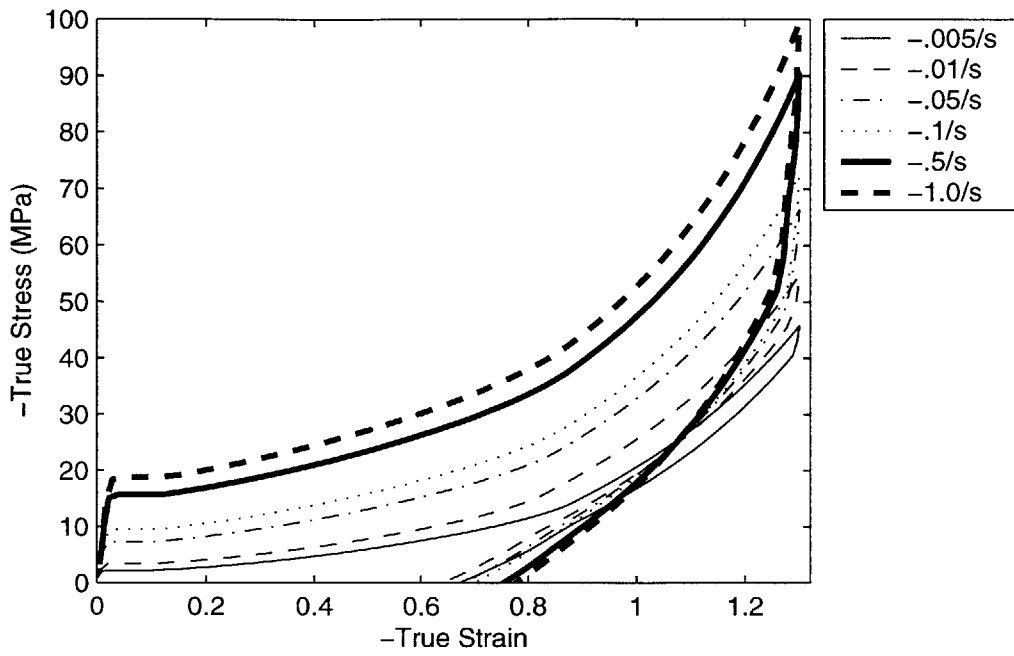
Figure 3-49: Plane Strain Compression Simulation, Temperature = 80 ° C
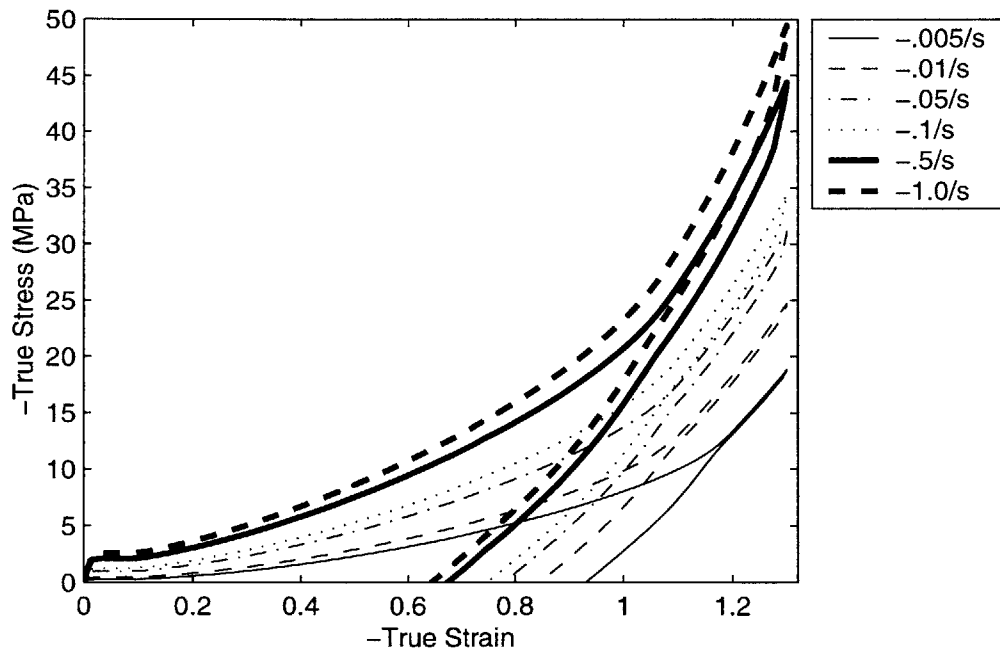
Figure 3-50: Plane Strain Compression Simulation, Temperature = 90 ° C
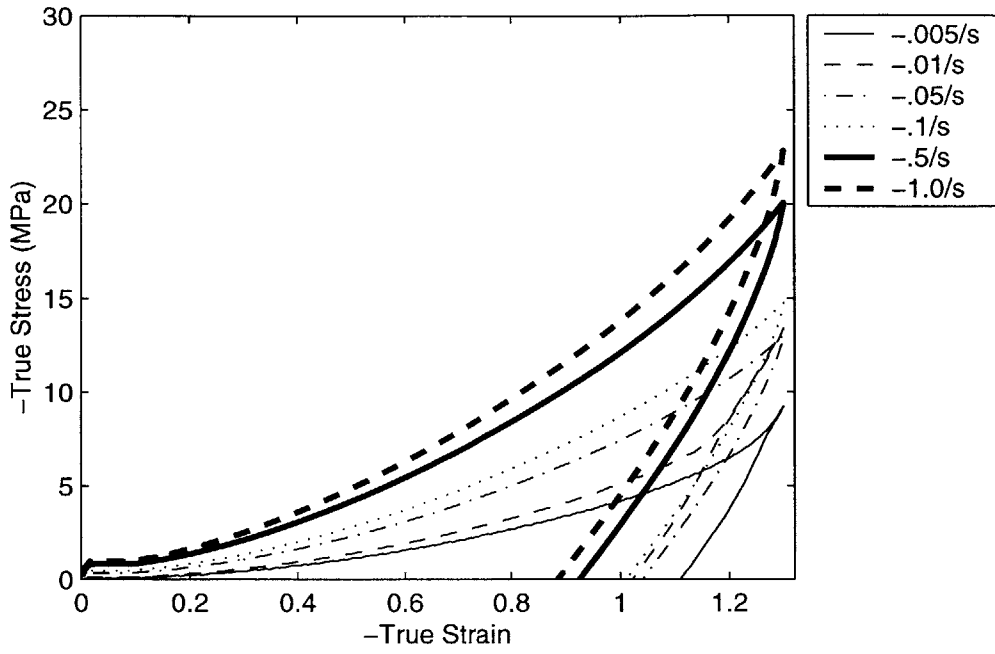
Figure 3-51: Plane Strain Compression Simulation, Temperature = 100 ° C
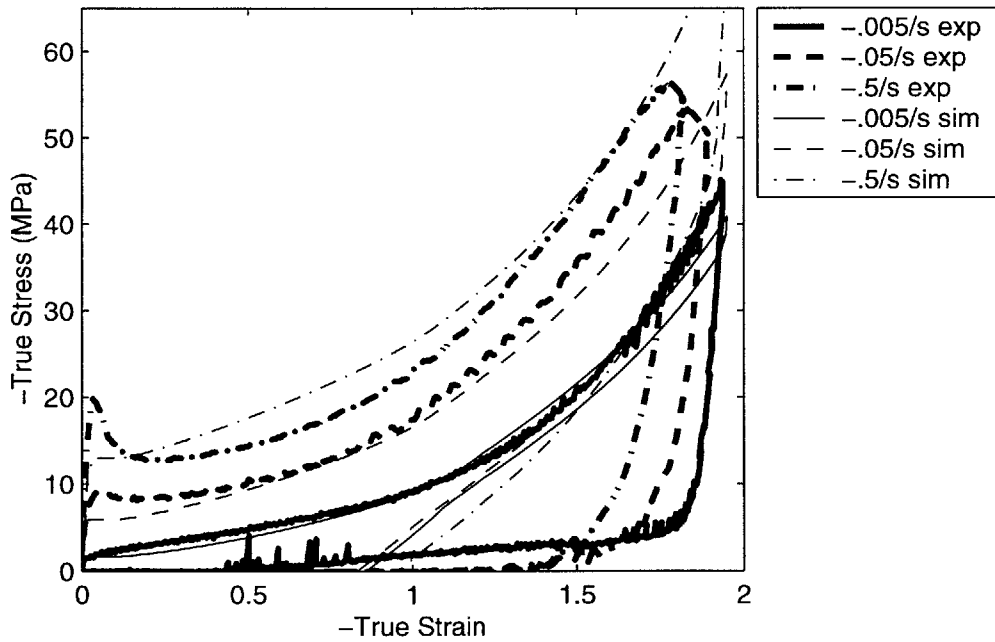
Figure 3-52: Uniaxial Compression, Comparing Simulation with Experimental Data, Temperature = 80 ° C
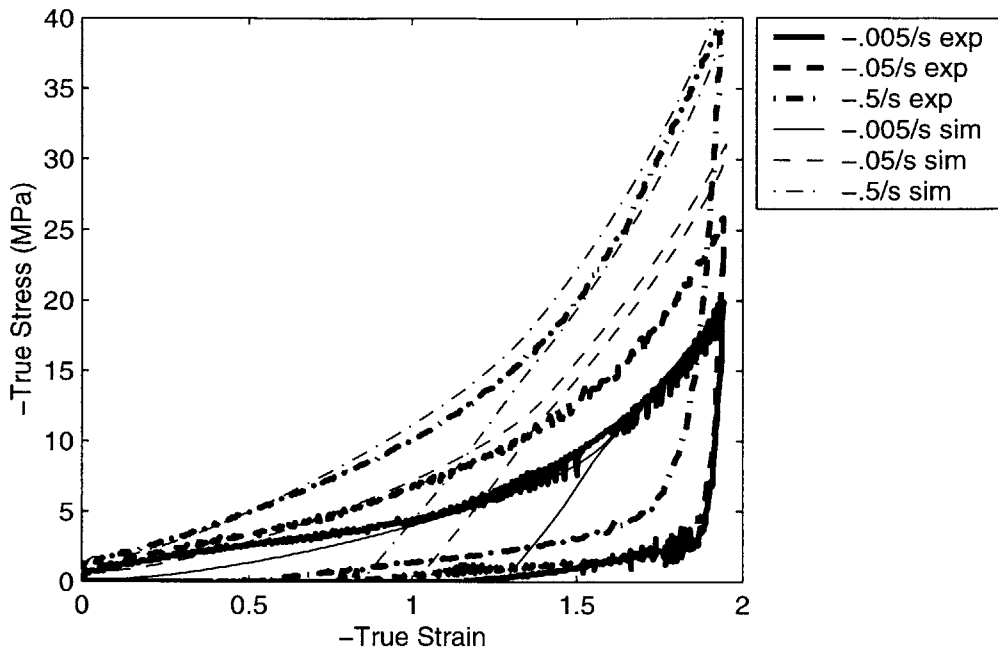
Figure 3-53: Uniaxial Compression, Comparing Simulation with Experimental Data, Temperature = 90 °C
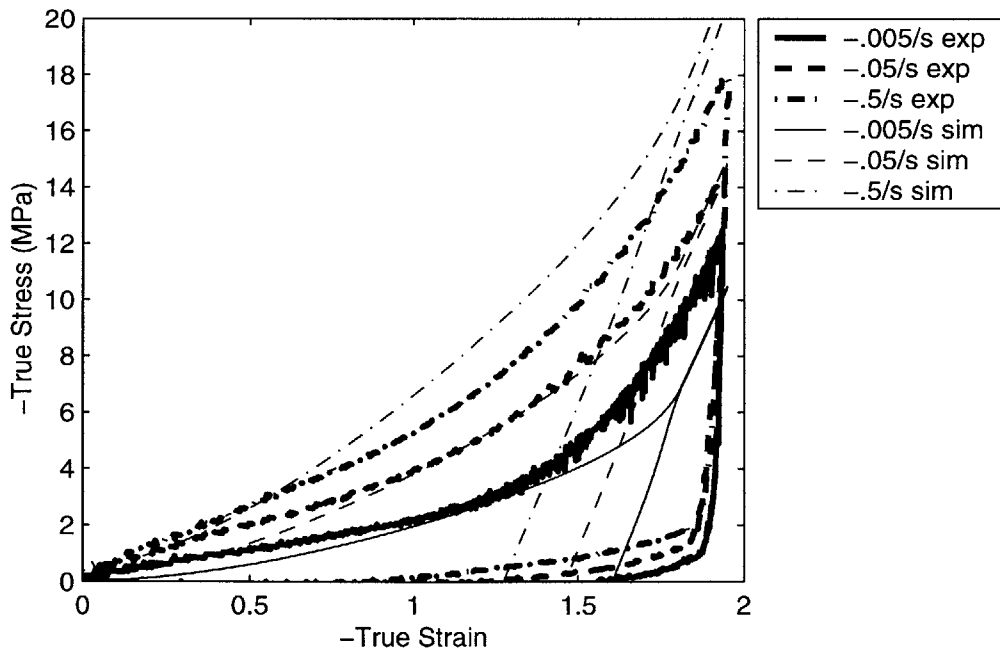
Figure 3-54: Uniaxial Compression, Comparing Simulation with Experimental Data, Temperature = 100 °C

87
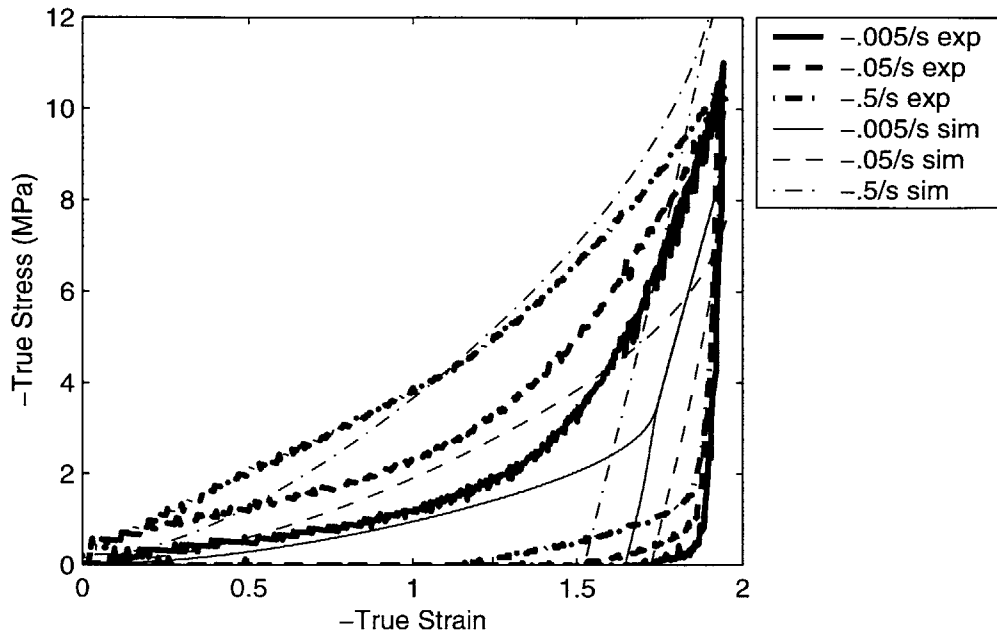
Figure 3-55: Uniaxial Compression, Comparing Simulation with Experimental Data, Temperature = 110 °C
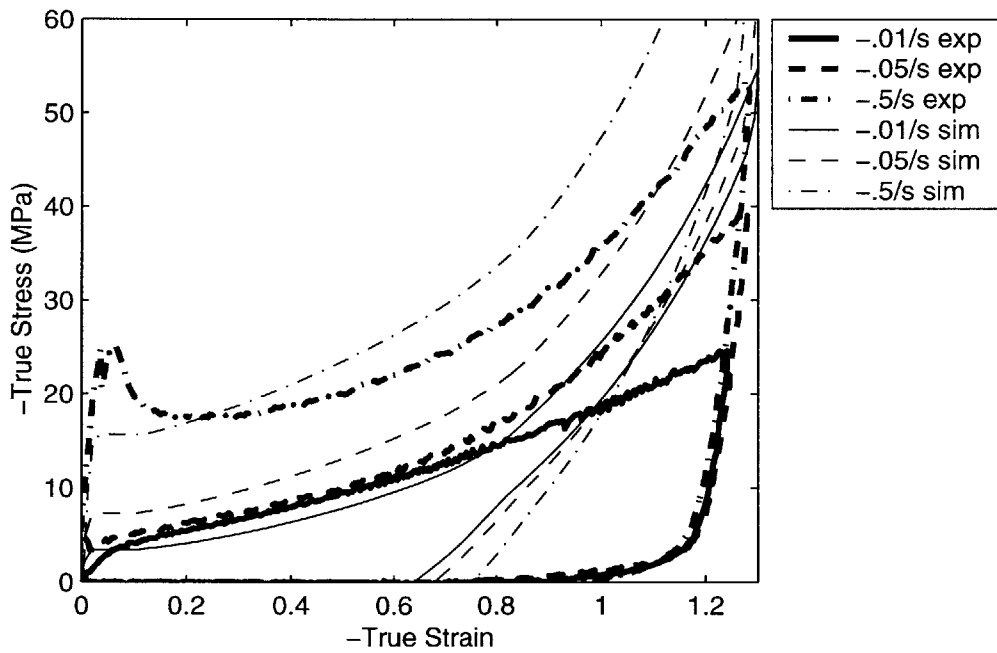
Figure 3-56: Plane Strain Compression, Comparing Simulation with Experimental Data, Temperature = 80 °C
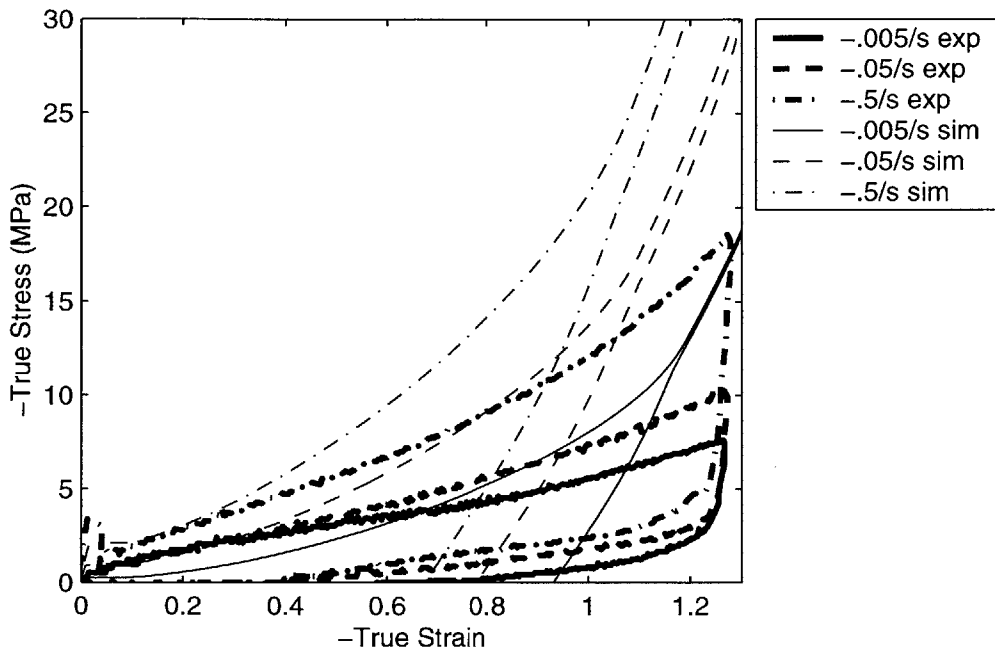
Figure 3-57: Plane Strain Compression, Comparing Simulation with Experimental Data, Temperature = 90 °C
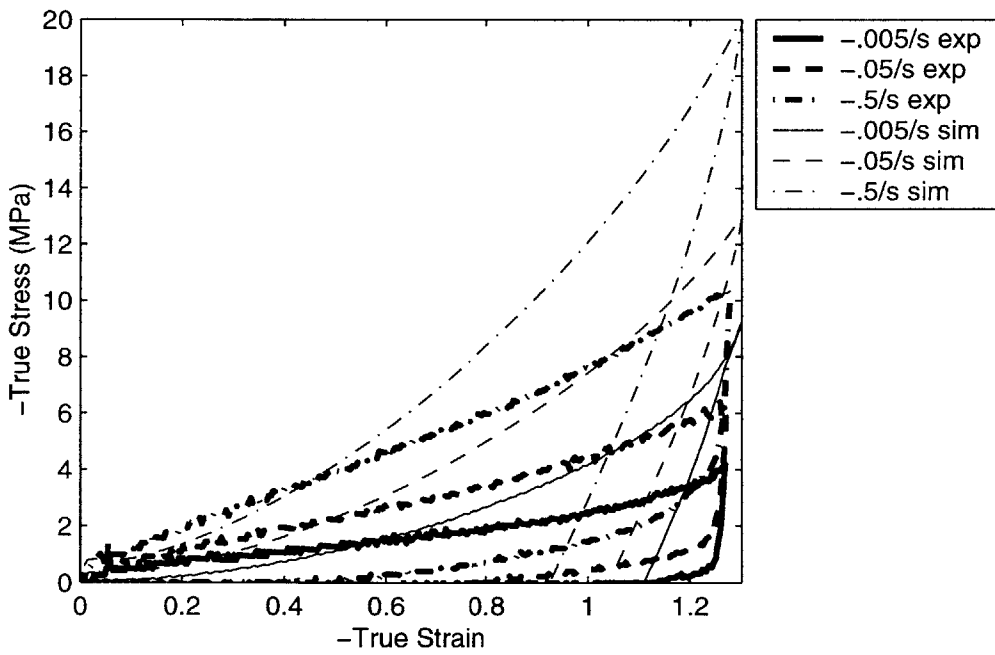
Figure 3-58: Plane Strain Compression, Comparing Simulation with Experimental Data, Temperature = 100 °C
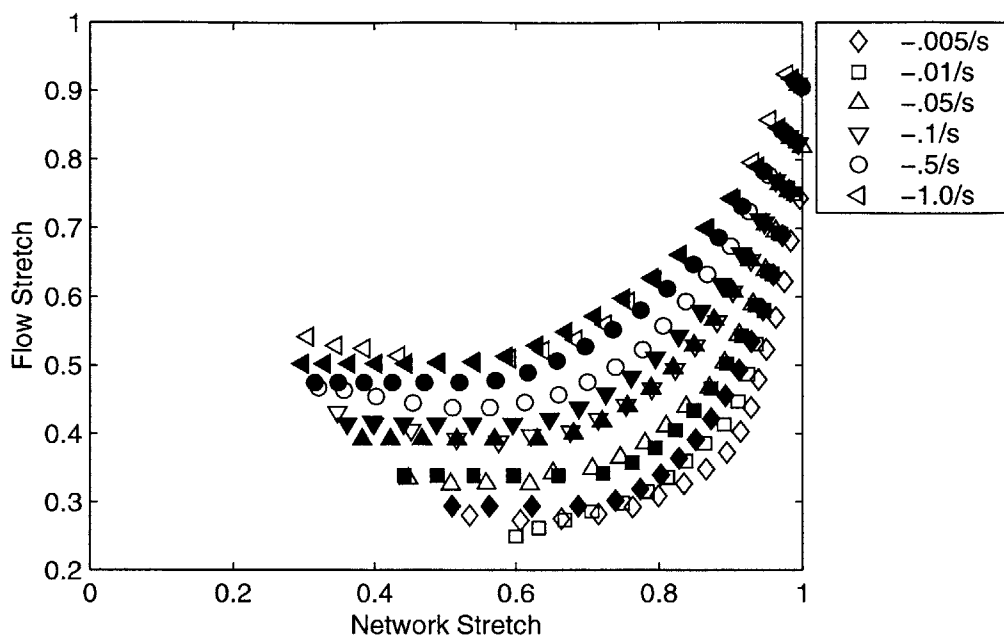
Figure 3-59: Network Stretch versus Flow Stretch, Uniaxial Compression, T = 90 ° C (open symbols are experimental data; filled symbols are computer simulations)
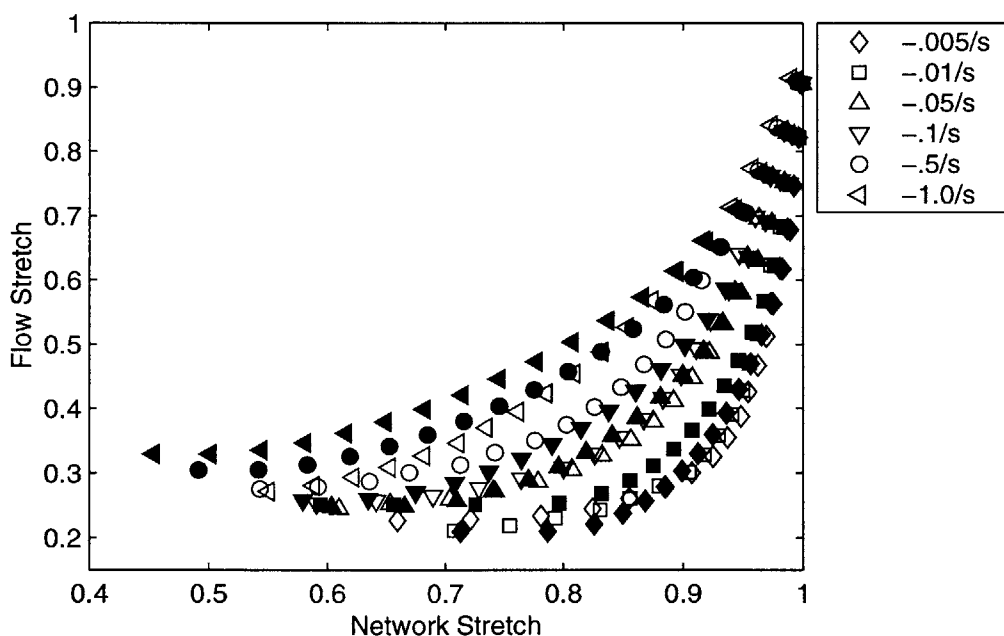
Figure 3-60: Network Stretch versus Flow Stretch, Uniaxial Compression, T = 100 ° C (open symbols are experimental data; filled symbols are computer simulations)
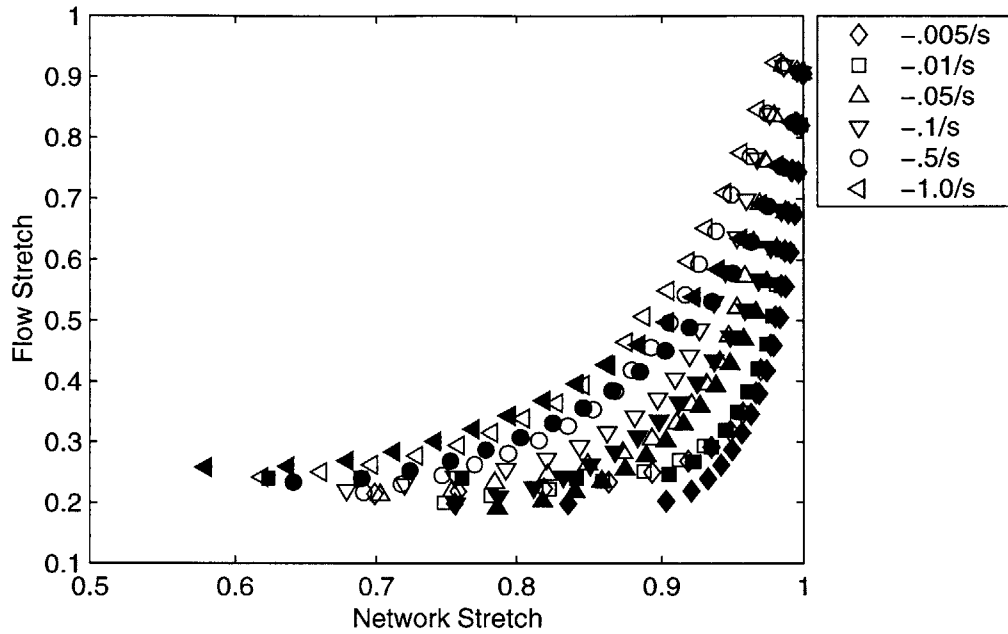
Figure 3-61: Network Stretch versus Flow Stretch, Uniaxial Compression, T = 110 ° C (open symbols are experimental data; filled symbols are computer simulations)
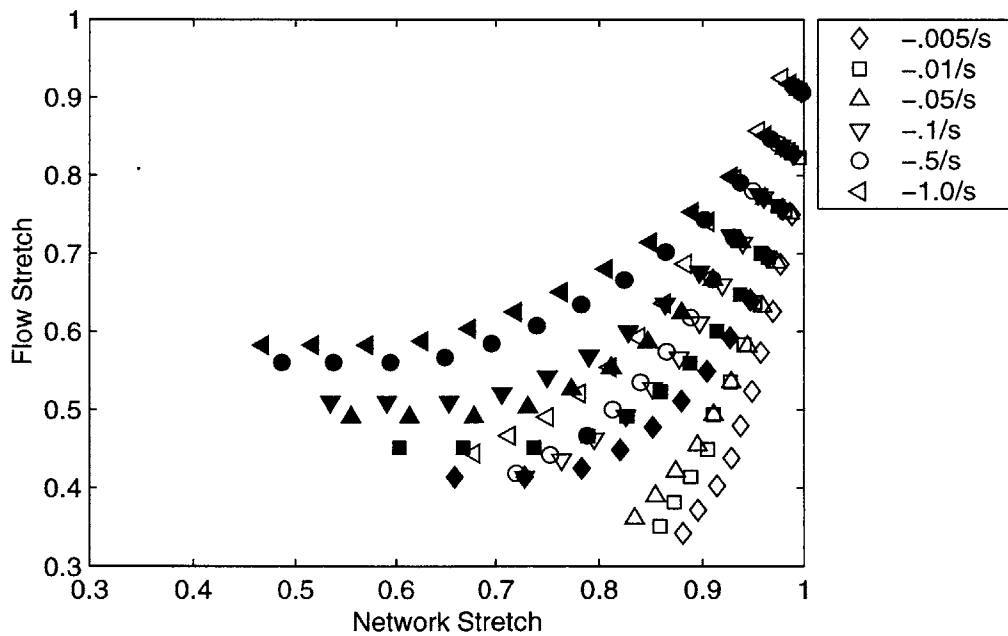
Figure 3-62: Network Stretch versus Flow Stretch, Plane Strain Compression, T = 90 ° C (open symbols are experimental data; filled symbols are computer simulations)
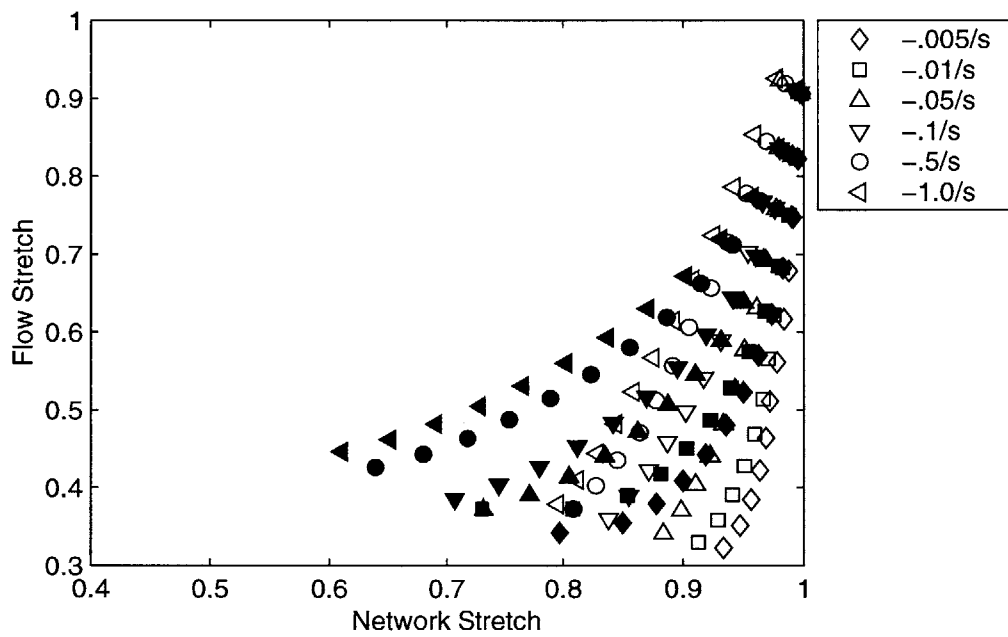
Figure 3-63: Network Stretch versus Flow Stretch, Plane Strain Compression, T = 100 ° C (open symbols are experimental data; filled symbols are computer simulations)

Chapter 4

Conclusions and Future Work

A series of compression experiments have been performed on PETG at temperatures in and above the glass transition region. These experiments were performed in order to identify the strain rate, temperature, and strain state dependence of the large strain deformation behavior of the material. Experiments in both uniaxial and plane strain deformation modes were conducted. The data seems to be self-consistent and follows the general trends expected for a polymer in this temperature range. The pressure dependence of the material is one aspect which has yet to be determined. In future work, a series of uniaxial tension experiments and biaxial extension experiments will be performed on the same material to determine if there is a pressure dependence to the orientation evolution.

In attempting to prescribe the molecular relaxation portion of the constitutive model for PETG, it was determined that the behavior could not be correctly modeled without incorporating a value of network stretch where molecular relaxation ceased. PETG does not crystallize, so this indicates that polymers can experience a cessation of flow solely due to molecular orientation. This is consistent with the findings of Blundell, et al.[10] and Mahendrasingam, et al.[26, 27] that PET does not crystallize during deformation, only after motion has ceased and that the upswing in the stress-strain curve is due to orientation alone, not crystallization. Boyce, et al. [12] and Adams, et al.[2] both incorporated this cessation to flow into their models to account for crystallization. It appears that in PET, flow does cease at the critical network

stretch, but this cessation is due to molecular orientation rather than strain induced crystallization. Then, at the end of the deformation process, the PET crystallizes rapidly due to the applied strain and continues to crystallize during cooling, imparting the high strength and stiffness properties to the final product. In PETG, this same cessation to flow occurs as this polymer reaches a critical orientation stretch, but after flow ceases, the polymer is unable to crystallize and so does not gain those extra strength and stiffness properties and exhibits far greater recovery upon unloading since the orientation is not frozen in by crystallization.

The material model presented accounts for many aspects of the stress-strain behavior of PETG, but falls somewhat short in predicting behavior in different deformation modes. Future work needs to be done in order to refine the strain hardening parameters to fit the data in both uniaxial and plane strain compression. It is also possible that once the strain hardening issue is resolved the molecular relaxation expression will also need some modification. Once the model is refined to fully capture the strain state dependence, computer simulations can be performed to correspond with biaxial, tensile, and blow molding experiments.

Another element to be investigated in future work is the effect of reloading specimens which have been previously deformed. A series of loading/unloading/reloading experiments as well as experiments which include sequential stretch histories will be helpful in testing the model's ability to capture the final material state after straining.

Finally, the completed model can then be adapted to account for crystallization effects and be applied to PET.

Bibliography

[1] A. M. Adams, C. P. Buckley, and D. P. Jones. Biaxial hot-drawing of poly(ethylene terephalate): dependence of yield stress on strain-rate ratio. *Polymer*, 39(23):5761–5763, November 1998.

[2] A. M. Adams, C. P. Buckley, and D. P. Jones. Biaxial hot drawing of poly(ethylene terephthalate): measurements and modelling of strain-stiffening. *Polymer*, 41(2):771–786, January 2000.

[3] E. M. Arruda and M. C. Boyce. Evolution of plastic anisotropy in amorphous polymers during finite straining. *International Journal of Plasticity*, 9(6):697–720, 1993.

[4] E. M. Arruda and M. C. Boyce. A three-dimensional constitutive model for the large stretch behavior of rubber elastic materials. *Journal of the Mechanics and Physics of Solids*, 41(2):389–412, February 1993.

[5] E. M. Arruda, M. C. Boyce, and R. Jayachandran. Effects of strain rate, temperature and thermomechanical coupling on the finite strain deformation of glassy polymers. *Mechanics of Materials*, 19:193–212, January 1995.

[6] F. H. Axtell and B. Haworth. Elongational deformation and stretch blow moulding of poly(ethylene terephthalate). *Plastics, Rubber, and Composites Processing and Applications*, 22(3):127–136, 1994.

[7] R. C. Ball, M. Doi, S. F. Edwards, and M. Warner. Elasticity of entangled networks. *Polymer*, 22:"1010", 1981.

[8] A. Bellare, R. E. Cohen, and A. S. Argon. Development of texture in poly(ethylene terephthalate) by plane-strain compression. *Polymer*, 34(7):1393–1403, 1993.

[9] J. S. Bergstrom and M. C. Boyce. Constitutive modeling of the large strain time-dependent behavior of elastomers. *Journal of the Mechanics and Physics of Solids*, 46(5):931–954, May 1998.

[10] D. J. Blundell, D. H. MacKerron, W. Fuller, A. Mahendrasingam, C. Martin, R. J. Oldman, R. J. Rule, and C. Riekel. Characterization of strain-induced crystallization of poly(ethylene terephthalate) at fast draw rates using synchrotron radiation. *Polymer*, 37(15):3303–3311, July 1996.

[11] M. C. Boyce, D. M. Parks, and A. S. Argon. Large inelastic deformation of glassy polymers. part i: Rate dependent constitutive model. *Mechanics of Materials*, 7:15–33, 1988.

[12] M. C. Boyce, S. Socrate, and P. G. Llana. Constitutive model for the finite deformation stress-strain behavior of poly(ethylene terephthalate) above the glass transition. *Polymer*, 41(6):2183–2201, March 2000.

[13] C. P. Buckley and D. C. Jones. Glass-rubber constitutive model for amorphous polymers near the glass transition. *Polymer*, 36(17):3301–3312, August 1995.

[14] C. P. Buckley, D. C. Jones, and D. P. Jones. Hot-drawing of poly(ethylene terephthalate) under biaxial stress: application of a three-dimensional glass-rubber constitutive model. *Polymer*, 37(12):2403–2414, June 1996.

[15] Cakmak, White, and Spruiell. Structure development in stretch blow molding polyethylene terephthalate bottles. In *ANTEC '85*, pages 912–915. ANTEC, 1985.

[16] P. Chandran and S. Jabarin. Biaxial orientation of poly(ethylene terephthalate). Part I: Nature of the stress-strain curves. *Advances in Polymer Technology*, 12(2):119–132, 1993.

[17] P. Chandran and S. Jabarin. Biaxial orientation of poly(ethylene terephthalate). Part II: The strain-hardening parameter. *Advances in Polymer Technology*, 12(2):133–151, 1993.

[18] P. Chandran and S. Jabarin. Biaxial orientation of poly(ethylene terephthalate). Part III: Comparative structure and property changes resulting from simultaneous and sequential orientation. *Advances in Polymer Technology*, 12(2):153–165, 1993.

[19] M. Doi and M. F. Edwards. *The theory of polymer dynamics*. Oxford University Press, 1986.

[20] R. A. Duckett, S. Rabinowitz, and I. M. Ward. The strain-rate, temperature and pressure dependence of yield of isotropic poly(methylmethacrylate) and poly(ethylene terephthalate). *Journal of Materials Science*, 5:909–915, 1970.

[21] S. F. Edwards and Th. Vilgis. The effect of entanglements in rubber elasticity. *Polymer*, 27(4):483–492, April 1986.

[22] D. H. Gordon, R. A. Duckett, and I. M. Ward. A study of uniaxial and constant-width drawing of poly(ethylene terephthalate). *Polymer*, 35(12):2554–2559, 1994.

[23] J. Y. Guan, L. Wang, and R. S. Porter. Planar deformation of amorphous poly(ethylene terephthalate) by stretching and forging. *Journal of Polymer Science: Part B: Polymer Physics*, 30(7):387–391, June 1992.

[24] S. A. Jabarin. Strain-induced crystallization of poly(ethylene terephthalate). *Polymer Engineering and Science*, 32(18):1341–1348, September 1992.

[25] P. G. Llana and M. C. Boyce. Finite strain behavior of poly(ethylene terephthalate) above the glass transition temperature. *Polymer*, 40(24):6729–6751, November 1999.

[26] A. Mahendrasingam, C. Martin, W. Fuller, D. J. Blundell, R. J. Oldman, J. L. Harvie, D. H. MacKerron, C. Riekel, and P. Engstrom. Effect of draw ratio and

temperature on the strain-induced crystallization of poly (ethylene terephthalate) at fast draw rates. *Polymer*, 40(20):5553–5565, September 1999.

[27] A. Mahendrasingam, C. Martin, W. Fuller, D. J. Blundell, R. J. Oldman, D. H. MacKerron, J. L. Harvie, and C. Riekel. Observation of a transient structure prior to strain-induced crystallization in poly(ethylene terephthalate). *Polymer*, 41(3):1217–1221, February 2000.

[28] I. Marshall and A. B. Thompson. The drawing of 'terylene'. *Journal of Applied Chemistry*, 4:145–153, April 1954.

[29] R. G. Matthews, R. A. Duckett, I. M. Ward, and D. P. Jones. The biaxial drawing behaviour of poly(ethylene terephthalate). *Polymer*, 38(19):4795–4802, September 1997.

[30] A. Misra and R. S. Stein. Stress-induced crystallization of poly(ethylene terephthalate). *Journal of Polymer Science: Polymer Physics Edition*, 17:235–257, 1979.

[31] R. L. Patton. Rate and temperature dependent stress-strain behavior of amorphous pet in uniaxial and plane strain compression. This is a report from an undergraduate research project at MIT, 1998.

[32] D. R. Salem. Development of crystalline order during hot-drawing of poly(ethylene terephthalate) film: influence of strain rate. *Polymer*, 33(15):3182–3188, 1992.

[33] D. R. Salem. Crystallization during hot-drawing of poly(ethylene terephthalate) film: influence of temperature on strain-rate/draw-time superposition. *Polymer*, 35(4):771–776, 1994.

[34] A. B. Thompson. Strain-induced crystallization in polyethylene terephthalate. *Journal of Polymer Science*, 34:741–760, 1959.

[35] J. S. Zaroulis and M. C. Boyce. Temperature, strain rate, and strain state dependence of the evolution in mechanical behaviour and structure of poly(ethylene terephthalate) with finite strain deformation. *Polymer*, 38(6):1303–1315, March 1997.